Universität Basel

Duke UNIVERSITY | BIOMEDICAL ENGINEERING

Master Thesis

Improving Cloning Procedures and Particle Architectures of Elastin-like Polypeptide-based Drug Delivery Vehicles

November 13th 2019

Patrick Weber

Abstracts

Project I

Many peptide and protein ligands used for nanoparticle drug delivery systems today greatly benefit or even require multivalent display for proper function. Though it seems evident that particle disassembly after extensive dilution below the carrier's critical aggregation concentration (CAC) would result in a dramatic decrease in the formulation's potency, to date no studies exist on the relationship between these two factors. In this project, we investigated this effect using resilin-/elastin-like polypeptide (RLP/ELP) diblock copolymer nanoparticles that were functionalized with one of three different protein/peptide ligands: Two protein scaffolds engineered to bind to death receptor 5 and $\alpha_v\beta_3$ integrins respectively as well as an integrin-binding octapeptide. To analyze the effect of particle stability on the formulation's potency, we genetically introduced the unnatural amino acid *para*-acidophenylalanine into the core of the nanoparticles. This modification allowed for chemical crosslinking and was proven to prevent these nanoparticles from disassembling even after extensive dilution. The following cell experiments comparing native with crosslinked particles then showed a pronounced increase in potency below the CAC for the crosslinked particles. Moreover, a convincing correlation between the potency of the native particles and their CAC was found.

Project II

Today, ELP constructs are typically grown and/or modified using the plasmid reconstruction by recursive directional ligation (PRe-RDL) cloning approach. Whereas PRe-RDL is a very reliable strategy, it is not very fast: Using this technique, it takes several weeks to grow larger ELP constructs from scratch. To speed things up, we propose a PRe-RDL-compatible concatemerization strategy through which large constructs are reached within just one single cloning cycle. In this approach, dsDNA monomers with complementary but non-palindromic sticky ends are created through polymerase chain reaction (PCR) followed by enzymatic digestion. The monomers are then concatemerized into the two conventional PRe-RDL cloning vector fragments and the concatemer distribution subsequently screened using colony PCR. The initial proof-of-principle experiments quickly yielded successfully transformed constructs with up to 60 ELP repeats. Subsequently performed experiments after optimization of the PCR and concatemerization conditions then however failed to yield any successful transformations. The sequencing results from three false positive clones indicated that the formed concatemers suffered greatly from frameshift mutations though it still remained unclear what caused these effects.

Project III

So far, ELP-based drug delivery vehicles almost exclusively have a micellar morphology. Though this kind of structure is relatively easy to produce and control, it is limited in terms of the type and amount of cargo that can be delivered as well as the potential complexity of the release cascade. Vesicular architectures on the other hand are a lot more versatile and have become an established architecture for drug delivery systems based on lipids or synthetic polymers. To expand the versatility of ELP-based nanocarriers, we tested 15 ELP di- and triblock constructs carrying differently charged coronal blocks for their potential towards vesicle formation. Though we made several interesting off-target observations along the way none of the

analyzed constructs seemed to form vesicular structures. The failure of this project was most probably due to too much time being spent on different coronal blocks which could have been invested in the exploration of different di- and triblock architectures as well as alternative sample preparation techniques.

Table of Contents

1. Introduction

1.1 Targeted Drug Delivery

According to the Global Cancer Statistics published by the American Cancer Society, cancer globally accounted for nearly 10 million deaths in 2018 making it the second leading cause of death worldwide behind cardiovascular diseases[1]. As a result of continuously increasing standards of living all around the world and the increased life expectancy that comes with it, it is only a matter of time until cancer will become the number one cause of death worldwide. In the face of this, it is not surprising at all that a lot of resources have been invested in the development of better cancer diagnosis and treatment during the last decades. In fact, the number of papers containing the word "cancer" in their title increased almost five-fold since 1990[2].

One of the main challenges for researchers working on cancer treatments is specificity. Developing a drug that kills cancer cells is relatively easy and we have possessed such drugs since shortly after World War II[3]. Developing a drug that *only* kills cancer cells but does not attack healthy cells is significantly more difficult since every tumor is unique and there simply is no characteristic that clearly differentiates all tumor cells and tissue from their healthy counterparts. Nevertheless, there still exist a few features generally attributed to cancer tissue and cells which researchers have exploited in the past to develop therapeutics with improved specificity.

The first of those features is that although many processes in cancer cells generally have a rather chaotic and dysregulated nature, there are some systematic differences in protein expression levels compared to healthy cells. Particularly important are altered receptor densities in the cellular membrane as they are the most easily accessible from the extracellular space. This has led researchers all over the world to catalogue cancer cells by their transmembrane proteins and to identify proteins which could be useful in developing a more specific cancer treatment. The class of drugs coming out of this targeting strategy is called ligand-targeted therapeutics (LTTs). In LTTs, ligands with high affinities to certain membrane-bound proteins on cancer cells are employed to increase local concentrations and/or cell uptake of a given anticancer drug. Though some of the antibody-based LTT formulations have since entered clinical trials or have even been approved for commercial use, ligand-drug conjugates often suffer from poor drug loading, premature clearance and insufficient delivery to the target cells[4,5].

The second targeting strategy is based on the macroscopic properties of solid tumors themselves: Due to the chaotic growth of solid tumors, the epithelia of their vasculature is not nearly as tight as in healthy tissue. As a result, macromolecules with a size of up to several hundreds of nanometers can slip through the blood vessel epithelia in solid tumors which would not be possible elsewhere in the body[6,7]. The resulting accumulation of macromolecules in the tumor tissue is better known as the enhanced permeability and retention (EPR) effect and is the main passive targeting strategy exploited for cancer treatment today (fig. 1)[6]. The macromolecules employed for EPR-targeting mostly have self-assembled micellar or vesicular architectures and are made up of amphiphilic molecules such as lipids, synthetic block copolymers or biopolymers[8–11]. These liposomes/polymersomes are typically loaded with a small molecule drug which is then released in the tumor microenvironment. Until today, several nanomedicines of

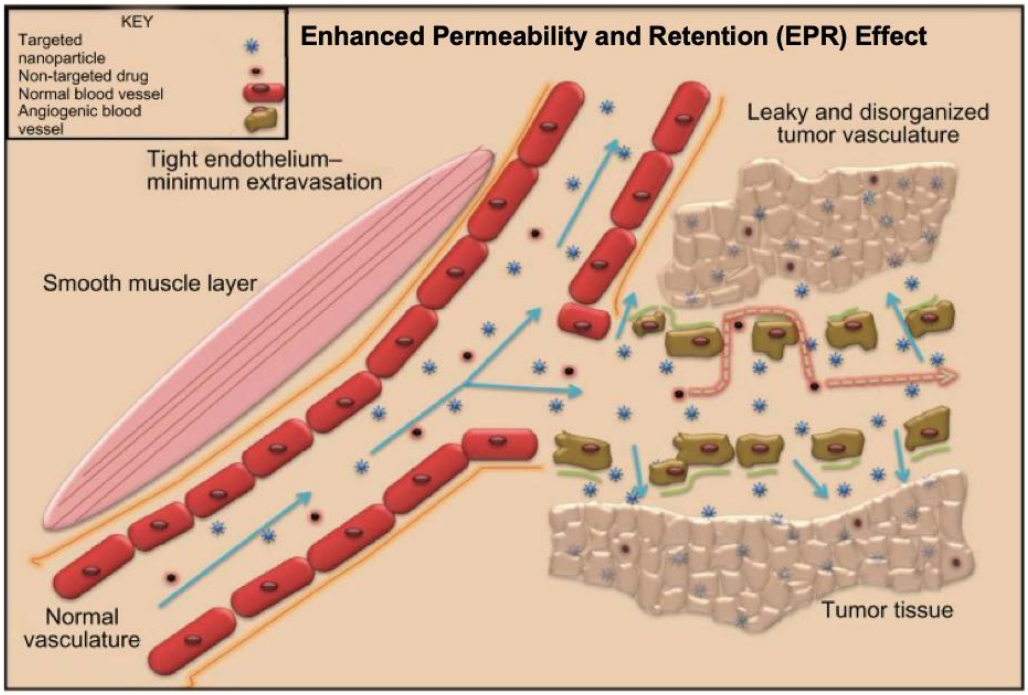

Figure 1: Schematic depiction of the mechanism behind the EPR effect. The illustration also shows how ligand-functionalized nanoparticles (blue) accumulate in the tumor tissue to a higher degree than their unfunctionalized analogues (black/red) due to ligand-receptor binding. (Figure adapted from ref. 6)

this class (exclusively liposomal systems) have been approved for commercial use by the Food and Drug Administration (FDA)[12]. In order to benefit from both active and passive targeting strategies, researchers have also been exploring ligand-functionalized nanoparticle drug delivery systems for anticancer treatments (fig. 1). Many drug candidates of this class are currently in clinical trials.

Though most of the research in this area so far has been done on liposomal systems, alternative materials are also being explored for targeted drug delivery, for instance bioinspired elastin-like polypeptides (ELPs)[13].

1.2 Elastin-/Resilin-like Polypeptides

1.2.1 Properties and Applications

The ELP is a biopolymer derived from mammalian tropoelastin consisting of repeats of the pentapeptide VPGXG where X is any amino acid except proline[14–16]. ELPs are temperature-responsive polymers and form phase-separated aggregates in aqueous media upon heating above their critical transition temperature T_t (a lower critical solution temperature (LCST) phase transition, fig. 2a/b)[16]. The phase transition of ELPs is usually completely reversible and T_t can be influenced by a variety of different factors such as polarity of the guest residue X, number of pentapeptide repeats, ELP concentration, N- and C-terminal conjugates and salt concentration in the media (fig. 2b/d)[17–21].

Resilin-like polypeptides (RLPs) are in many ways similar to ELPs: They are also temperature-responsive, repetitive biopolymers which have been inspired by a natural protein – this time the

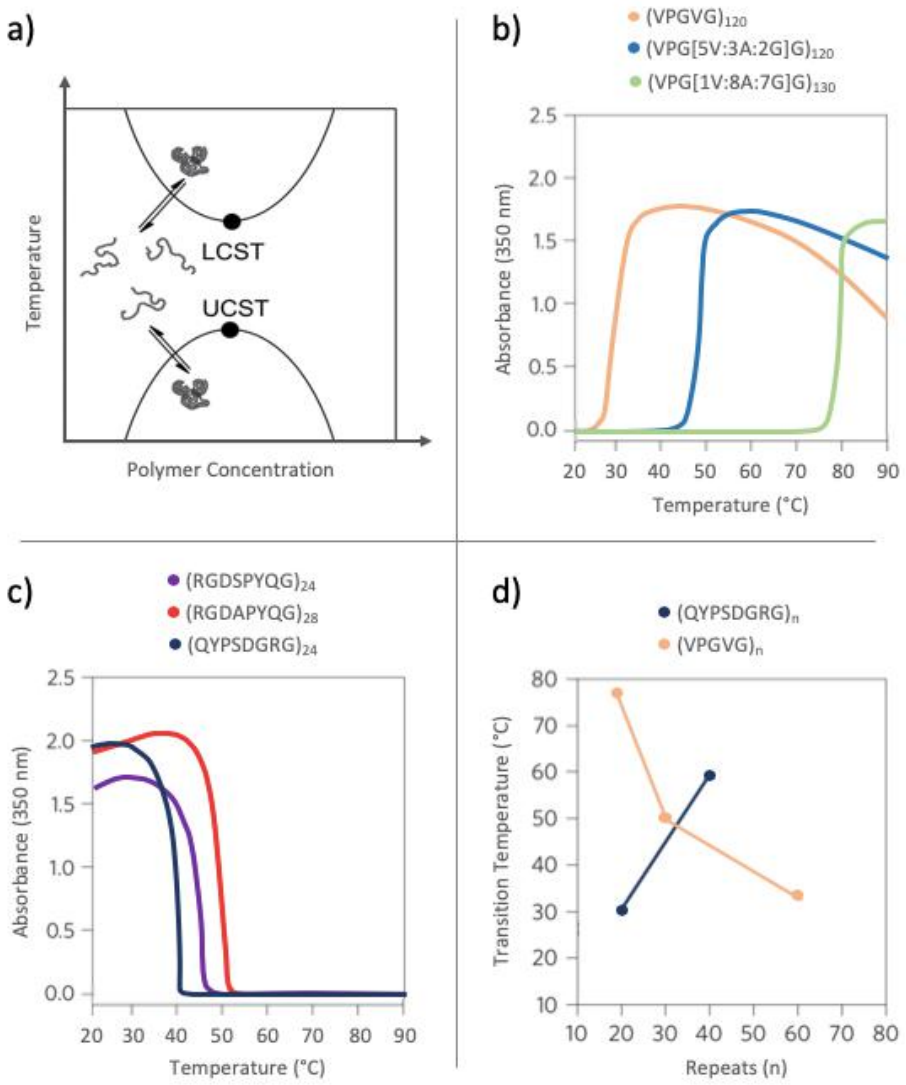

Figure 2: **a)** Phase diagram showing both LCST and UCST transitions of a (bio)polymer solution. **b/c)** Turbidity plots for different ELP (**b**) and RLP (**c**) sequences. Changing the ELP guest residue or RLP sequence has a significant effect on the transition point. Panel **d** furthermore shows that T_t can be influenced by the number of ELP and RLP repeats. (Figure adapted from refs. 18, 22 and 25)

inspiration came from rec-1 resilin in *D. melanogaster*[23–25]. Unlike ELPs, RLPs undergo both a lower as well as an upper critical solution temperature (UCST) phase transition meaning that they become soluble upon heating above $T_{t,UCST}$ and then phase-separate again upon further heating above $T_{t,LCST}$ (fig. 2a)[26]. As the UCST phase transition typically occurs in a more physiologically relevant temperature range than the LCST transition, we will exclusively focus on the former for the remainder of this master thesis (fig. 2c). Analogously to ELPs, the transition point of RLPs can also be influenced by a variety of factors such as their amino acid sequence, the number of repeats or the RLP concentration (fig. 2c/d)[25,27]. RLPs are way less established as a biopolymer class such that no defining amino acid sequence can be provided at this point. Generally, RLPs have hepta- or octapeptide repeats, are rich in proline and glycine and have a zwitterionic nature[25].

As ELPs and RLPs are highly biocompatible materials and can be very easily functionalized with a targeting ligand using genetical engineering techniques, substantial research has been done in optimizing these materials towards biomedical applications[13,28–30]. In comparison to lipids and synthetic polymers, these biopolymers furthermore have a greatly decreased risk of developing toxicity issues and also benefit from improved pharmacokinetics[31,32]. So far, a significant number of ELP-/RLP-based drug delivery systems has been developed, a few of which shall be briefly described in the following sections:

One feature which many ELP-based materials have in common is that they were engineered to have a transition temperature slightly above 37°C under physiological conditions[33–35]. Like this, one can use locally applied mild hyperthermia (39-42°C) to trigger the phase transition and further increase the specificity of the drug delivery system[36]. The power of this approach was first demonstrated by *Dreher et al.* in 2007 who achieved a two-fold increase in intratumoral ELP concentration as a result of local, hyperthermia-induced ELP precipitation[33]. A few years later, two somewhat similar systems were reported with ligand-targeted diblock copolymers. In both these systems, the hydrophobic ELP block was engineered to have a transition temperature slightly above 37°C. Like this, locally applied hyperthermia triggered the self-assembly into micelles which then displayed the ligands multivalently and thus had up to five-fold increased cellular uptake in comparison to unassembled controls[34,35].

Another property which is often sought in liposomal and polymersomal drug delivery systems is pH-sensitivity[37–39]. Responsiveness to changes in pH can help delivering drugs more efficiently as their carriers usually experience several pH gradients on their way to their target[40]. In 2012, *Callahan et al.* developed a histidine-bearing ELP diblock construct that disassembled upon entering the more acidic tumor tissue[41]. The locally released unimers were then able to penetrate the solid tumor more effectively than the assembled nanoparticles. In another study by *MacKay et al.,* a pH-sensitive bifunctional linker was used to chemically conjugate eight molecules of the hydrophobic anticancer drug doxorubicin onto one end of their hydrophilic monoblock ELP[42]. This conjugation strategy then not only led to nanoparticle assembly but to significant increases in *in vivo* potency.

RLPs on the other hand have so far mostly been explored in the context of mechanically active tissues due to their very good mechanical properties[28,43]. In one study by *Dzuricky et al.*, ELP/RLP-hybrid constructs were however also investigated in a drug delivery context[30]. More concretely, ligand-functionalized diblock constructs were used to target $\alpha_v\beta_3$-integrins which are often overexpressed on cancer cells. As the work by *Dzuricky et al.* was one of the cornerstones of the herein documented master project, their study will be presented in greater detail later on.

1.2.2 Cloning

One great advantage of ELP- and RLP-based materials is that they can be expressed recombinantly in *E. coli* bacteria and we thus in theory have absolute control over the length and the composition of the expressed proteins. For a long time, researchers however had great trouble getting precise control over the ELP sequence due to its repetitiveness. This changed in 2010

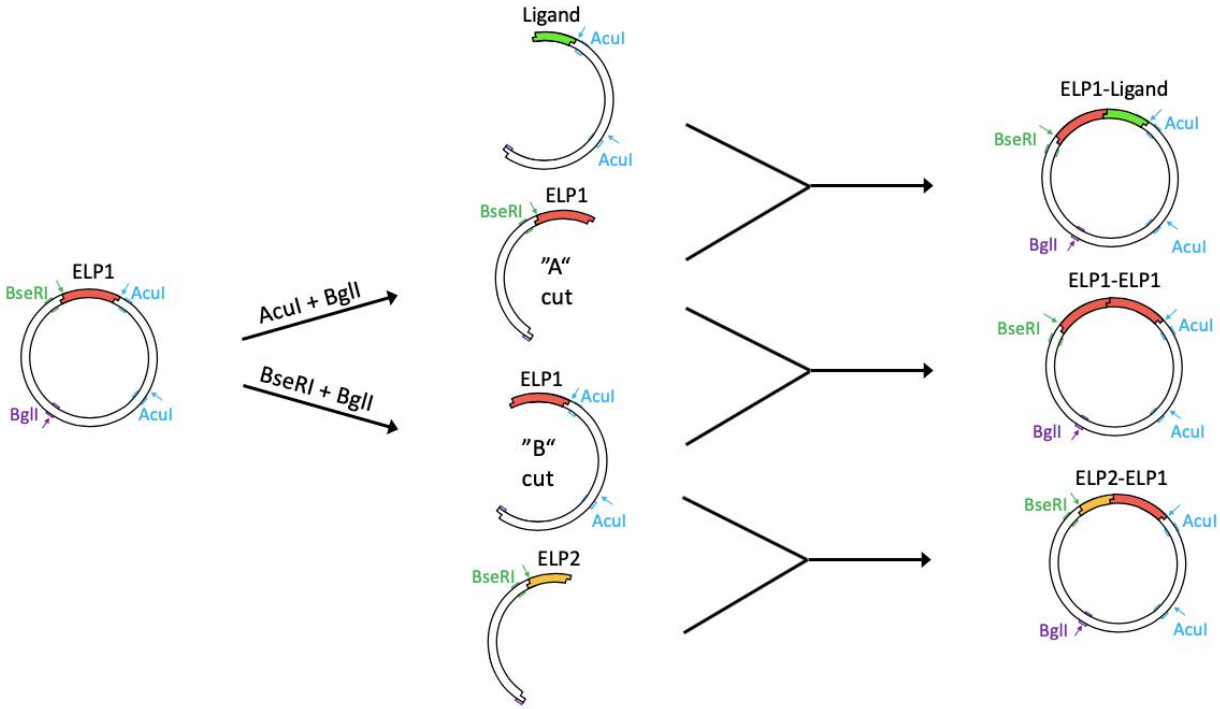

Figure 3: Schematic illustration of the PRe-RDL cloning process to grow and/or functionalize ELP/RLP constructs in an easy and controllable manner: In the first step, the pET-24a+ vector is digested with the restriction enzymes *AcuI/BglI* or *BseRI/BglI* to create the corresponding "A" or "B" cut respectively. By ligation of an "A" with a "B" cut – containing identical or different sequences of interest – the plasmid is reconstructed and can be subjected to a second cycle of PRe-RDL. Note that the colored lines on the plasmid represent the recognition sites and the arrows the cut sites of the respective restriction endonucleases.

when *McDaniel et al.* introduced a novel cloning strategy with which the ELP sequence could be controlled with so far unprecedented precision: Recursive directional ligation by plasmid reconstruction (PRe-RDL)[44].

PRe-RDL is a cloning procedure based on previous work from the research group of Prof. Ashutosh Chilkoti at Duke University[45]. It involves three different cut sites for restriction enzymes on a conventional pET-24a+ cloning vector: two identical sites for different restriction endonucleases immediately up- and downstream of the inserted construct (*AcuI*, *BseRI*) and a cut site for the enzyme *BglI* in the middle of the vector. By digesting the vector with *BglI* and for instance *AcuI* one can generate a "A-cut" of any ELP-/RLP-bearing plasmid which can then be reconstructed by ligation to the "B-cut" (digestion with *BglI* and *BseRI*) of any other (or the same) plasmid (fig. 3). Like this, ELPs and RLPs can be either grown or functionalized in a very controlled manner. Moreover, *AcuI* and *BseRI* are type IIs restriction enzymes which have their recognition sites several nucleotides away from the actual cut site. As a result, the reconstructed vector after one PRe-RDL cycle still only contains one cut site each without creating a new one at the linkage of the two ligated vector fragments. Like this, additional PRe-RDL cycles can be performed right away to further increase the size of the construct or to add ligands, linkers or other ELP/RLP blocks at either side.

1.2.3 Inverse Transition Cycling

As mentioned above, the thermal responsiveness of ELPs has been exploited many-fold in the context of drug delivery applications. In addition to this, the characteristic phase behavior of

ELPs provides another – way more fundamental – advantage for ELP-based materials: Their relative ease in purification by employing inverse transition cycling (ITC)[20].

This technique exploits the complete reversibility of the LCST phase transition observed for ELPs and ELP-based materials. In principle, ITC is a series of alternating “hot” and “cold” centrifuge spins (fig. 4). In the first step, the temperature of the cell lysate is significantly increased to force the ELP to undergo its phase transition and to precipitate out as insoluble aggregates. If the increase in temperature is not sufficient to trigger the phase transition, the T_t of the ELP can also be lowered by adding salts to the solution. In this state, the sample is subjected to a “hot” centrifuge spin at increased temperature after which the supernatant containing any soluble contamination is discarded. Next, the pellet is resuspended in cold water such that the ELPs are forced below their LCST transition point and become soluble again. Subsequently, the ITC cycle is completed by performing a “cold” spin and discarding the formed pellet to remove any irreversibly insoluble contamination. Like this, most ELP-bearing proteins can be purified to >95% purity in a fast and highly parallel way by only using a centrifuge and some salts.

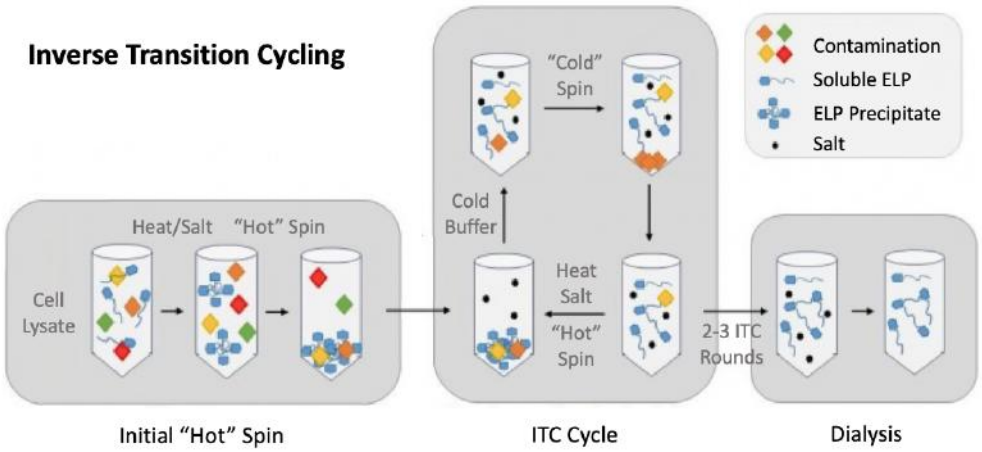

Figure 4: Schematic illustration of the ITC purification process for ELP-containing proteins. (Figure adapted from ref. 46)

Project I

Increasing the Stability and Potency of Ligand-bearing ELP/RLP Diblock Nanoparticles through chemical Crosslinking

2. Project Introduction

One very important variable for any self-assembled nanomedicine is its critical aggregation concentration (CAC). The CAC represents the amphiphile concentration at which the spinodal line in the phase diagram is crossed and above which the polymer mixture contains co-existing dilute and dense phases. In more illustrative terms: Nanoparticles (the dense phase) are only present at concentrations above the CAC whereas below the CAC, all amphiphilic molecules reside as unimers (the dilute phase) in a homogenous solution. Thus, determining the CAC is ultimately also a means to assess the stability of a certain nanoparticle architecture. It determines how far down a nanoformulation can be diluted down before the nanoparticles inevitably fall apart. Today, most ELP-based nanoparticles have reported CACs in the high nanomolar to low micromolar range which is comparable to systems based on synthetic polymers[29,34,47–49].

It is then also the CAC around which this first project is going to revolve. The main hypothesis we wanted to prove was that this parameter not only represents a characteristic variable for nanoparticle stability but also for the potency of the whole formulation. Based on the introductory paragraphs of section 1.1, it is clear that the CAC has a high influence on the targeting efficiency of nanoparticle formulations: Once the particles disassemble, they do no longer benefit from passive tumor-targeting through the EPR effect which significantly decreases their potency. But even if the particles are able to reach the tumor microenvironment intact, they are still dependent on the carrier remaining assembled as many of today's anticancer ligands require or at least benefit from multivalent display. As a result, it can be expected that many multivalent, ELP-based formulations with reported *in vitro* potencies in the low nanomolar or even picomolar range are actually significantly less potent *in vivo* due to CAC-dependent nanoparticle disassembly[50–52].

In the face of these drawbacks of self-assembled drug delivery systems we felt the need to develop an ELP-based nanocarrier with increased stability. To achieve this, we wanted to use chemical crosslinking – a strategy which had already been successfully employed to increase the stability of drug delivery systems based on synthetic polymers and lipids[53–56]. Like this, we hoped to completely remove the CAC from the equation and thereby significantly increase the nanoformulation's *in vivo* potency. In a clinical setting, this would then also lower the required dose per treatment which could ultimately help with dosage-dependent side effects as well as cytotoxicity[51,57].

2.1 Crosslinking Nanoparticles

In order to crosslink a nanoparticle, several different strategies have been pursued in the past: One crosslinking strategy which has been so far mostly exploited for carriers based on synthetic polymers is the use of polymerization reactions[53,54]. In this approach, the polymer building blocks are given one additional functional group which then reacts in a cross-molecular polymerization reaction once an initiator molecule is added to the solution. Another frequently used crosslinking strategy is the addition of multifunctional linkers which selectively react with certain functional groups on different polymer or lipid chains[55,56].

So far, the efforts on crosslinking ELPs have been mostly focused on the use of organophosphate crosslinkers which react with lysine residues[58–60]. Less explored alternatives to this approach include bifunctional linkers as well as enzymatic crosslinking with transglutaminase[61,62]. Though all these strategies succeeded in crosslinking ELPs, there still is a lot of room for improvement. Drawbacks include the cytotoxicity of some of the linkers, the addition of several experimental steps to the workload and the rather inefficient crosslinking for some of the approaches[63,64].

2.1.1 Crosslinking with *para*-Azidophenylalanine

In the face of this, *Costa et al.* developed a new technique to chemically crosslink ELP nanoparticles by introducing the unnatural amino acid *para*-azidophenylalanine (*p*AzF) into the ELP polypeptide sequence[65]. Introducing azide-bearing unnatural amino acids into proteins is an approach well established in the field of biomedical research as it allows for easy and selective bio-orthogonal conjugations via "click" chemistry reactions[66]. Using such amino acids to chemically crosslink a nanoparticle on the other hand is a novel approach.

In order to chemically crosslink molecules using an azide functional group, there principally exist two different approaches: Using a linker bearing "click" chemistry moieties or converting the azido group into a reactive nitrene by either UV irradiation or heat[67–69]. In the latter approach – the more interesting strategy for ELP crosslinking as it does not involve the addition of a reactive linker – the reactive nitrene group then readily inserts into any nearby C-H and N-H bonds[70,71]. Though this reaction is very non-specific, it has been proven to be a very fast and efficient way of crosslinking molecules[68,69].

Inspired by these results, *Costa et al.* designed and manufactured two different *p*AzF-bearing ELPs: a mono- and a diblock construct (fig. 5a)[65]. By varying the molecular ratio of the two native proteins in solution as well as the macro/microfluidic setup, they were able to control the

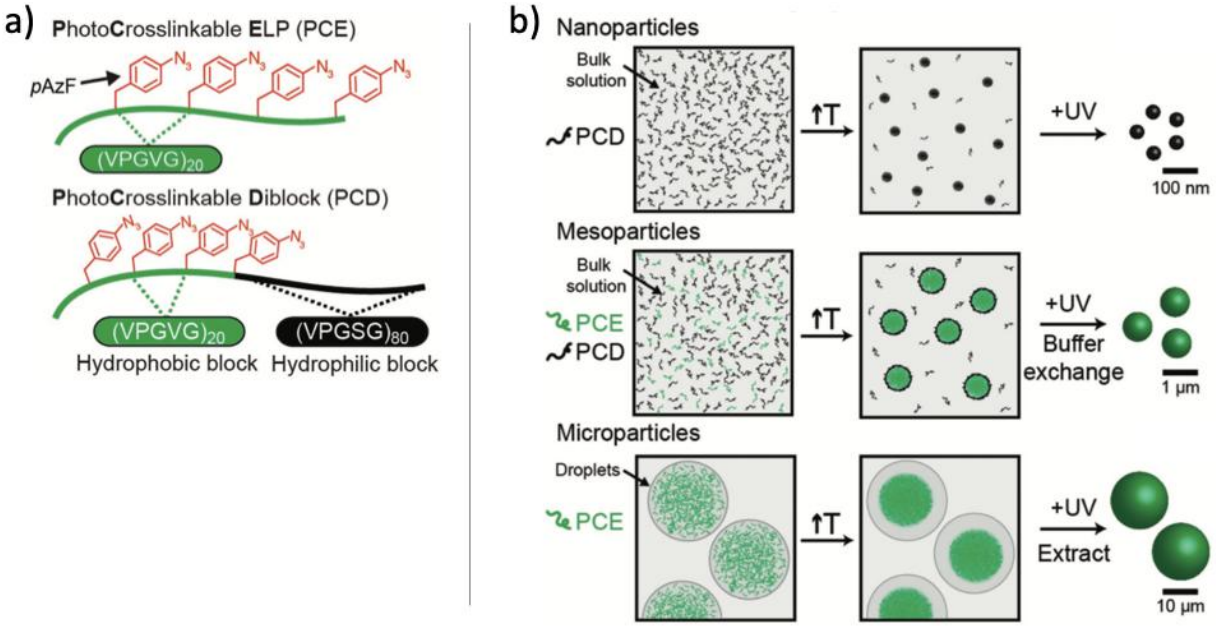

Figure 5: a) Illustration of the two different *p*AzF-containing ELP constructs *Costa et al.* designed for their crosslinking study. **b)** Schematic overview of the experimental strategies pursued to arrive at crosslinked particles spanning the nano- and micrometer ranges. (Figure adapted from ref. 65)

size of the formed aggregates upon heating above T_t. In this phase separated state, the particles were then crosslinked by exposure to UV irradiation. Like this, *Costa et al.* were able to isolate stable hydrogel particles spanning both nano- and micrometer scales (fig. 5b).

2.1.2 Expressing unnatural Proteins

One of the main reasons why unnatural amino acids are not used more frequently in biomedical research is that introducing them into a protein of interest poses a significant challenge. For a long time, the use of chemical synthesis was the only way researchers could selectively introduce unnatural amino acids to create (semi)synthetic peptides and proteins[72–74]. Due to the size limitations of chemical peptide synthesis, such artificially modified proteins were usually rather small with molecular weights below 10 kDa[72–74]. It was not until 1989, when the research groups of Peter Schultz and Richard Chamberlin independently published a more general strategy to selectively incorporate unnatural amino acids into proteins of any size[75,76]. Their approach was based on the fact that the amber stop codon UAG is relatively easily suppressed if a corresponding amino acid-loaded tRNA carrying the anticodon CUA is present[77]. Thus, they genetically introduced a UAG codon into their gene of interest, chemically prepared an unnatural amber-suppressor $tRNA_{CUA}$ carrying their unnatural amino acids of choice, added both to their *in vitro* expression systems and were then able to isolate unnatural versions of β-lactamase and a 16-residue polypeptide respectively[75,76].

Since 1989, numerous scientists have been working on improving this initial strategy with regard to both efficiency and ease of use[78]. More concretely, researchers quickly started introducing genetically encoded, orthogonal $tRNA_{CUA}$/aminoacyl tRNA synthetase (aaRS) pairs into their expression systems to expand the respective translation machineries. Like this, the expression systems could independently recognize and incorporate not 20 but 21 distinct amino acids without the necessary addition of an externally produced $tRNA_{CUA}$. Though this modification greatly increased the ease of use, the corresponding yields and specificities remained low due to imperfect orthogonality[78]. In the following years, researchers then spent a lot of time optimizing the individual components required for unnatural amino acid incorporation:

One of the key components was the aaRS enzyme that should ideally exclusively recognize the unnatural amino acid of interest and efficiently load it onto the corresponding $tRNA_{CUA}$. With the help of high throughput screening techniques, the field has seen a great increase in aaRS specificity and efficiency in recent years[78]. The aaRS variant used by *Costa et al.* for instance recognized *p*AzF as a substrate while excluding 237 other unnatural amino acids[65,79].

The second component was the plasmid carrying the $tRNA_{CUA}$/aaRS pair. It had been shown that the architecture of the vector by itself already had a substantial influence on protein expression levels. For their ELP-crosslinking study, *Costa et al.* had used the vector pEVOL that had been published in 2010 by researchers around Peter Schultz[80]. This vector had been highly optimized for maximal protein yields and amongst others contained both a constitutively expressed and an inducible copy of the aaRS gene. Overall, the resulting pEVOL vector outcompeted expression levels of any previous tRNA/aaRS vectors by at least 250%[80].

Lastly, the expression system itself naturally also had a significant influence on the protein yields. In order to reduce crosstalk to a minimum, *Isaacs et al*. created the *E. coli* strain

C321.ΔA in which all naturally occurring UAG stop codons had been replaced by synonymous UAA codons[81]. Like this, UAG was converted into a truly "blank" codon without any assigned functionality. This not only improved the specificity for unnatural amino acid incorporation but also led to a significant decrease in doubling time for the genetically recoded strain[82].

Based on the good results *Costa et al.* had gotten from the combination of these three components, we decided to adopt their strategy analogously for the expression of our own *p*AzF-containing proteins.

2.2 Project Strategy

2.2.1 Nanoparticle Architectures

The nanoparticle-forming amphiphiles studied in this master project were based on the ELP/RLP diblock constructs initially described by *Weitzhandler et al.* in 2017. In this study, the RLP block consisted of repeats of the octapeptide QYPSDGRG whereas the ELP block had the standard VPGXG repeats[29]. As this particular RLP octapeptide had a relatively high $T_{t,UCST}$ the RLP block would typically reside below its transition temperature in its phase-separated state. By choosing ELP blocks that remained in solution at the same conditions, this diblock architecture then represented a highly amphiphilic molecule capable of self-assembly.

The goal of *Weitzhandler et al.*'s study was to investigate three different intrinsic variables of these ELP/RLP diblocks and their effect on the morphology of the self-assembled structures: The number of ELP repeats, the number of RLP repeats and the ELP guest residue X (fig. 6a). What they found was that generally, at least 40 RLP repeats were necessary to result in any self-assembly at all. Beyond that, an increase in RLP repeats, a decrease in ELP repeats and more hydrophobic guest residues all promoted the formation of elongated/worm-like micelles over their spherical analogues and vice versa (fig. 6b). Moreover, diblocks with the same RLP-to-ELP ratios resulted in particles different in size but identical in aspect ratio.

In a recently published follow-up study by *Dzuricky et al.* three of those ELP/RLP diblocks were picked and further investigated for targeted drug delivery applications: The non-assembling RLP_{20}-$ELP_{A/G,80}$, the sphere-forming RLP_{40}-$ELP_{A/G,80}$ and the worm-forming RLP_{80}-$ELP_{A/G,80}$ (fig. 6c)[30]. All three constructs were then functionalized with a variant of the tenth type III domain from human fibronectin (Fn3) which naturally binds to integrin cell surface receptors, though with very low affinities[83]. The variant that *Dzuricky et al.* used was taken from a study by *Richards et al.* whom improved the selectivity and efficiency of Fn3-binding to $\alpha_v\beta_3$-integrins – a cell surface receptor that is often overexpressed on tumor cells[84,85]. Of all the Fn3 variants *Richards et al.* had developed, *Dzuricky et al.* chose a rather weakly binding version. They chose this particular variant as they were expecting significant multivalency benefits upon display on their ELP/RLP particles which might not be detectable if they used a variant with a high unimer binding affinity. And indeed, both self-assembling ELP/RLP diblocks showed significantly increased cellular uptake in comparison to the non-assembling RLP_{20}-$ELP_{A/G,80}$ construct[30]. Moreover, their cell uptake studies also showed that the worm-like micelles were taken up with greater efficiency than their spherical analogues (fig. 6d). This suggests that cell uptake for $\alpha_v\beta_3$-targeting nanoparticles might not only be multivalency- but also shape-dependent.

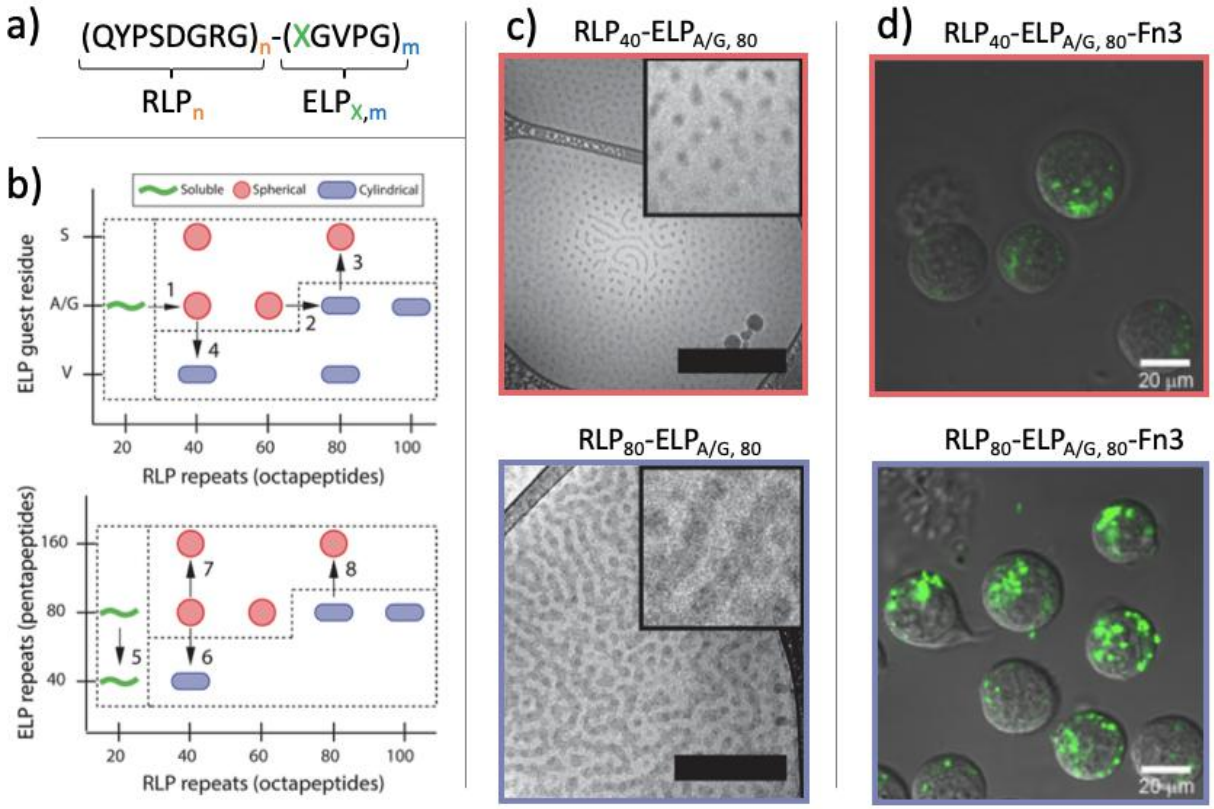

Figure 6: a) Short letter code representation of the RLP-ELP diblock constructs investigated by *Weitzhandler et al.* Note the three variables *n, m* and *X* which were analyzed for their influence on particle morphology. **b)** Schematic overview of the different particle morphologies observed for the tested constructs. Note that the top panel represents the construct RLP_n-$ELP_{X,80}$ and the bottom panel RLP_n-$ELP_{A/G,m}$. **c)** Cryo-TEM images of the unfunctionalized RLP_{40}-$ELP_{A/G,80}$ and RLP_{80}-$ELP_{A/G,80}$ constructs showing spherical and worm-like morphologies respectively. Scale bars both represent 500 nm. **d)** Confocal microscopy images of $\alpha_v\beta_3$-integrin-displaying K562 leukemia cells after co-incubation with the same two RLP-ELP diblock constructs carrying an integrin-targeting Fn3 domain and a fluorescence tag. (Figure adapted from refs. 29 and 30)

Based on the gathered knowledge from these two studies we decided to use the sphere-forming RLP_{40}-$ELP_{A/G,80}$ and the worm-forming RLP_{80}-$ELP_{A/G,80}$ constructs for the crosslinking studies presented in this master thesis. In addition to the two unmodified constructs – from here on referred to as DB-40 and DB-80 respectively – three additional constructs were engineered carrying evenly spaced *p*AzF residues in their core-forming RLP block: $(p\text{AzF-glycine-RLP}_{20})_2$-$ELP_{A/G,80}$ (≡ UAA2-40), $(p\text{AzF-glycine-RLP}_8)_5$-$ELP_{A/G,80}$ (≡ UAA5-40) and $(p\text{AzF-glycine-RLP}_{20})_4$-$ELP_{A/G,80}$ (≡ UAA4-80). The reason why two different *p*AzF-carrying constructs were designed for the shorter, sphere-forming diblock is that we were curious to see how many *p*AzF residues were necessary to achieve stable crosslinking of the nanoparticles.

2.2.2 Anticancer ligands

The main goal of this project was to show that crosslinked nanoparticles still retained their multivalency benefits at concentrations below the CAC of their native analogues and thus represented an ideal vehicle for highly potent, multivalent anticancer ligands. As a result, the chosen anticancer proteins and peptides needed to fulfil three basic requirements: Firstly, they needed to be subject to substantial increases in potency upon multivalent display. Secondly, the

multivalent form of these ligands should furthermore be potent enough to still have a detectable effect at concentrations below the CAC of the native DB-40 and DB-80 constructs. Based on the data published by *Weitzhandler et al.* we expected these CACs to lie at around 100 nM[29]. Lastly, the monovalent form should have no noticeable effect below the CAC. In order to prove the broad applicability of our crosslinked nanoparticles we decided to test a variety of different multivalent anticancer ligands: large protein domains, short peptides, ligands with intrinsic cytotoxic activity as well as tumor-homing ligands.

The most obvious candidate for our study was the $\alpha_v\beta_3$-targeting Fn3 domain previously investigated by *Dzuricky et al*. From surface plasmon resonance (SPR) experiments they had reported K_D values of 1 μM for the non-assembling constructs and 80 nM and 0.8 nM respectively for the multivalent particles which was perfect for our purposes[30]. Within the Fn3 structure, it is known that the FG loop and more particularly the therein contained tripeptide motif RGD is the most important for integrin-binding[84,86]. Moreover, there exist a great number of studies demonstrating the multivalency benefits of RGD-containing peptides, some even on ELP-based systems[35,87,88]. Motivated by this, we decided to not only include the Fn3 scaffold into our study but also its characteristic octapeptide GRGDSPAS[84].

The next ligand that peaked our interest was the Tn3 ligand developed by *Swers et al.* in 2013[52]. This is a protein domain derived from the third type III fibronectin domain of Tenascin C which they optimized to bind to the apoptosis-inducing death receptor 5 (DR5) with low nanomolar affinity. In their study they found that the Tn3 ligand actually requires multivalent display to become active at all: mono- and divalent forms failed to show any toxicity *in vitro* whereas tetra-, hexa- and octameric versions showed EC_{50} values in the low picomolar range. Moreover, the Tn3 ligand has already been successfully employed for ELP-based formulations which made this another good ligand candidate[89]. Similarily to the Fn3 ligand, we also here wanted to expand the experimental scheme by including a peptide with similar properties to the Tn3 domain. We found these in the $TRAIL^{mim/DR5}$ peptides developed by *Angell et al.* in 2009 which showed up to 10'000-fold increased binding affinities upon multimerisation[90]. The variant we ended up choosing for this study was a slightly modified version from a later follow-up study with a monomer K_D of 225 nM and a trimer K_D of 50 pM[91]. Lastly, we also decided to include the tumor necrosis factor-α–related apoptosis–inducing ligand (TRAIL) which is the standard reference for DR5-targetting ligands[92]. It has furthermore been shown, that TRAIL itself also experiences substantial multivalency benefits[93]. Generally, it is believed that a large contribution to the pronounced multivalency benefits for DR5-targeting systems comes from the downstream trimerization of ligand-bound DR5 receptors required for apoptosis induction[94,95].

In addition to these $\alpha_v\beta_3$-integrin- and DR5-targeting ligands, we included two more peptide ligands in our study: AHNP and polybia-MPI. The former is a 13-amino acid peptide targeting the ErbB2 receptor commonly overexpressed in breast cancer and for which there already exists some promising data on ELP-based systems[96,97]. The latter is a cationic, membranolytic peptide isolated from wasp venom which recognizes cancer cells by their systematically increased content of anionic phospholipids in their cell membrane[98]. As polybia-MPI is thought to elicit its effect via the "carpet" mechanism – a process that requires a high local concentration at the cell membrane – it seemed plausible that it would also highly benefit from multivalent display[99,100].

2.2.3 Hydrophilic linker

Particularly when working with short, hydrophobic peptide ligands on self-assembled drug delivery systems, there exists a considerable risk that the peptide will prefer to be buried in the particle core rather than being accessible on the vehicle's surface[101]. An approach to solve this problem is the introduction of a hydrophilic linker between the coronal end of the polymer/lipid and the peptide ligand. This strategy has been proven to work rather well for polymer micelles and liposomes[102,103]. Motivated by this, *Wang et al.* started working on a similar linker for ELP-based micelles. The peptide they used for their work was AHNP which had also shown poor exposure for lipid- and polymer-based systems[102,103]. After screening through many different linkers, they concluded that the introduction of a linker consisting of eight consecutive lysine residues followed by four aspartic acid residues worked best. Using this "K_8D_4" linker, they were able to increase cell uptake levels five-fold in comparison to an analogous linker-less construct[97].

Based on these findings, we decided to introduce this K_8D_4 linker into all of the functionalized constructs investigated in this master project.

Project Overview

Goal: Prevent disassembly of potent ELP/RLP nanoparticles and loss of their multivalency upon extensive dilution by chemical crosslinking

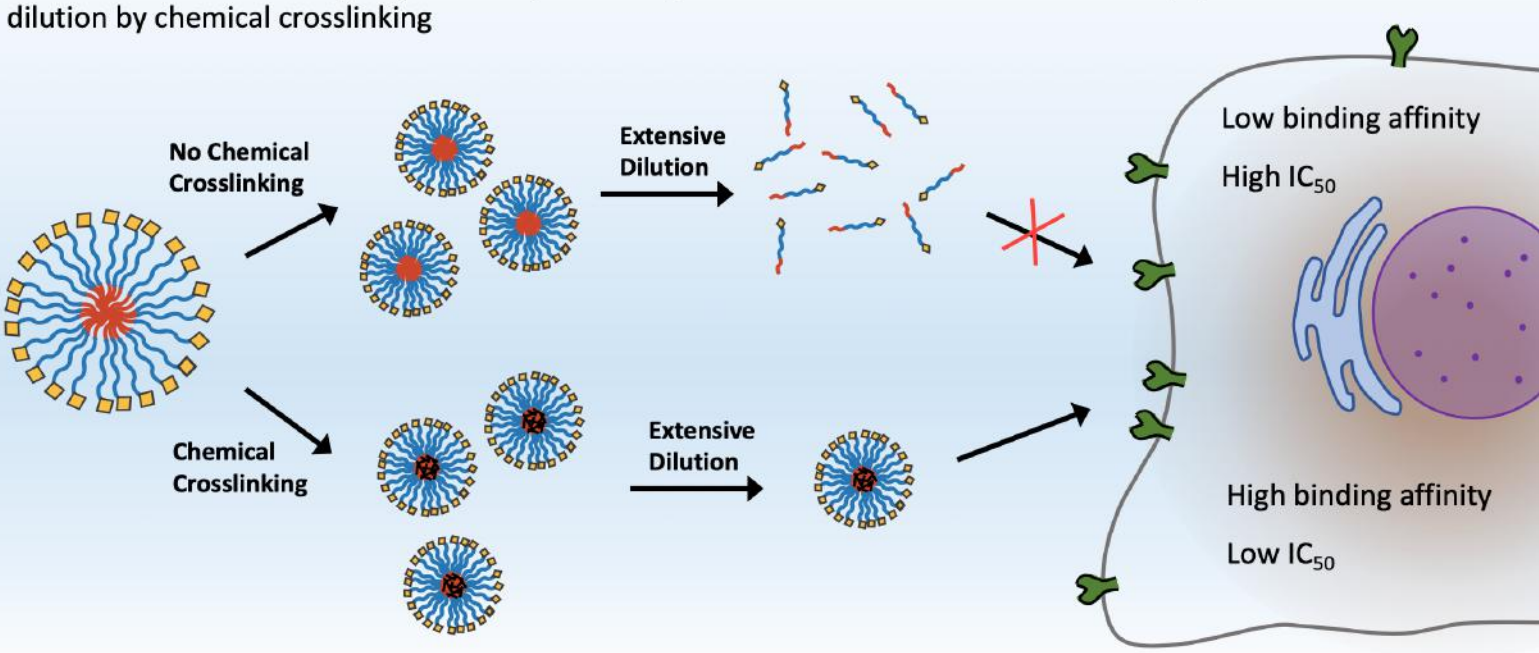

Construct Overview

Crosslinking with *p*AzF

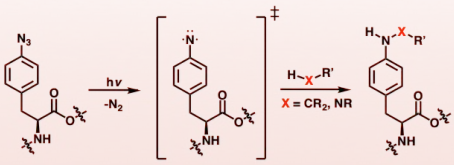

RLP/ELP sequences

No Linker

Hydrophobic burial

$GK_8G_3D_4G \equiv K_8D_4$

Ligand exposure

With K_8D_4-Linker

Diblock Architectures

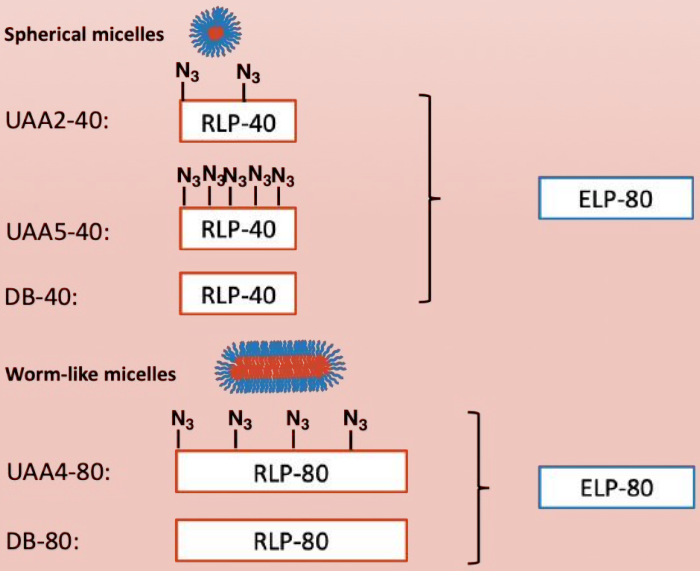

Ligand Overview

Ligand	# of aa	Cellular Target	Multivalency Benefit
AHNP	13	ErbB2 Receptor	N.A.
Fn3	96	$\alpha_v\beta_3$-Integrins	Decrease in K_d by more than 1000-fold
GRGDSPAS	8	Integrins	Significant decrease in K_d for comparable peptides
Polybia-MPI	14	Cell Membrane	Cell membrane disruption via „carpet"-mechanism, thus high local concentration is key
Tn3	105	DR5 Receptor	No anticancer effect for mono- and dimers of Tn3
TRAIL	184	DR5 Receptor	Multimerisation significantly increases cytotoxicity
TRAIL peptide	16	DR5 Receptor	Decrease in K_d by more than 1000-fold

Figure 7: Schematic illustration of both the overarching goal of this master project (**top**) as well as the different constructs employed in tackling this challenge (**bottom**).

3. Results and Discussion

3.1 Nanoparticle Crosslinking and Characterization

Before performing any experiments on the expected multivalency benefits, we first wanted to thoroughly investigate the effects of *p*AzF-introduction as well as nanoparticle crosslinking. For this, we started by characterizing solely our five different ELP/RLP diblock architectures without any C-terminal functionalization.

After expression and purification of the diblock constructs using ITC, the *p*AzF-containing constructs were crosslinked in solution by exposure to UV irradiation and characterized using dynamic light scattering (DLS). The measured hydrodynamic radii (R_H) showed that both the introduction of the unnatural amino acid into the polypeptide sequence and particularly the crosslinking process itself did influence the general size of the particles (tab. 1). Generally, both processes seem to have increased the measured radii with this effect being more pronounced for the worm-forming constructs. It seems largely unclear at this point why the crosslinking process by itself would lead to an increase in particle size rather than to just "freeze" the particles in their self-assembled state. One possible explanation is that this is simply an artefact of the DLS measurement due to the generally decreased fluidity of the more rigid particles after crosslinking.

Apart from changes in nanoparticle morphology we were particularly interested in the effect *p*AzF-crosslinking had on their stability. In order to evaluate whether the crosslinking process had indeed led to significantly increased stability, we exposed the particles to guanidine hydrochloride (GuHCl). GuHCl is a well-known denaturing agent that disrupts any inter- and intramolecular electrostatic forces and completely breaks down the quaternary, tertiary and secondary structure of most known proteins[104,105]. As covalent bonds – such as the ones formed by *p*AzF-crosslinking – however remain unaffected by GuHCl, the addition of this denaturing agent was expected to give us insights on the stability of our crosslinked nanoparticles.

To analyze this, we again turned to DLS: The gathered data proved that crosslinking had indeed yielded the desired stability increase (tab. 1). All crosslinked samples in GuHCl showed R_H values in the same general range as the ones previously measured in phosphate buffered saline (PBS). All native samples on the other hand resorted to complete unimerization upon exposure to GuHCl. As the R_H values for the crosslinked particles in GuHCl were generally larger than in PBS, the DLS data furthermore indicates a swelling behavior in the presence of the denaturing agent. This can most probably be attributed to the RLP core which is assumed to be completely collapsed in PBS but will however try to reach an elongated, random-coil morphology in the presence of GuHCl. Though the crosslinking does prevent particle disassembly, it cannot prevent the RLP core from expanding – at least not completely.

Lastly, the dataset also showed that the UAA2-40 and UAA5-40 constructs are identical both with respect to particle morphology as well as stability. It seemed that two *p*AzF residues per polypeptide chain were already more than sufficient to achieve stable crosslinking. To determine the minimal *p*AzF density required for stable crosslinking we mixed the UAA2/5-40 constructs with the *p*AzF-free DB-40 diblock and crosslinked them at a DB-40 fraction of 50, 60, 70, 80 and 90 percent. The following DLS characterization in 7.2 M GuHCl then showed that

R_H [nm]	DB-40	UAA2-40		UAA5-40	
		Native	Crosslinked	Native	Crosslinked
15 µM in PBS	28.0 ± 1.0	28.1 ± 0.2	29.8 ± 0.3	29.8 ± 0.2	34.3 ± 0.3
1.5 µM in 7.2 M GuHCl	0.7 ± 0.1	7.0 ± 1.1	54.1 ± 2.0	5.9 ± 1.6	52.1 ± 1.0

R_H [nm]	DB-80	UAA4-80	
		Native	Crosslinked
10 µM in PBS	39.9 ± 0.6	55.7 ± 2.3	86.2 ± 4.5
1 µM in 7.2 M GuHCl	1.0 ± 0.1	7.4 ± 1.9	138.1 ± 12.5

Table 1: DLS data for all ELP/RLP diblock constructs of this study in both native and crosslinked states. Exposure to the denaturing agent GuHCl resulted in complete disassembly for the native and *p*AzF-free constructs whereas a swelling behavior was observed for the crosslinked particles. Note that the particles were crosslinked at 15 and 10 µM respectively.

the cutoff lies at around one *p*AzF residue per ELP/RLP chain which in principle is a very intuitive result (fig. 8). Though the average DLS readings seemed to indicate that this is a rather abrupt transition, closer examination showed that this is not actually the case. In the range of one to two *p*AzF sites per diblock we also observeb a secondary population corresponding to the unimer fraction which continuously decreases in size as the *p*AzF density increases. In the face of these observations we decided to go for the safe option and use the UAA5-40 construct as the sphere-forming diblock for all future experiments.

As DLS only provides insights about the general size of nanoparticles but does not tell us anything about potential changes in morphology from one sample to the other, we decided to also perform cryogenic transmission electron microscopy (cryo-TEM) imaging to get a better idea of what our particles actually looked like.

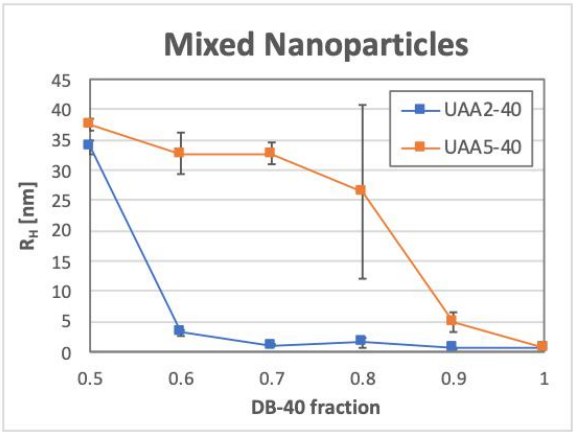

Figure 8: Stability comparison of the two *p*AzF-containing sphere-forming diblock constructs investigated in this study. The constructs were mixed with the *p*AzF-free DB-40 diblock at different ratios, crosslinked at 7 µM and their hydrodynamic radii recorded in 7.2 M GuHCl at 700 nM using DLS. Note that both *p*AzF constructs failed to create stably crosslinked particles once the *p*AzF-per-polypeptide ratio drops below 1.

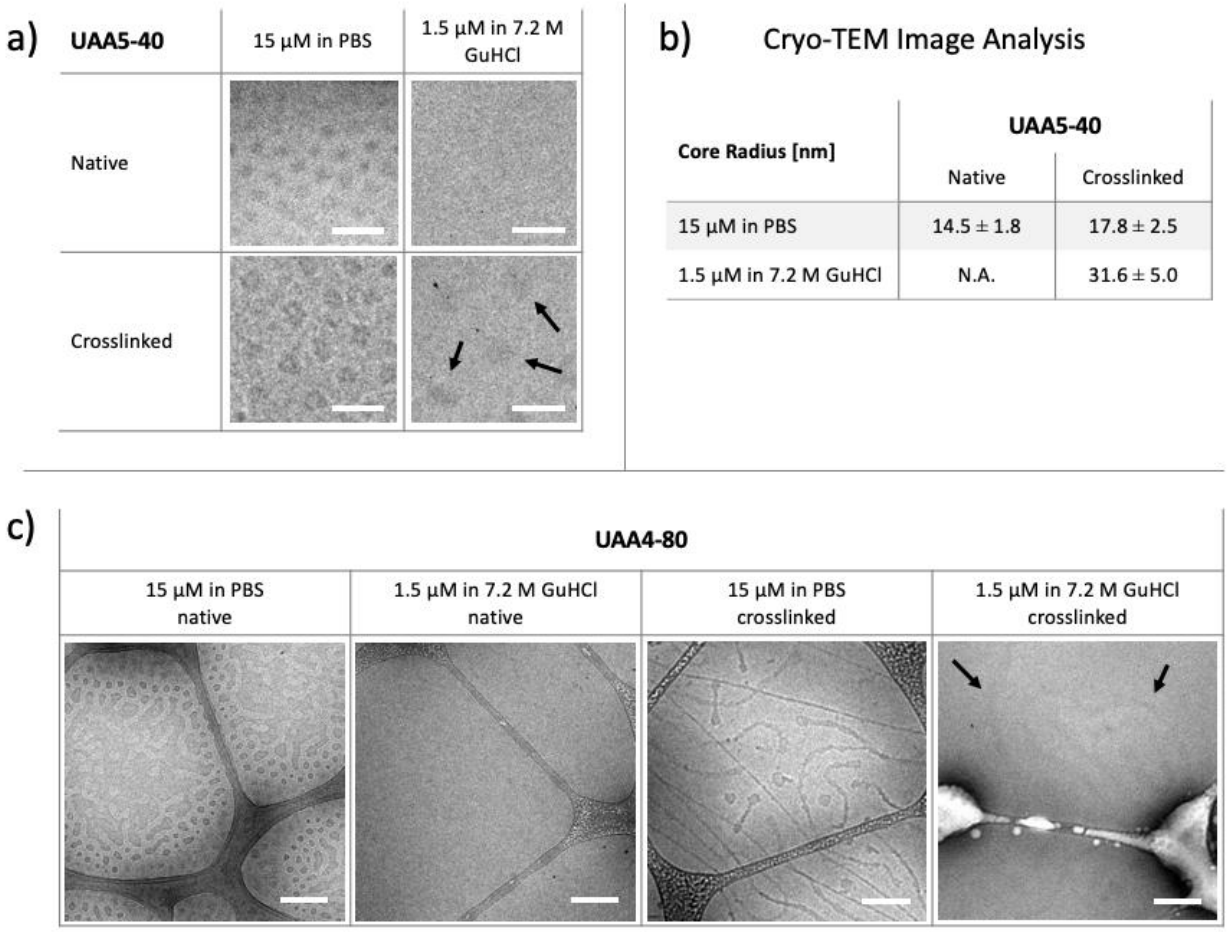

Figure 9: Cryo-TEM analysis of the *p*AzF-containing constructs UAA5-40 and UAA4-80: **a)** The presence of visible particles in GuHCl proved successful crosslinking for the UAA5-40 construct. Scale bars represent 100 nm. **b)** Image analysis of the core radii of the UAA5-40 particles showed significant swelling after GuHCl exposure. The particles appear smaller as only the collapsed RLP core has a high enough electron density for TEM. 100 particles were measured per condition. **c)** The UAA4-80 construct resided as highly elongated, flexible worms after crosslinking that retained their morphology even in the presence of GuHCl. Scale bars represent 300 nm.

For the sphere-forming diblock architectures, the resulting images more or less precisely confirmed what had been suggested by the DLS data: spherical particles which slightly increase in size upon exposure to GuHCl in the crosslinked regime and completely disassemble without prior crosslinking (fig. 9a). Moreover, the images also confirm the previous observation that the crosslinking process by itself already leads to a significant increase in particle size. The image analysis then resulted in particle radii significantly below the DLS values (fig. 9b). This can be explained by the previous observation that only the collapsed micelle cores have a high enough electron density to be imaged by TEM[106]. By subtracting the measured core radii from the corresponding R_H values from DLS we also see that indeed the changes in particle size upon GuHCl exposure stem mostly from swelling of the RLP core rather than the ELP corona.

As opposed to the sphere-forming diblocks, the cryo-TEM images of the worm-forming constructs showed a rather unexpected situation with worms several micrometers in length after crosslinking (fig. 9c). The surprise came less from the imprecise DLS data – as DLS assumes

spherical morphologies it systematically struggles with high aspect ratios – than from the divergence from the cryo-TEM images taken for the native sample. The particles in the image taken under native conditions were not nearly as elongated as the ones in the crosslinked state.

The most plausible explanation for this observation is that the particles in the native sample must have been subject to substantial rearrangements during sample preparation for cryo-TEM imaging. Indeed, it is known that self-assembled copolymer nanoparticles assemble and rearrange very quickly in fractions of a second[107,108]. Thus, the particles would have had plenty of time to interact and rearrange in response to being loaded on the TEM grid before being frozen. And as a 0.1-0.8 µm thick water film within a glow discharged carbon grid represents a very different environment than a regular sample vial, it seems very plausible that the micelles would have been subject to substantial rearrangement[109,110]. On the other hand, the so far collected data does suggest that the process of crosslinking by itself also has an effect on particle morphology. This could in turn indicate that the *p*AzF crosslinking does occur on a timescale greater than that of polypeptide rearrangement, allowing the particle to adopt new morphologies in response to the crosslinks being formed. In reality, the observed discrepancies in the TEM images most probably were the result of a combination of both effects.

In any case, the retention of the high aspect ratios in GuHCl confirmed that the crosslinking was also successful for the worm-forming constructs which was the main reason for performing cryo-TEM imaging in the first place.

Lastly, we also wanted to determine the CAC of the individual constructs in this first phase of the project as this was a value that would become very important later on. For this, the R_H values were measured with DLS over a dilution series from the mid-micromolar down to the low nanomolar range. The resulting hydrodynamic radii indicated that the sphere-forming constructs generally are more stable than their worm-forming analogues with the DB-40 and DB-80 constructs disassembling at low micromolar and mid-nanomolar concentrations respectively (fig. 10). Curiously, the mere introduction of crosslinking sites seems to dramatically decrease the

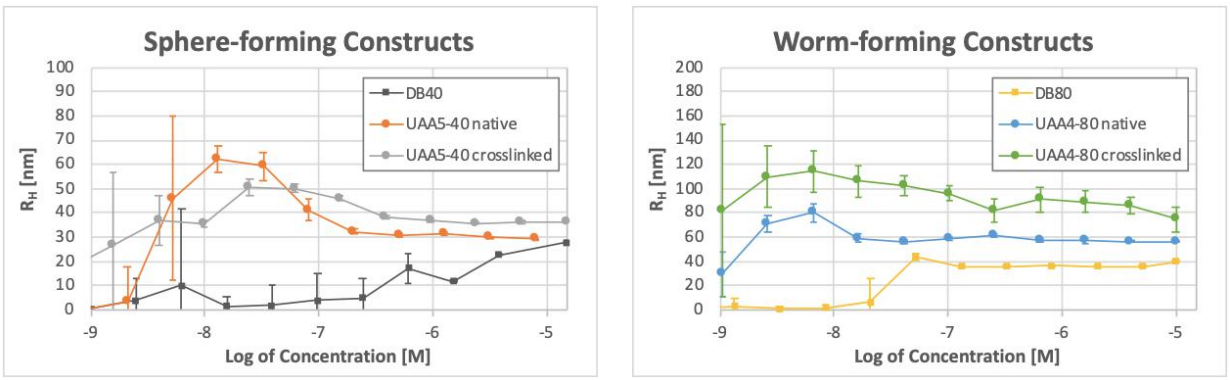

Figure 10: CAC determination of both sphere- and worm-forming constructs using DLS. Whereas the crosslinked samples showed stable nanoparticle readings down to the low nanomolar range – the estimated limit of detection for the DLS instrument – all other samples seemed to disassemble above that threshold. Generally, the worm-forming constructs had lower CACs than their spherical analogues and so do *p*AzF-containing constructs in comparison to analogous *p*AzF-free polypeptides. Note that all samples were prepared in PBS and that the error bars correspond to the standard deviation over 20 measurements.

CAC of both constructs down to the low nanomolar range. As the sample solutions were prepared freshly from lyophilized protein immediately before the measurement it seems unlikely that this could have been caused by partial crosslinking of the self-assembled particles, though this is a possibility. Another explanation is that the introduction of the *p*AzF residues significantly increased the T_t of the RLP block thereby also causing the CAC to decrease. As the aromatic *p*AzF residues are generally hydrophobic, it is expected that their introduction would cause such an effect. Whether the contributions from only four or five residues are however sufficient to explain the observed dramatic decrease in CAC remains questionable.

3.2 Ligand Screening

Based on the positive results from this initial crosslinking study, we felt prepared to move on to our functionalized constructs. As it would have been quite a lot of work to express, purify and characterize 14 different ELP/RLP diblocks we decided to perform the initial screening of our ligand candidates by just using the sphere-forming UAA5-40 construct as the basis. Only after the most promising ligands had been identified shall we then also include worm-forming construct in our experiments.

3.2.1 Expression and Purification

The first hurdle the ligands had to overcome was the expression and purification step. As the herein investigated constructs shall ultimately also be tested in *in vivo* experiments which generally require relatively large amounts of protein, good protein yields are certainly a desired if not required property.

Overall, most constructs expressed relatively well with the exception of the diblock carrying the TRAIL ligand. For this particular construct, the SDS-PAGE gel indicated a mass corresponding to an unfunctionalized UAA5-40 diblock but showed no band at the target mass of 88.2 kDa (fig. 11a). Based on the fact that also lanes for the other two larger protein ligands showed a band at this mass it seems possible that this band might correspond to a truncation product resulting from the repetitiveness of the K_8D_4 linker sequence. Why however the bacterial cultures still primarily produced the correct product for both the Fn3 and Tn3 constructs but completely failed to do so for the TRAIL ligand remains unclear at this point. In any case,

a)

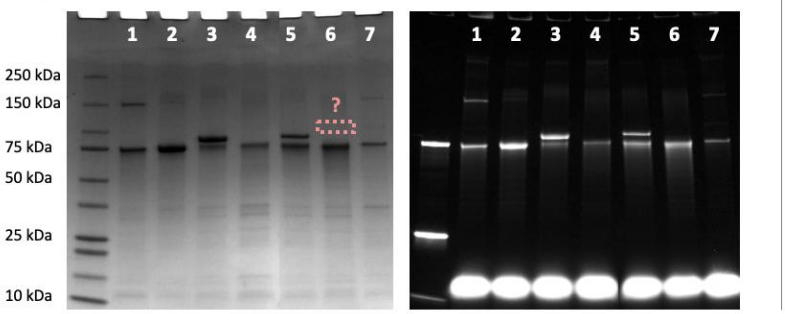

b)

#	Ligand	Protein yield [mg/L]
1	AHNP	18.0
2	GRGDSPAS	37.2
3	Fn3	24.6
4	Polybia-MPI	3.9
5	Tn3	13.9
6	TRAIL	11.3
7	TRAIL peptide	9.6

Figure 11: SDS-PAGE gels (**a**) and protein yields (**b**) after expression and purification of all UAA5-40-K_8D_4-ligand constructs of this study. Note that with the exception of the TRAIL sample (pink), all lanes show bands of the targeted mass. Note also that both AHNP and TRAIL peptide ligands contain cysteine residues due to which we see faint bands corresponding to the dimers on the SDS-PAGE gel.

it was decided to remove the TRAIL construct from the list of ligands and continue with the remaining six candidates. In terms of the observed side products for the Fn3 and Tn3 samples, we decided to continue with the characterization without further purification efforts. We expected the targeted multivalency effects to still occur even if a small fraction of the polypeptides within the nanoparticles were unfunctionalized.

Concerning the protein yields, all but one culture had produced around or above 10 milligrams per liter of liquid culture (fig. 11b). Though these are by no means great yields for recombinant ELP expression they were still considered satisfactory as both the *p*AzF incorporation and the complexity and size of the constructs were expected to reduce protein yields – particularly in an unoptimized protocol[30,65,97]. For the polybia-MPI construct the yield was significantly lower with only 3.9 mg/L which might become quite problematic when preparing for an *in vivo* experiment. Due to the fact that the material had already been produced and that it was present in sufficient quantities to perform cell experiments, the polybia-MPI construct was nevertheless subjected to the subsequent characterization experiments.

3.2.2 Particle characterization

The first step of the characterization process was to produce crosslinked particles for the functionalized diblock constructs and to analyze whether the attachment of the ligands had caused any significant changes in particle size. The following DLS analysis showed that the functionalization did not have any substantial influence on most of the nanoparticle architectures (tab. 2). The two exceptions were the constructs carrying the AHNP and TRAIL peptide ligands which showed significantly increased and decreased hydrodynamic radii respectively. The most plausible explanation is that this was caused by the decreased solubility observed for both these constructs which might have significantly altered the actual concentrations in solution. Whatever the reason was, it had no effect on the crosslinking process as the particles still remained stable after GuHCl exposure.

Crosslinked UAA5-40-K_8D_4-Ligand Constructs

	R_H [nm]	
Ligand	**7 μM in PBS**	**0.7 μM in 7.2 M GuHCl**
Unfunctionalized UAA5-40	34.3 ± 0.3	52.1 ± 1.0
AHNP	46.7 ± 0.4	51.4 ± 0.8
GRGDSPAS	33.9 ± 0.5	48.7 ± 0.7
Fn3	37.6 ± 1.2	46.4 ± 0.6
Polybia-MPI	33.8 ± 0.4	44.0 ± 1.1
Tn3	32.3 ± 0.4	47.8 ± 0.7
TRAIL peptide	27.6 ± 6.8	47.5 ± 6.7

Table 2: DLS readings for the crosslinked UAA5-40-K_8D_4-ligand constructs both in PBS and GuHCl. With the exception of the AHNP and TRAIL peptide constructs, all particles had a very similar size to that the unfunctionalized control. Nevertheless, all particles remained stable in GuHCl. Note that all samples were crosslinked at 7 μM.

3.2.3 Cell experiments

To determine which of the remaining six ligand candidates would be good candidates to investigate the hypothesized superiority of crosslinked nanoparticles for multivalent display, a series of cell experiments were performed. More concretely, the experiments were performed on four different cell lines depending on the type of ligand: The colorectal cancer cell line Colo205 was used for the apoptosis-inducing DR5-targeting ligands (Tn3 and TRAIL peptide), the breast cancer cell line SK-BR-3 was chosen to determine the potency of the ErbB2-binding AHNP ligand and two different variants of the leukemia cell line K562 (native and transfected with the gene for $\alpha_v\beta_3$-integrins, see *Dzuricky et al.*[30]) were employed to characterize the integrin-targeting constructs. The leukemia cell lines were also used to test polybia-MPI as its cytotoxicity had been reported for K562 cells[98].

In order for any ligand to represent a good candidate for the further multivalency studies, the tested crosslinked particles needed to show a detectable effect at concentrations both above and below the CAC of the sphere-forming ELP/RLP diblock construct.

Cell viability assays

The potency of the three cytotoxic ligands Tn3, TRAIL peptide and polybia-MPI was evaluated by performing cell viability assays on the respective cell lines at different concentrations. The subsequently collected data then showed that only the exposure to the Tn3-functionalized nanoparticles had led to any cell death (fig. 12). For the other two constructs the cells showed complete survival in the investigated concentration range. With an EC_{50} value of 470 pM the Tn3 sample still induced cell death at concentrations significantly below the CAC of the UAA5-40 construct. Therefore, the Tn3 ligand was identified as the first ligand candidate with all necessary properties for our multivalency experiments.

The failure of the other two ligands to cause any significant cell death might be attributed to different reasons: For the polybia-MPI ligand it seems most likely that we were simply wrong in hoping for significant multivalency benefits based on its hypothesized “carpet” mechanism driven by increased local concentrations. After all, the cytotoxicity experiments for polybia-

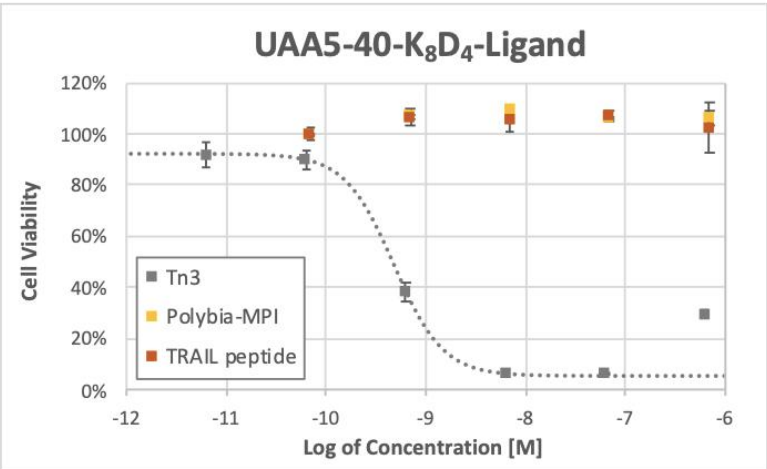

Figure 12: Cell viability assays testing the cytotoxicity of the polybia-MPI, Tn3 and TRAIL peptide ligands. All ligands were tested on crosslinked UAA5-40 nanoparticles and were co-incubated with Colo205 (Tn3 and TRAIL peptide) and K562 cells (Polybia-MPI) respectively over 24 hours.

MPI had been performed at 4 μM which still lies significantly above the herein tested concentrations[98]. For the TRAIL peptide on the other hand, it seems largely unclear as to what might have prevented this construct from having its reported effect on DR5-displaying cells. It seems plausible that its poor solubility – that was already hypothesized to have caused the altered DLS results – could be one of the reasons.

Cell uptake experiments

The first ligand evaluated through cell uptake experiments was the AHNP peptide. To also investigate possible non-specific uptake, all six ligands plus the unfunctionalized construct were tested on the SK-BR-3 cells. The resulting confocal images after 2 hours of co-incubation with the crosslinked, AlexaFluor-488-tagged nanoparticles at a concentration of 7 μM are shown in figure 13. To our disappointment, the images clearly showed that the AHNP functionalization did not lead to any increased cell uptake in comparison to the other ligands. Interestingly, all six functionalized particles however showed increased cell uptake in comparison to the unfunctionalized UAA5-40 control sample. This observation would then suggest that the increase in cell uptake was not actually caused by the ligands but the K_8D_4-linker instead. And indeed, the data from the publication initially describing the K_8D_4-linker shows that though the K_8D_4+AHNP construct had shown an 8-fold increase in cell fluorescence, the K_8D_4-functionalization alone had also resulted in a 50% increase in cell uptake[97]. Some other linkers with similar compositions had led to even greater increases in cellular uptake. Though this might explain the observed differences between the linker-carrying and linker-less particles of our own study, the cause of the AHNP inactivity remains unknown. Similarly to the TRAIL peptide ligand, it seems plausible that the decreased solubility observed for the AHNP construct might have made some contribution.

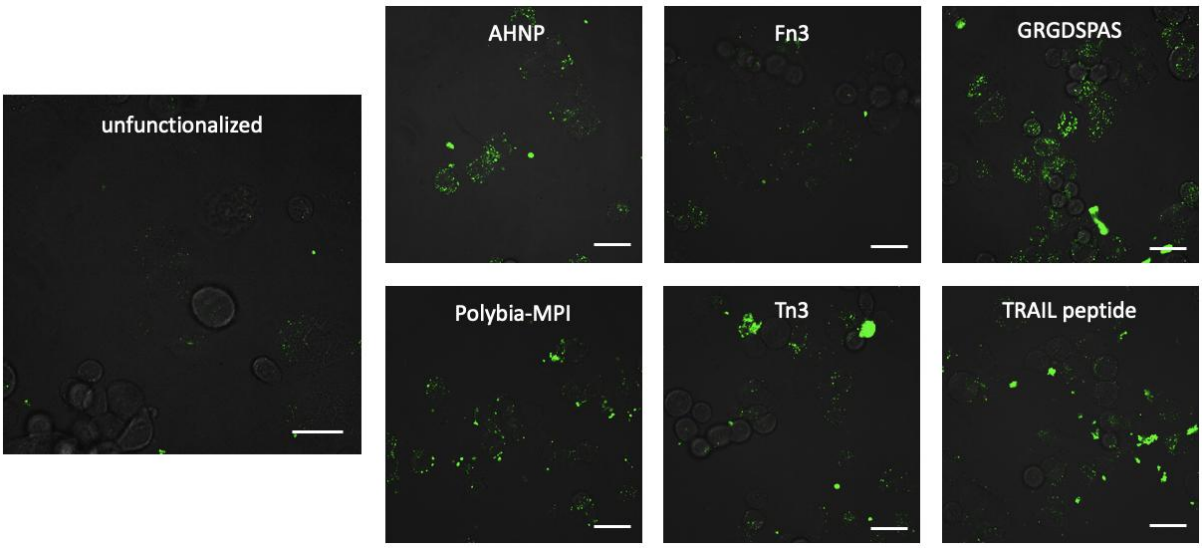

Figure 13: Confocal images from the cell uptake study on the breast cancer cell line SK-BR-3 using crosslinked UAA5-40-K_8D_4-ligand nanoparticles at a concentration of 7 μM. Apart from the Fn3 scaffold, all ligands showed significant increases in cell uptake in comparison to the unfunctionalized control. In theory, we would have expected this effect to only occur for the AHNP ligand as it targets the ErbB2 receptor on SK-BR-3 cells. Note that the brightfield contrast is extremely bad due to cell adhesion on the plate but there are around 20 cells in each of the images. Scale bars represent 30 μm.

Lastly, cell uptake experiments were performed on the two remaining leukemia cell lines. Here, three different ligands were tested: The integrin-targeting ligands Fn3 and GRGDSPAS as well as polybia-MPI. The latter was included as it seemed plausible that polybia-MPI – though it failed to lead to any cell death in the previous cell viability assay – might still have tumor-homing properties leading to increased cell uptake.

And indeed, the confocal images taken after 2 hours of co-incubation at 7 µM showed that the crosslinked polybia-MPI particles were actually internalized the most efficiently of all three functionalized constructs (fig. 14a). Furthermore, the two integrin-targeting ligands both showed increased uptake levels for the $\alpha_v\beta_3$-displaying K562 variants whereas no significant increase was observed for the native K562 cells in comparison to the unfunctionalized control. In the face of these positive results in the above-CAC regime, all three ligands were then also tested at a concentration of 70 nM – this time only on the $\alpha_v\beta_3$-positive cell line. Though this

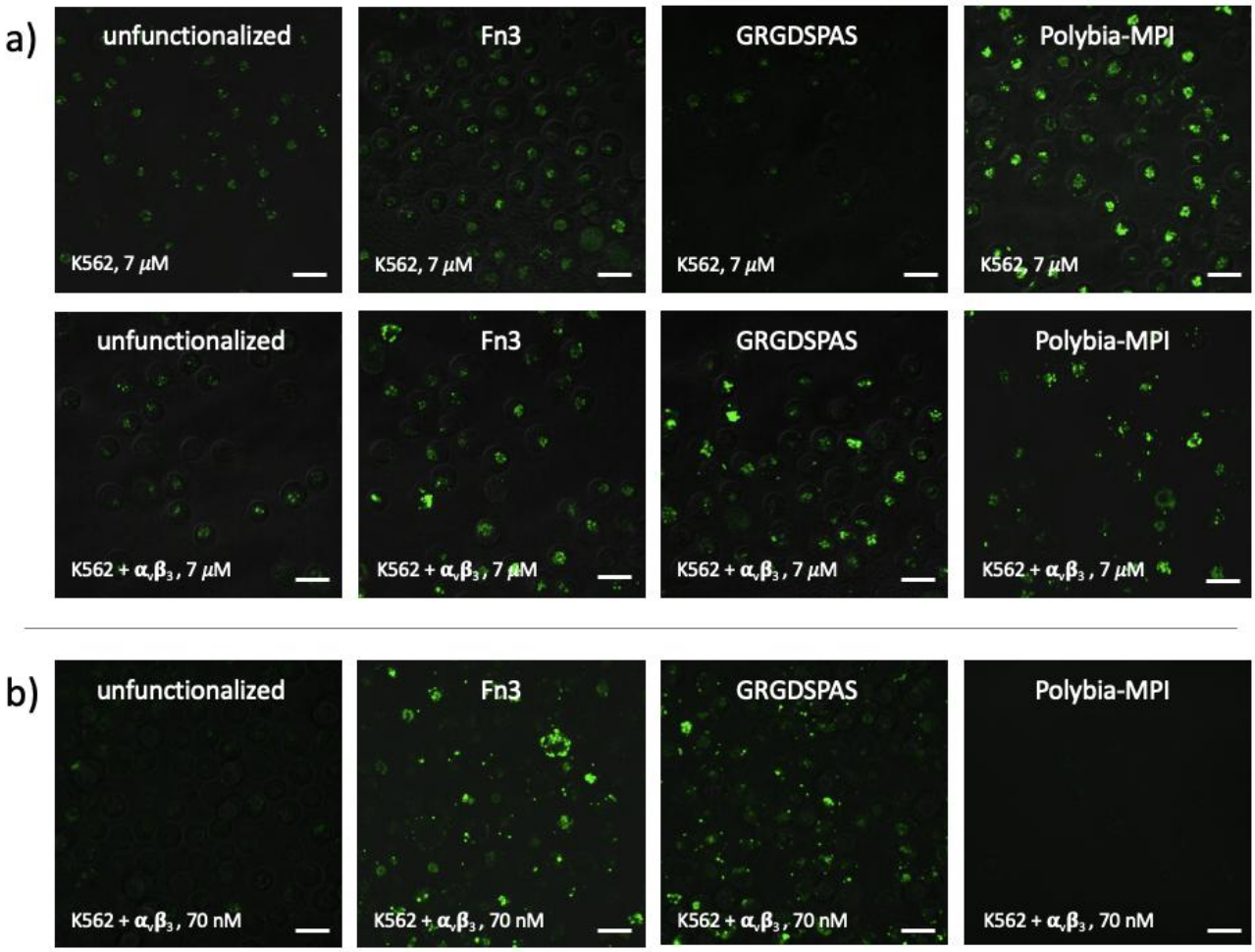

Figure 14: Confocal images of native and $\alpha_v\beta_3$-transfected K562 cells after co-incubation with AF488-tagged, crosslinked UAA5-40-K_8D_4-ligand nanoparticles. Scale bars represent 20 µm. **a)** Cell uptake studies above the CAC of the sphere-forming ELP/RLP diblock construct. Comparison between the native and $\alpha_v\beta_3$-transfected cell line indicates that the increased uptake observed for Fn3 and GRGDSPAS ligands was caused by integrin presentation on the cell membrane. Note that the cell uptake was not homogenous over the population which is due to previously reported variability in integrin expression levels for this cell line[30]. Polybia-MPI on the other hand showed increased uptake for both cell lines but more so for the native variant. **b)** Analogous experiments at concentrations below the CAC of the ELP/RLP carrier showed that both Fn3- and GRGDSPAS- but not Polybia-MPI-constructs still had increased cell uptake compared to the unfunctionalized control. Note that the brightness of these images has been adjusted in comparison to **a)** due to generally decreased uptake levels.

concentration might still lie above the construct's CAC, the limit of detection of the cell uptake assay (approx. 10 nM) did not allow us to dilute any further. The resulting confocal images then showed that both GRGDSPAS- and Fn3-carrying nanoparticles were still taken up in significant quantities whereas no increased cell uptake was observed for polybia-MPI (fig. 14b). It seemed that polybia-MPI did indeed not benefit from multivalent display to the degree we had hoped it would.

3.3 Multivalency Experiments

As only three of the screened ligands had shown activity both in the concentrated and dilute regimes, we decided to use all three of them for the subsequent multivalency experiments: GRGDSPAS, Fn3 and Tn3.

The goal of these experiments was to prove that crosslinked particles with multivalently displayed anticancer ligands were superior to their native analogues at concentrations below their CAC due to the retained multivalency. Moreover, we also hoped to see increased activity for the worm-shaped particles compared to their spherical counterparts as previously reported by *Dzuricky et al*[30].

3.3.1 Particle characterization

Before testing our hypothesis in cell experiments the newly expressed worm-like UAA4-80-K_8D_4-ligand constructs were characterized: Whereas the addition of these three ligands had not had any significant effect on the DLS readings for the spherical nanoparticles (tab. 2), a systematic decrease in hydrodynamic radius by approximately 20 nm was observed for the worm-like constructs (fig. 15a). In the face of these results and the fact that the R_H value does not represent particles with an elongated morphology very accurately, we turned to cryo-TEM to get a better idea of what might have caused this systematic change. The resulting images then clearly showed that the addition of the K_8D_4-linker and the three different ligands to the corona of the ELP/RLP diblocks had caused the proteins to take up a spherical rather than a worm-like morphology (fig. 15b-d). The radius of the particles in the cryo-TEM images was determined at between 20 and 40 nm (fig. 15e) which is in accordance to the DLS readings when also including the solvated and therefore invisible ELP corona (see section 3.1). Though spherical micelles like this had already been observed in some of the cryo-TEM images for the undecorated UAA4-80 construct, they had only been a minor side product (fig. 15f). The functionalization of these constructs now seems to have strongly shifted this equilibrium towards the low aspect ratio fraction.

As this change in particle morphology was equally pronounced for the short GRGDSPAS ligand as for the larger Fn3 and Tn3 protein scaffolds, it seems likely that the main cause of this effect was the introduction of the K_8D_4-linker. Due to the charge and hydrophilicity of this linker it seems reasonable that the attachment of such a peptide to the corona would generally promote lower aspect ratios. As none of the three remaining ligands was a short hydrophobic peptide with a high risk of hydrophobic burial, we decided to remove the K_8D_4-linker from all UAA4-80 and UAA5-40 constructs. The DLS characterization of the resulting linker-less UAA4-80 constructs then however showed unchanged hydrodynamic radii (fig. 16a). The subsequently recorded TEM images then confirmed that also the constructs without the K_8D_4-

Crosslinked UAA4-80-K_8D_4-Ligand Constructs

a)

Ligand	DLS R_H [nm]	
	7 μM in PBS	0.7 μM in 7.2 M GuHCl
Unfunctionalized UAA4-80	85.7 ± 6.7	93.5 ± 1.6
GRGDSPAS	47.7 ± 0.7	69.3 ± 1.2
Fn3	63.2 ± 1.8	70.8 ± 2.4
Tn3	49.6 ± 1.6	67.0 ± 0.9

e)

Ligand	Cryo-TEM Core Radius [nm]
GRGDSPAS	34.7 ± 6.1
Fn3	31.3 ± 5.1
Tn3	37.5 ± 4.4

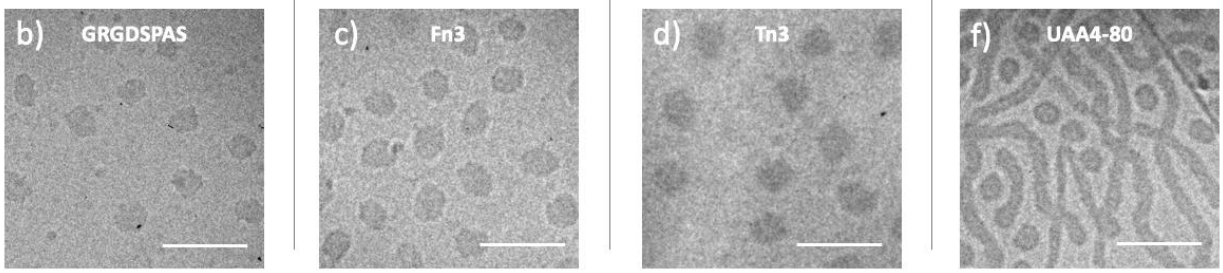

Figure 15: Characterization of the three different UAA4-80-K_8D_4-ligand constructs using DLS (**a**) and TEM (**b-e**). The functionalization of the UAA4-80 construct had a substantial effect on the particle morphology after crosslinking. Though spherical structures had also been observed for the unfunctionalized UAA4-80 construct (**f**) they were only a minor side product. The functionalized constructs now however formed exclusively this kind of structure. Note that all samples were crosslinked at 7 µM. All scale bars represent 200 nm.

linker still formed spherical rather than worm-like particles (fig. 16b-e). This however does not mean that the addition of the linker had no effect on the particle morphology: In fact, the UAA4-80-K_8D_4 nanoparticles showed an even greater decrease in size than the ligand-carrying constructs (fig. 16a/f). This would suggest that these worm-like architectures were just generally very sensitive to even the smallest coronal modifications.

Based on these findings we then tried to "save" the worm-like architectures by decreasing the ligand density on the nanoparticles. We achieved this by mixing the ligand-bearing constructs with the unfunctionalized UAA4-80 polypeptides before crosslinking. Even at a molar ratio of 1:1, the measured hydrodynamic radii however still remained close to the ones in figures 15 and 16. In a last attempt, we then also tried to crosslink the functionalized particles at lower concentrations – a strategy that had been shown to promote worm-like morphologies in previous, undiscussed experiments. Sadly, this approach also failed in recreating the architectures of the unfunctionalized UAA4-80 nanoparticles.

From a physicochemical standpoint it seems generally understandable that the strongly elongated structures observed for the crosslinked UAA4-80 construct would be highly metastable and could easily collapse into spherical morphologies. That the addition of only eight amino acids was however already sufficient to trigger the collapse of this 1048-aa construct was nonetheless a very surprising observation.

Though the worm-like morphology was lost at this point, the spherical UAA4-80 particles were still significantly larger than their UAA5-40 analogues which nevertheless represented an interesting basis for the following multivalency experiments.

Crosslinked UAA4-80-Ligand Constructs

a)

Ligand	DLS R_H [nm] 7 μM in PBS	0.7 μM in 7.2 M GuHCl
Unfunctionalized UAA4-80	85.7 ± 6.7	93.5 ± 1.6
UAA4-80-K_8D_4	37.7 ± 0.7	47.1 ± 2.3
GRGDSPAS	52.5 ± 1.6	71.3 ± 2.0
Fn3	44.4 ± 1.0	69.0 ± 1.5
Tn3	39.6 ± 2.4	59.6 ± 0.9

e)

Ligand	Cryo-TEM Core Radius [nm]
UAA4-80-K_8D_4	24.8 ± 2.9
GRGDSPAS	26.4 ± 3.8
Fn3	29.3 ± 4.3
Tn3	26.4 ± 3.4

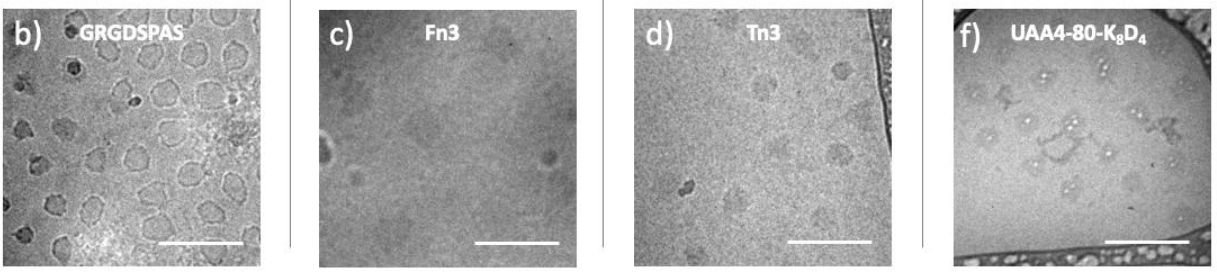

Figure 16: Characterization of the functionalized UAA4-80 constructs after removal of the K_8D_4-linker. Both DLS (**a**) and TEM (**b-e**) however showed that the resulting nanoparticles after crosslinking still had a spherical morphology rather than that of elongated worms. Characterization of the UAA4-80-K_8D_4 construct (**a, e, f**) indicated that attachment of the linker alone nevertheless also resulted in spherical morphologies. Note that all samples were crosslinked at 7 μM. All scale bars represent 200 nm.

3.3.2 DR5-targeting

Though the removal of the K_8D_4 linker did not end up promoting worm-like morphologies, the resulting particles were also no less worm-like than the ones carrying the linker. Thus, the first experiment to evaluate the multivalency benefits of crosslinked nanoparticles was to determine whether there were any differences in binding affinity between the linker-less and linker-carrying constructs. For this, cell viability experiments were performed with crosslinked versions of the Tn3-functionalized constructs. The resulting data showed that the K_8D_4-containing constructs were significantly more potent than their linker-less analogues for both UAA5-40 and

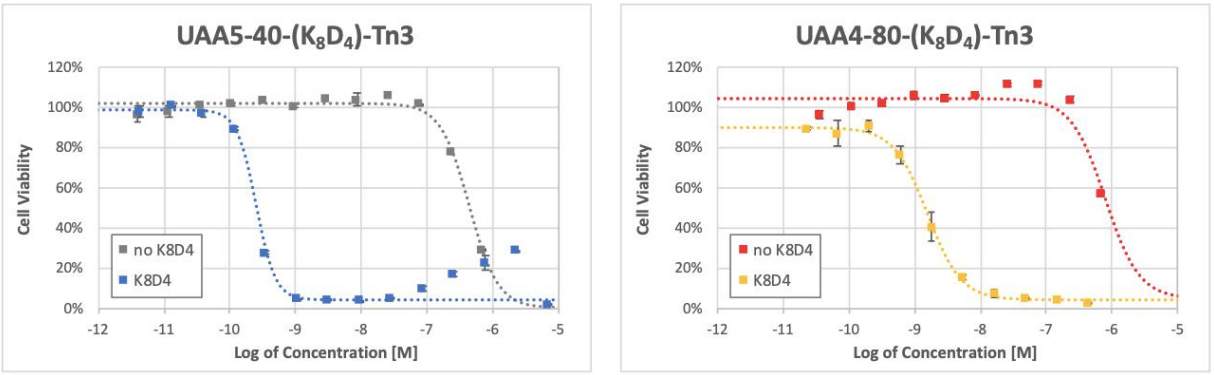

Figure 17: Cell viability plots comparing the potency of crosslinked constructs with and without the K_8D_4 linker. In addition to a strong increase in potency upon introduction of the linker, the plots also showed that of the K_8D_4-containing constructs, the one with the smaller UAA5-40 basis was significantly more potent.

UAA4-80 constructs (fig. 17). As the Tn3 ligand is a 104-aa protein scaffold and thus would generally not be expected to be at risk of hydrophobic burial, it seems very unexpected that the removal of the linker had such a dramatic influence on the particles' potency. One alternative hypothesis is that this highly charged linker generally helps with cell targeting through electrostatic interaction with the cell membrane. As the cell membrane – particularly in tumor tissue – is negatively charged, it seems plausible that the K_8D_4 linker with a net charge of +4 could facilitate cell targeting[98]. Regardless of what had caused this disparity, we decided to focus on the K_8D_4-containing constructs for all remaining experiments.

What the cell survival plots in figure 17 also showed is that the particles with a UAA5-40 basis were generally slightly more potent than the ones constructed from the UAA4-80 diblock. This observation was also somewhat counterintuitive as one would generally expect larger spheres with lower curvatures to have higher contact areas with the cell membrane and therefore bind to the displayed receptors more efficiently. The TEM images in figure 15 however showed that the particles with the UAA4-80 basis were no perfect spheres. This in turn indicated that the self-assembly and/or crosslinking of these constructs might be more chaotic than for the UAA5-40 particles and therefore might have also compromised ligand exposure.

Lastly, the cell survival curve for the crosslinked UAA5-40-K_8D_4-Tn3 particles in figure 17 almost perfectly matched the one from the previous ligand screening experiments (fig. 12b). Whereas it was satisfying to see that the data was reproducible, this also meant that the observed slight increase in cell survival for concentrations around 1 μM was in fact real. Though the cell survival still remained below 30% for all concentrations in this range, this was a rather inexplicable observation. What was particularly confusing is that the cell survival went back to 0% if the concentration was further increased up to 7 μM. As a result, this effect cannot be explained by a high concentration phenomenon such as nanoparticle clustering but was caused by something that exclusively appears at concentrations around 1 μM.

Moving on, we then performed analogous cell viability assays for the corresponding native constructs to quantify the multivalency benefits upon crosslinking. These experiments delivered some encouraging results: For both diblock architectures, the crosslinking significantly increased the potency of the respective nanoformulations (fig. 18a). For the functionalized UAA5-40 construct, the crosslinking decreased the EC_{50} value by more than three orders of magnitude. Moreover, a comparison of these cell viability results with the previously recorded CACs for the native UAA5/4-40/80 and DB-40/80 constructs then showed a profound correlation: The EC_{50} values of the native DR5-targeting constructs almost perfectly matched the CACs of the DB-40 and DB-80 constructs (fig. 18b). Though it was still largely unclear why the determined CACs for the UAA5/4-40/80 diblocks differed so greatly from their *p*AzF-free analogues, these observations strongly indicated that those differences were not actually real. It seemed highly unlikely that the near perfect correlation of the EC_{50} values and the CACs of the DB-40/80 constructs was just a coincidence and cannot be attributed to CAC-dependent particle disassembly. Therefore, this result then represents strong evidence for our hypothesis that the CAC is indeed one of *the* limiting factors to the potency of multivalency-benefitting ligands on self-assembled nanoparticles and that chemical crosslinking is a powerful means to overcome this issue.

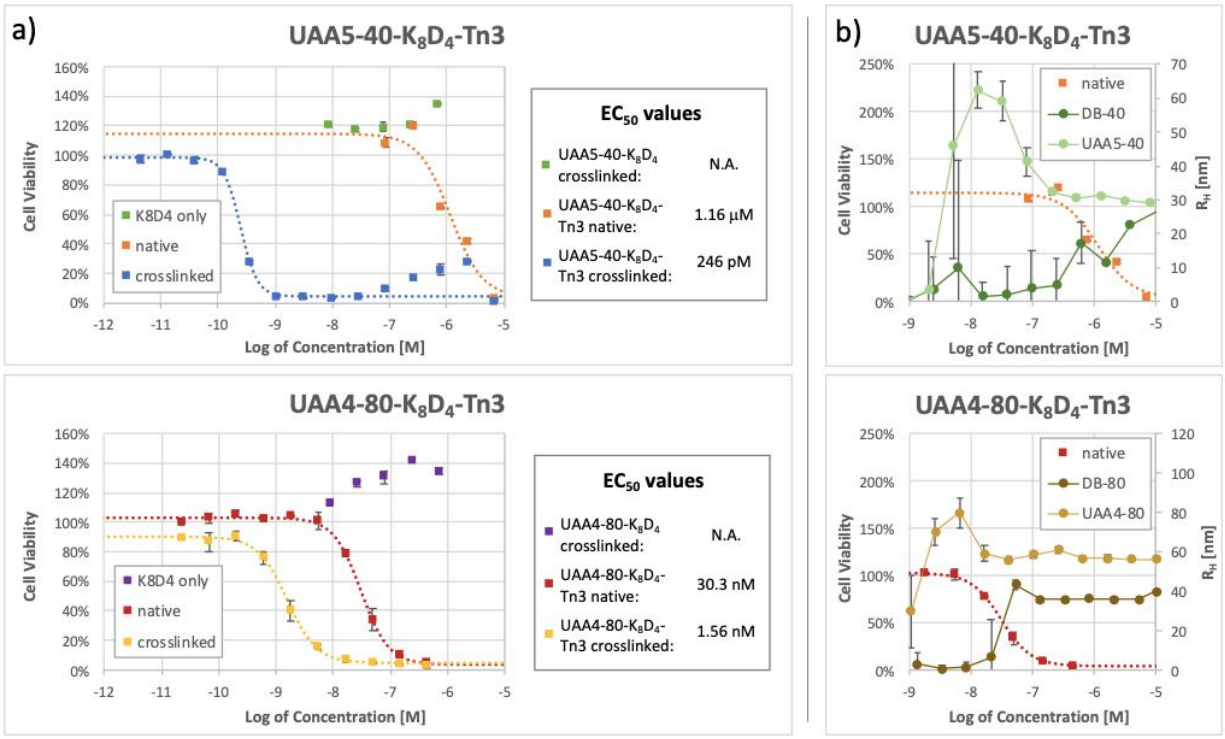

Figure 18: a) Direct comparison of analogous constructs in native and crosslinked states showed clearly that crosslinking increased the potency of the respective nanoformulations by several orders of magnitude. **b)** Comparison of the cell survival curve with the CAC data for both *p*AzF-free and -containing diblocks shows that the determined EC_{50} values almost perfectly matched the CAC of the *p*AzF-free DB-40/80 constructs. Thus, particle disassembly below the CAC seems to be the limiting factor in terms of potency for loosely self-assembled nanoparticles

In an additional follow-up experiment we then also investigated how different ligand densities on the crosslinked nanoparticles affected the overall potency. For this we prepared crosslinked particles consisting of both the unfunctionalized UAA5-40 diblock as well as the UAA5-40-K_8D_4-Tn3 construct at molar ratios of 1:3, 1:1 and 3:1. Subsequently performed cell viability assays with these constructs then showed that a decrease in nanoparticle functionalization down

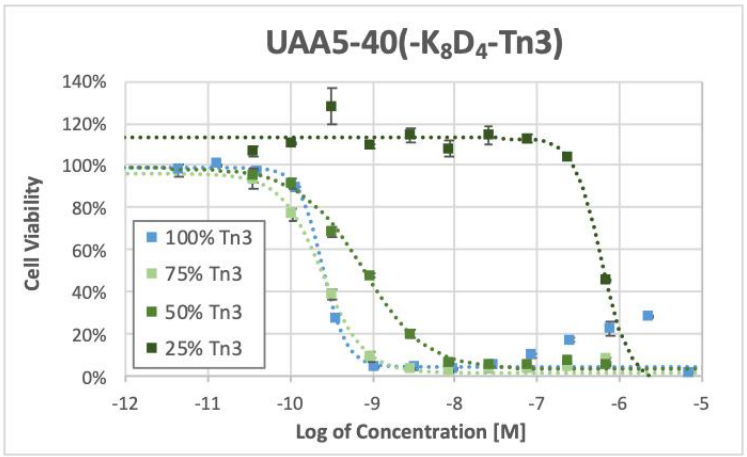

Figure 19: Comparison of the cytotoxicity of crosslinked UAA5-40 nanoparticles with different degrees of Tn3 functionalization. The nanoparticles were able to tolerate partial functionalization down to at least 50% without a major decrease in potency

to 50% only led to minor changes in potency (fig. 19). Only upon further reduction down to 25% functionalized ELP/RLP diblocks within the nanoparticles did the measured EC_{50} value significantly increase to the high nanomolar range. Due to the non-linearity of the observed trend, we can furthermore assume that the two constructs mixed readily and that the changes in potency are indeed a consequence of decreased ligand density on the nanoparticle surface. If we also consider that the UAA5-40-K_8D_4-Tn3 construct was not completely pure in the first place as it contained significant amounts of truncation product (see fig. 11a) these observations become even more promising. It seems that at least half of the Tn3 ligands on the fully functionalized nanoparticles could theoretically be removed without compromising the potency of the formulation. This then represents a good starting point for additional engineering of this system for instance towards bispecific nanoparticles.

3.3.3 $\alpha_v\beta_3$-Targeting

To be able to put the cellular uptake of our integrin-targeting constructs into context, we first determined the $\alpha_v\beta_3$ integrin levels on our two K562 cell lines using an anti-$\alpha_v\beta_3$ antibody. The resulting flow cytometry data then confirmed previous reports that the $\alpha_v\beta_3$ levels within the transfected cell line were far from homogenous (fig. 20a)[30]. The fluorescence intensity histogram indicated the existence of two subpopulations: A first, main population with low integrin expression comparable to that on native K562 cells and a second, smaller subgroup with high $\alpha_v\beta_3$ levels. In the previously published cell uptake study by *Dzuricky et al.* the $\alpha_v\beta_3$-displaying subgroup accounted for around one third of all the cells within this cell line[30]. In the herein presented study, this fraction however seemed to have dropped to a little more than ten percent – most probably a consequence of small differences in fitness during the cell culturing prior to the cell uptake experiments. As a result, the corresponding boxplots for the native and transfected K562 cell lines mainly differed in their value for the 90th percentile (fig. 20b). Based on this observation, we then decided to only analyze the flow cytometry data for the most strongly

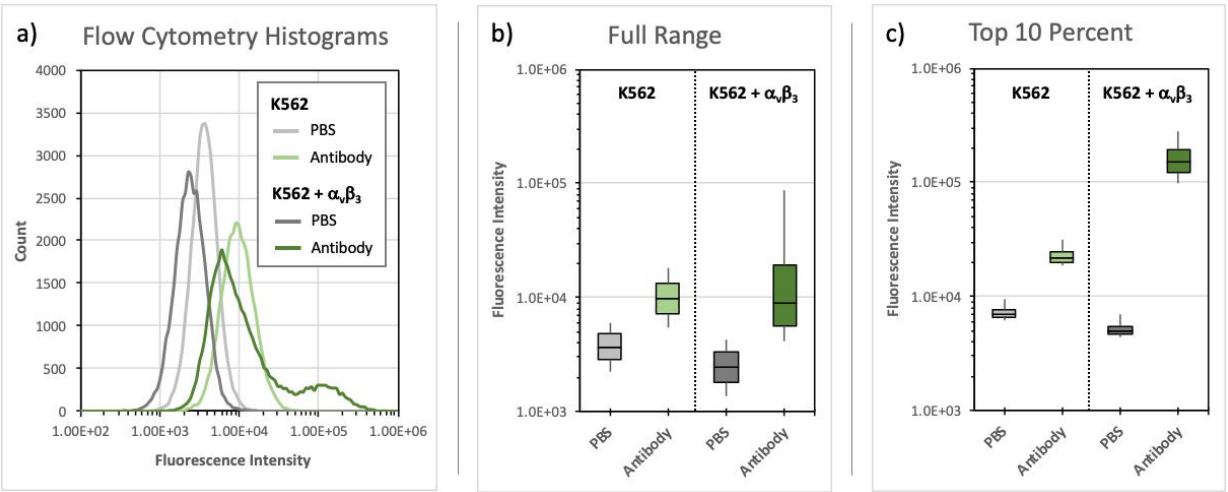

Figure 20: a) Flow cytometry data for the two K562 cell lines used in this study after 90 minutes of co-incubation with either PBS or 350 nM of an anti-$\alpha_v\beta_3$ antibody. Note that for the transfected cell line, we observe a secondary subpopulation with significantly increased fluorescence. This subpopulation accounts for 12.6% of all analyzed cells. **b/c)** Based on the observation in **a)** we decided to solely focus on the most strongly fluorescent 10% of the whole cell population through which the two cell lines can be differentiated more clearly in the boxplot diagrams. In the "full range" diagram (**b**), the boxes represent the 25th and 75th percentile and the bars the 10th and 90th percentile. In the "top 10 percent" diagram (**c**), they represent the 93rd/97th and 91st/99th percentiles respectively.

fluorescent ten percent of the cell population for all following cell uptake experiments. Like this, we hoped to statistically extract the small, $\alpha_v\beta_3$-displaying subpopulation within the transfected cell line and thus increase the sensitivity of our assay. At least for the antibody-experiments this minor adjustment seemed to work as it led to dramatically improved differentiation between the two tested K562 cell lines (fig. 20c).

A somewhat surprising observation from this first experiment was that the native K562 cells seemed to generally have higher background fluorescence than the transfected cell line. This is most easily explained by the transfection process lowering the expression levels of some weakly fluorescent proteins in favor of the $\alpha_v\beta_3$ integrin cell receptor. It is known that eukaryotic transfection also leads to some off-target alterations of protein expression levels compared to the parent cell line[111].

After initial characterization of the two cell lines of interest, we then moved on to analyze differences in cell uptake between these two K562 variants. We wanted to determine whether the constructs at hand actually showed specific rather than non-specific uptake. The following experiments with crosslinked nanoparticles then confirmed specific uptake for both integrin-tar-

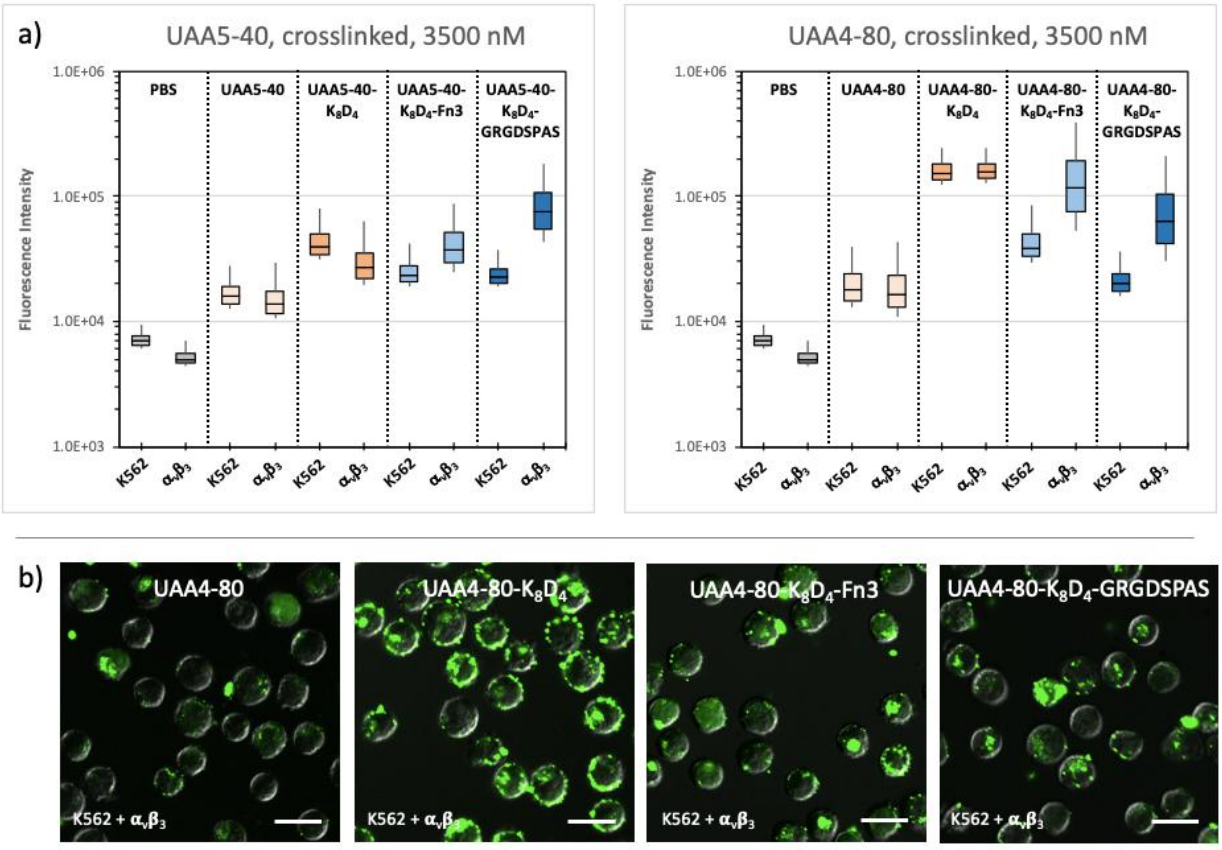

Figure 21: a) Flow cytometry data for cell uptake experiments comparing the two different K562 cell lines of this study. All cells were co-incubated with crosslinked AF488-tagged nanoparticles for 90 minutes. Only the particles carrying the Fn3 and GRGDSPAS ligands showed selective uptake for the $\alpha_v\beta_3$-displaying cell line. The boxes in the boxplot diagrams represent the 93rd and 97th percentile, the bars the 91st and 99th percentile. **b)** Confocal microscopy images of the $\alpha_v\beta_3$-transfected K562 cells after treatment with UAA4-80-based nanoparticles (identical samples as in **a**). Whereas the Fn3- and GRGDSPAS-carrying particles were taken up into the interior of the cells, particles with only the K_8D_4 linker showed peripheral aggregation at the cell membrane but no uptake. All scale bars represent 20 µm.

geting ligands on both diblock architectures (fig. 21a). Though all four constructs showed significantly higher cell uptake for the transfected cell line in comparison to its native analogue, the fluorescence levels of the native K562 cells were also significantly elevated. As also the native K562 cells treated with the unfunctionalized UAA5-40 and UAA4-80 constructs showed a significant increase in fluorescence over the PBS control, most of this response was probably due to non-specific cell uptake through (macro)pinocytosis[112]. The remaining delta in fluorescence levels is more difficult to explain. One possible explanation is that this was caused by other natively expressed cell receptors of the integrin family to which particularly the short GRGDSPAS ligand is expected to also show some affinity.

Another explanation for this effect is that it was caused by the addition of the K_8D_4 linker. The boxplot diagrams of the flow cytometry data showed very clearly that a functionalization with the linker alone led to a great increase in cell fluorescence – particularly for the larger UAA4-80 construct. Confocal microscopy then indicated that this fluorescence does however not originate from the interior of the cells – as is the case for the Fn3- and GRGDSPAS-carrying constructs – but from their periphery (fig. 21b). This observation then strongly supports the hypothesis from the previous cell viability assays that the K_8D_4-linker itself strongly interacts with the cell membrane and generally facilitates cell targeting.

Now that the two cell lines had been characterized and the specificity of the functionalized constructs to $\alpha_v\beta_3$ integrin was confirmed, we moved on to the actual multivalency experiments. Since serial dilutions analogous to the DR5-targeting constructs would have been too much work, we decided to characterize our constructs at only two different concentrations – one above and one below the CAC – in both native and crosslinked states. The concentration above the CAC was chosen to be 3.5 μM for both diblock architectures whereas the lower concentration was set at 70 and 30 nM respectively for the UAA5-40 and UAA4-80 constructs. Based on the CAC data, the lower concentration for the UAA4-80 constructs should have theoretically been set even lower than 30 nM to ensure complete disassembly. From previous cell uptake experiments we however knew that 30 nM would already be dangerously close to the limit of detection for this kind of cell uptake study. Thus, we chose not to decrease the concentration any further.

The subsequently collected flow cytometry data then showed similar levels of cell uptake for both native and crosslinked constructs in the high concentration regime whereas the crosslinked sample always outcompeted its native analogue at concentrations below the CAC (fig. 22). As expected, this trend was more pronounced for the UAA5-40 constructs than the larger UAA4-80 diblocks which can most certainly be attributed to incomplete disassembly of the native nanoparticles at 30 nM. Moreover, the improvements upon crosslinking for these integrin-targeting ligands in the dilute regime are not quite as impressive as for the Tn3-decorated constructs: Cell uptake was increased up to 6-fold for the former whereas for the latter, EC_{50} values dropped by at least a factor of 20. If one however takes into account that the Tn3 ligand *requires* multivalent display to elicit its effect and the Fn3 and GRGDSPAS ligand only *benefit* from multivalency, this less impressive improvements are no longer surprising. Generally speaking,

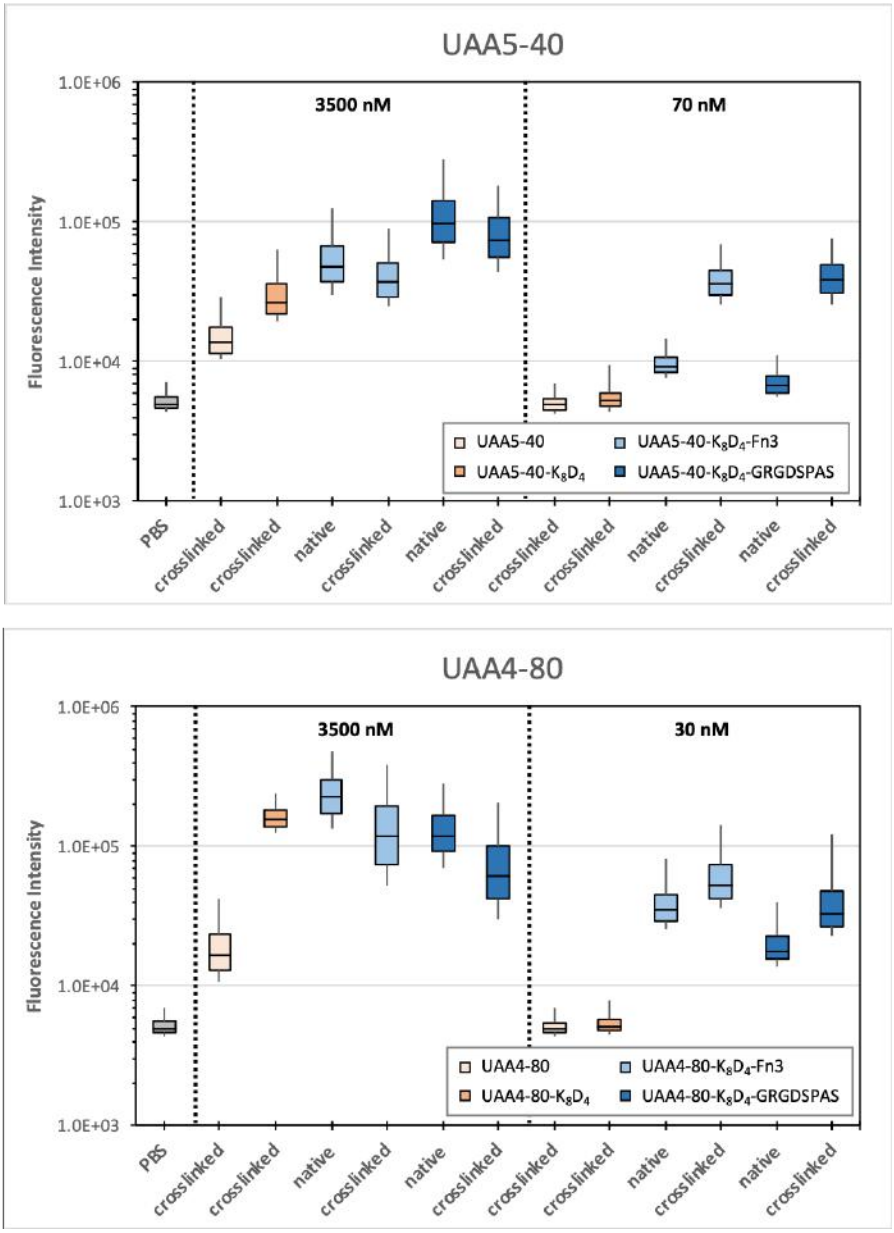

Figure 22: Flow cytometry data for the multivalency experiments on the $\alpha_v\beta_3$-transfected K562 cells. For both diblock architectures, crosslinking significantly increased cell uptake of Fn3- and GRGDSPAS-decorated nanoparticles in the sub-CAC regime. Note that the chosen concentration for the UAA4-80 construct was a compromise between its CAC (around 30-50 nM) and the limit of detection of the assay (around 10 nM). Thus, the improvements upon crosslinking were not quite as profound for the UAA4-80 constructs as they were for the UAA5-40 diblocks. The boxes in the boxplot diagrams represent the 93rd and 97th percentile, the bars the 91st and 99th percentile.

the experiments for the integrin-targeting constructs nevertheless provide further strong evidence that concentration-dependent disassembly of nanoparticles is a major limitation to efficient cell targeting and can be successfully overcome by chemical crosslinking.

In addition to the confirmation of our hypothesis, the results in figure 22 also led to two additional conclusions: Firstly, the boxplot diagrams indicated that at concentrations above the CAC crosslinking did also have an effect on cell uptake, though this time it was not a beneficial one. The observed slight decrease in uptake upon crosslinking was most probably due to a decrease in particle flexibility. Loosely self-assembled nanoparticles are expected to adapt to the cell

membrane topography more readily, thereby engaging more cell receptors and ultimately binding more tightly than their rigid, crosslinked analogues. Secondly, the boxplots also showed that the differences in cell uptake between the two tested ligands were rather slim despite the great difference in their size. Though the large Fn3 scaffold had a significantly increased monovalent binding affinity compared to the short GRGDSPAS peptide, they were affected equally by crosslinking. The only difference in the plots was that the cell uptake levels for the native Fn3-constructs in the sub-CAC regime were generally slightly higher than for their GRGDSPAS analogues. As those constructs are expected to have (mostly) lost their multivalency at this point, it makes sense that the construct with the worse monovalent binding affinity would also have the lower cell uptake levels. In the assembled state, the monovalent binding affinity then however only seems to make a negligible contribution such that the resulting nanoparticles were equally potent despite their very different ligands.

3.3.4 Surface Plasmon Resonance

Though we were ultimately most interested in the downstream effects of the treatment with crosslinked nanoparticles, we also wanted to investigate how chemical crosslinking affected the binding to the cell membrane receptors themselves. For this, we recorded the binding affinities of all our crosslinked and native diblock architectures using surface plasmon resonance (SPR). Generally speaking, we wanted to prove that the crosslinked nanoparticles had superior binding affinities in the sub-CAC regime compared to their native analogues whereas above the CAC, the K_D values should be comparable.

$\alpha_v\beta_3$-Targeting

To characterize the integrin-targeting constructs, we started by determining the K_D values of the UAA5-40-based constructs. This resulted in binding affinities of 3.3 nM and 20 nM for the Fn3 and GRGDSPAS ligands respectively (fig. 23a). These results generally matched the expectation that the short GRGDSPAS peptide ligand binds less strongly to $\alpha_v\beta_3$-integrin than the more complex Fn3 protein scaffold. For this latter ligand, the recorded K_D value for the crosslinked nanoparticles also lay significantly below the value reported by *Dzuricky et al.* for an analogous *p*AzF-free construct[30]. A closer look at the SPR sensograms then however raised some questions about the significance of these results. More concretely, we expected the main differences in binding affinities between these two ligands to stem from an increased off-rate for the GRGDSPAS nanoparticles. K_{on} which is mainly diffusion-driven was expected to be similar for both ligands[113,114]. In reality, the main reason for the increased K_D for the Fn3 construct however lay in vastly different association rates rather than differences in k_{off}.

Regardless of whether or not the differences between these K_D values were accurate, we can certainly say that SPR indicated binding for both crosslinked UAA5-40 constructs in the sub-CAC regime. For their native analogues on the other hand no binding was observed for the GRGDSPAS construct whereas some binding – though to a lesser extent than for the crosslinked samples – was measured for the Fn3 variant (fig. 23b). Based on the results from the cell uptake studies we had expected that the native Fn3 construct might show some binding due to its increased unimer binding affinity compared to the GRGDSPAS variant. At concentrations above the CAC, crosslinking had no significant effect on the binding affinities (fig. 23c).

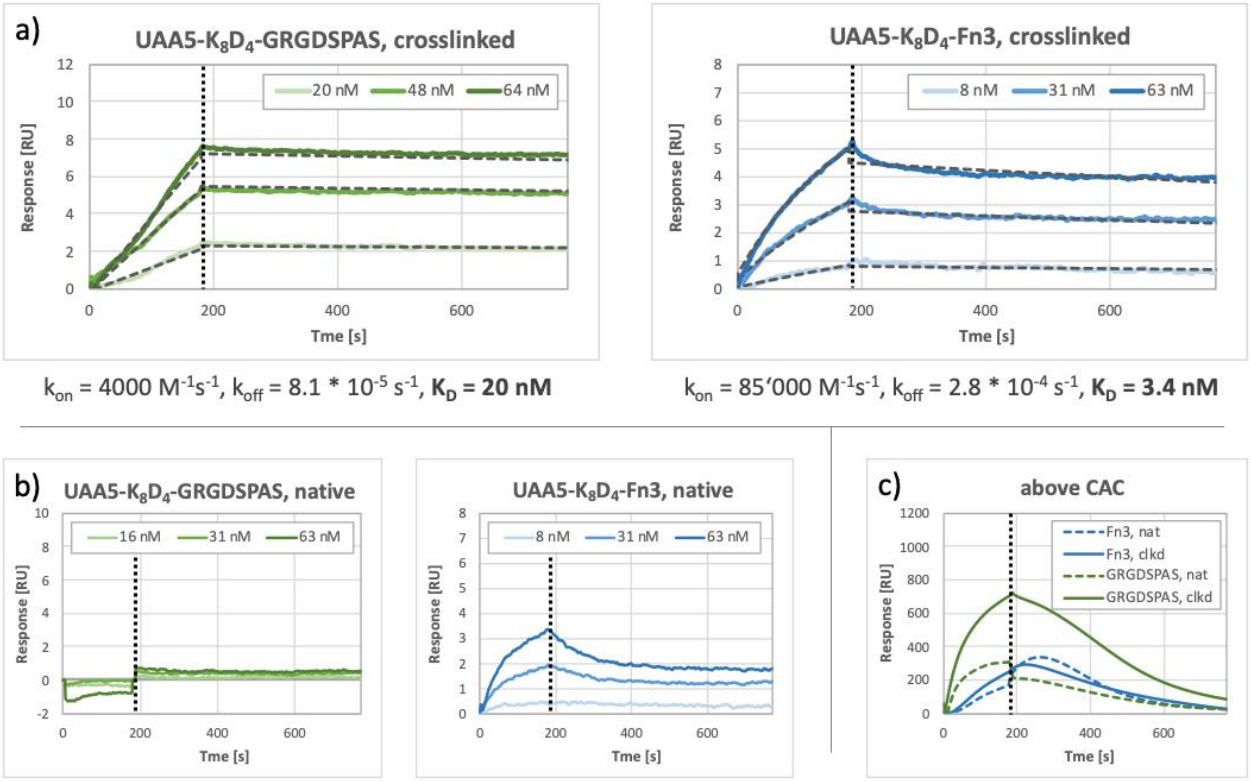

Figure 23: SPR analysis of the $\alpha_v\beta_3$ integrin binding of the UAA5-40 diblock constructs. **a)** In the crosslinked state, the Fn3- and GRGDSPAS-functionalized particles showed very high binding affinities to $\alpha_v\beta_3$ integrin. As a comparison: *Dzuricky et al.*'s native Fn3 constructs had a reported K_D of 79 nM[30]. **b)** In the native state, the GRGDSPAS construct showed no binding at concentrations below the CAC. For their native Fn3 analogues on the other hand, binding was observed though at lower levels than for the crosslinked nanoparticles. **c)** At concentrations above the CAC, native and crosslinked constructs showed comparable binding affinities to $\alpha_v\beta_3$ integrin. Note that the vertical dotted line represents the point at which the buffer is exchanged.

For the integrin-targeting constructs with the larger UAA4-80 basis, the SPR results were less clear: Whereas the SPR data for the crosslinked GRGDSPAS-functionalized particles showed very strong binding at a concentration of 190 nM, the signal rapidly collapsed upon further dilution (fig. 24a). For the crosslinked Fn3 constructs on the other hand the sensograms seemed somewhat decoupled from the concentration (fig. 24b). At 68 nM, the SPR data indicated strong binding whereas at concentrations both above and below that value, no binding was detected. As a result, we could only determine the K_D for the GRGDSPAS particles in the mid-nanomolar range which was calculated at 85 nM (fig. 24c). As neither of the two crosslinked particles showed any detectable binding upon dilution below the CAC, the multivalency benefits upon crosslinking could not be proven for either of these integrin-targeting constructs. This is most probably due to a combination of a comparably low binding affinity for the nanoparticles of this diblock architecture and the low CAC of these ELP/RLP constructs. As a result, the signal-to-noise ratio is not good enough to detect the integrin binding of these crosslinked nanoparticles in the sub-CAC regime.

DR5-Targeting

Initial characterization of the crosslinked Tn3 sample with the UAA5-40 basis in the sub-CAC regime yielded a K_D value deep in the picomolar range (fig. 25a). This extremely good binding constant can be mainly attributed to the k_{off} rate which is so low that it is most probably even

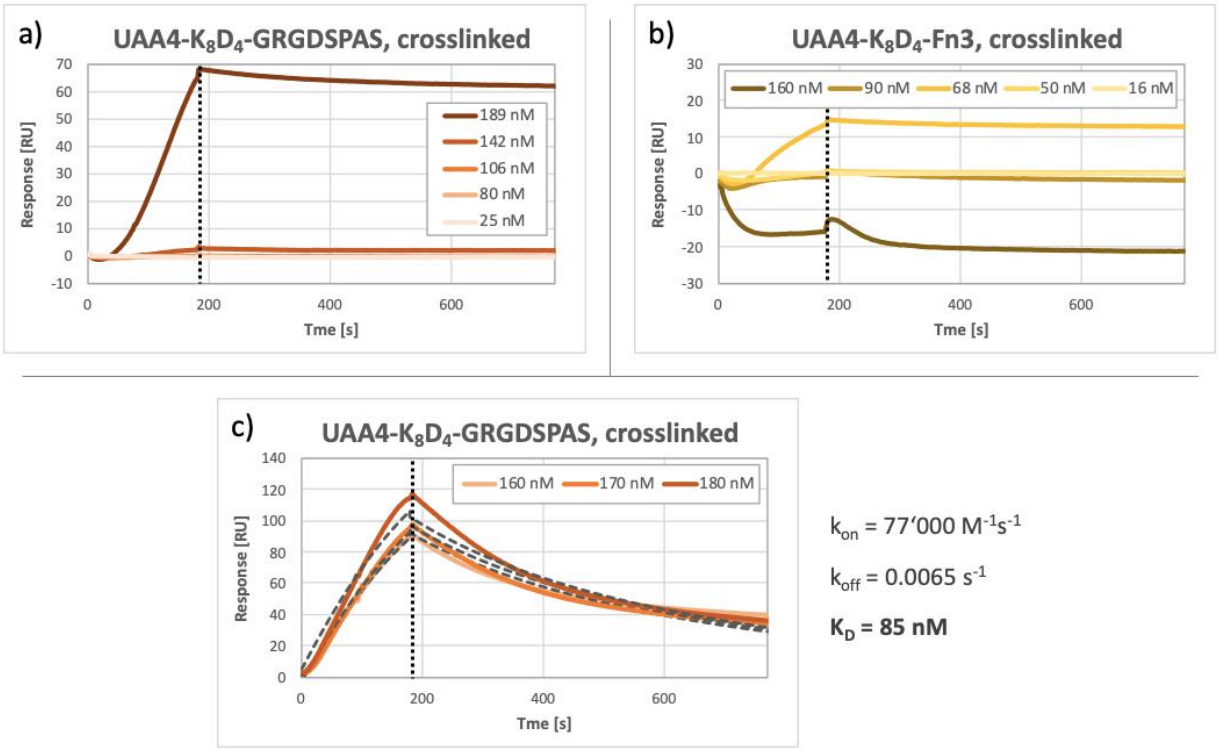

Figure 24: SPR characterization of the integrin-targeting UAA4-80 constructs. **a)** The GRGDSPAS-functionalized construct seemed to have a sharp cut-off for binding to $\alpha_v\beta_3$ integrin as the SPR signal rapidly collapsed upon dilution below 150 nM. **b)** For the Fn3-functionalized construct, the SPR data is even more confusing as it showed good binding at 68 nM but none at concentrations both above and below that value. **C)** Thus, the only K_D value that could be calculated was the one for the crosslinked GRGDSPAS construct in a narrow concentration range around 170 nM. Note that the vertical dotted line marks the point at which the buffer is exchanged.

below the limit of detection of the SPR instrument. As opposed to the integrin-targeting UAA5-40 particles, we however also observed very strong binding for the native Tn3 construct in the same concentration range (fig. 25b). With 250 nM, the calculated K_D value was only 12-fold increased compared to the crosslinked sample. This suggested that though crosslinking still improved DR5-binding, it did this only to a very limited degree.

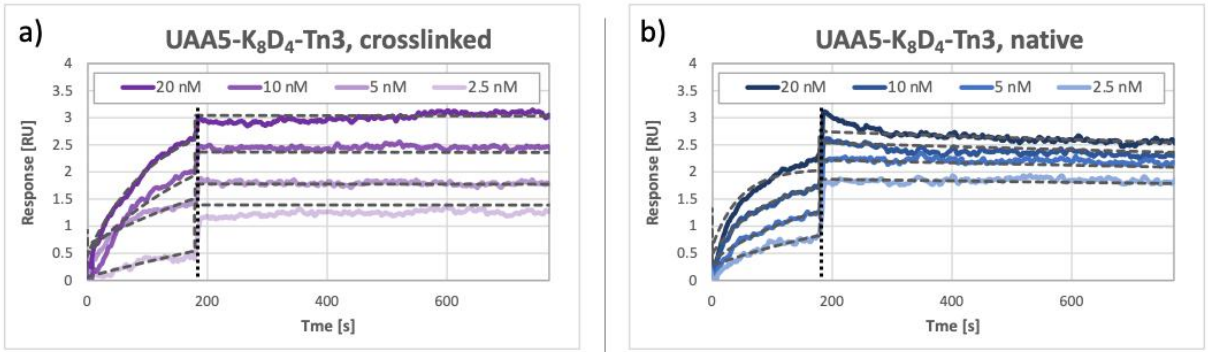

k_{on} = 440'000 $M^{-1}s^{-1}$, k_{off} = 9.3 * 10^{-6} s^{-1}, **K_D = 21 pM**

k_{on} = 1'070'000 $M^{-1}s^{-1}$, k_{off} = 2.7 * 10^{-4} s^{-1}, **K_D = 250 pM**

Figure 25: SPR characterization of the DR5-targeting UAA5-40 constructs. The comparison of the SPR data in figures **a** and **b** showed that the binding affinity of the Tn3-ligand seemed to only mildly benefit from multivalent display compared to the integrin-targeting constructs in figure 23. This then indicated that the requirement for multivalency for Tn3 action mainly stemmed from downstream effects after binding of the receptor and not from DR5-binding itself. Note that the vertical dotted line represents the point at which the buffer is exchanged during the SPR experiment.

Principally, this was not a too unexpected result since we already knew that apoptosis induction via DR5-binding required downstream trimerization of the ligand-bound DR5 receptors in the cell membrane[94,95]. Therefore, we had expected that the reported multivalency requirement for Tn3-action was at least partly stemming from this mechanistic effect rather than the DR5-binding itself. Nevertheless, we had still hoped to see a slightly more pronounced improvement in binding affinity upon crosslinking of our ELP/RLP nanoparticles.

In the face of these rather underwhelming improvements in binding affinity as well as the fact that the extremely tight binding of the Tn3 ligand led to problems in chip regeneration after each SPR cycle, we decided to abandon the SPR measurements at this point.

4. Conclusion and Outlook

In summary, the results of this study show very convincingly that the CAC is one of *the* limiting factors to efficient therapy with ligand-targeted, loosely self-assembled nanoparticle medicines. For therapeutic nanoparticle formulations to be the most effective, the potency and/or binding affinity of the displayed multivalent ligands needs to be matched by the CAC of the corresponding carrier system. If the CAC of the self-assembled nanoparticle lies significantly above the theoretical EC_{50} value of the respective multivalent ligand then the real EC_{50} value for the whole formulation will increase accordingly. Though this study has been exclusively performed on nanoparticles based on amphiphilic biopolymers, these conclusions are expected to apply analogously to other self-assembled nanomedicines such as liposomes, polymersomes or polymer micelles.

As the CACs of self-assembled nanoparticle carriers rarely go below the mid-nanomolar range but therapeutic ligands are often significantly more potent than that, we believe that this is a design flaw that has prevented many formulations from reaching their full potential. Moreover, the number of available nanoparticles steadily decreases after administration due to clearance or off-target uptake. As a result, it can be expected that nanoparticle formulations generally exceed their CAC only for a limited amount of time – if at all[115–117]. In this study, we show that chemical crosslinking of the nanoparticle carrier in its assembled state could become one of the key strategies in overcoming this major limitation. Whereas crosslinking did not significantly affect potency above the CAC of the native formulation, it greatly increased its effectiveness in the sub-CAC regime.

One of the limitations of the crosslinking strategy pursued in this study is that it is irreversible. This is great when it comes to ensuring multivalent ligand display by preventing particle disassembly but is less beneficial when the nanoparticle also carries cargo in its core that needs to be released. Though it can be expected that even such systems will eventually release their cargo once they are degraded in the lysosome, controlled release at a specific time or place – as it is often the goal for nanoparticle formulations – would be very difficult to achieve. A second limitation of crosslinking via photoactivation of *p*AzF is that this process is very non-specific and forms crosslinks in a very uncontrollable manner. Also here, this is not a huge issue for the constructs at hand but becomes problematic once the nanoparticle core also contains cargo. Since C-H or N-H insertions of the reactive nitrene of *p*AzF into the cargo molecule might irreversibly impair its intended function, this scenario should be avoided as best as possible. One approach in solving this issue could be to load the drug *after* crosslinking not *before*. It is however unclear whether the crosslinked particle would actually still allow for drug diffusion into its core at this stage. And if it did, this would most certainly be a rather inefficient and cumbersome way of drug loading.

Taking both the above-mentioned limitations together, it would be very beneficial to investigate alternative crosslinking strategies as the next step. In order to achieve reversible crosslinking, one could for instance take advantage of the redox-sensitive disulfide or pH-sensitive hydrazine chemistries as has been done many times before[118–120]. Another alternative to achieve selective crosslinking would be to use click chemistry methods. Though this would again result in irreversible crosslinking, click chemistry reactions are very reliable and highly selective and have

become the “go to”-option for conjugation reactions in biorthogonal research[121]. Regardless of which crosslinking strategy is chosen, it should preferentially work without any external reagents – or at least only biocompatible ones[63,64].

Another sensible next step would be to take the very promising DR5-targeting constructs of this study and move to *in vivo* experiments. While the primary goal should certainly consist in proving that the abovementioned CAC-vs-EC_{50} dilemma also holds *in vivo* such experiments might also provide some interesting secondary data. For instance, it seems very plausible that the pharmacokinetic profile of the crosslinked nanoparticles will be different from their native analogues due to their unique architecture.

Apart from the investigation of chemical crosslinking as a means to overcome the CAC barrier in self-assembled nanoparticles, the second goal of this study had been to analyze shape-dependent effects more closely. With the unfunctionalized UAA4-80 construct, we originally thought to have found a diblock architecture that forms strongly elongated particles and had been very curious to compare them with the spherical UAA5-40 particles. Sadly, the UAA4-80 constructs completely lost their worm-like shape upon functionalization which eliminated this branch of the study.

Nevertheless, shape has been proven to be a very important factor for the effectiveness of nanoparticle formulations. As a result, we believe it would still be worth revisiting this part of this study. According to the worm-vs-sphere diagram drawn by *Weitzhandler et al.* the UAA4-80 construct resides very close to the border to spherical morphologies[29]. Thus, it seems plausible that already a minor modification in the ELP/RLP diblock architecture – for instance a decrease in number of ELP repeats or the choice of a more hydrophobic ELP guest residue – will preserve the worm-like morphology even after functionalization. Moreover, these changes might also lead to the creation of crosslinked branched or even lamellar structures – morphologies that did not occur even for the unfunctionalized UAA4-80 construct. Structures like this would not only be highly interesting from a morphological point of view but could also lead to new applications in the area of hydrogel-based drug delivery.

Though the work with the *p*AzF-containing constructs was generally very easy and straight forward, one minor nuisance was that the yields were generally around 2-3 times lower than for analogous *p*AzF-free constructs. For experiments that do not require large amounts of protein – such as the ones of this study – this minor decrease in yield is still more than tolerable. Once we move *in vivo* things however might start looking slightly different. Thus, it seems also worthwhile to put some effort into solving this issue. Based on the observations that only an average of one *p*AzF residue per polypeptide chain is required for stable crosslinking and that at least the Tn3 nanoparticles also tolerate partial functionalization without significant decreases in potency, hybrid nanoparticles might be the solution. More concretely, these hybrid nanoparticles would consist of a small fraction of unfunctionalized constructs that carry several *p*AzF residues and a large fraction of *p*AzF-free constructs with the ligand(s) of interest. Like this, the more challenging ligand-bearing constructs could be expressed in regular protein production *E. coli* strains whereas only the shorter, less challenging *p*AzF-containing proteins would have to be expressed in an amber-suppressor strain. Furthermore, this approach would

also enable us to use unfunctionalized *p*AzF-containing diblock constructs as universal “glue” to crosslink a variety of different ligand-bearing constructs.

Project II

Optimizing Concatemerization to yield large ELP-encoding DNA Constructs within one Cloning Cycle

5. Project Introduction

With PRe-RDL, we possess a cloning strategy with which ELPs – or any repetitive biopolymer – can be easily constructed, grown and functionalized on the DNA level in a highly controlled manner[44]. Nevertheless, growing a large ELP construct with this strategy from scratch is a long and time-consuming process, as the ELP length is only doubled in every PRe-RDL cycle. If we for instance want to construct an ELP with 160 pentapeptide repeats starting from a commercially orderable oligonucleotide encoding for a 10-mer ELP, a total of five cloning steps (1x Gibson assembly, 4x PRe-RDL, fig. 26) is necessary. Even under optimal circumstances it would take at least 15 days to go through this entire process.

Thus, we felt the need to develop a new cloning strategy with which monoblock ELP constructs of a variety of different lengths could be constructed within only one single cloning step. In addition, this cloning strategy should still be compatible with PRe-RDL such that the resulting constructs can be easily functionalized in future cloning cycles.

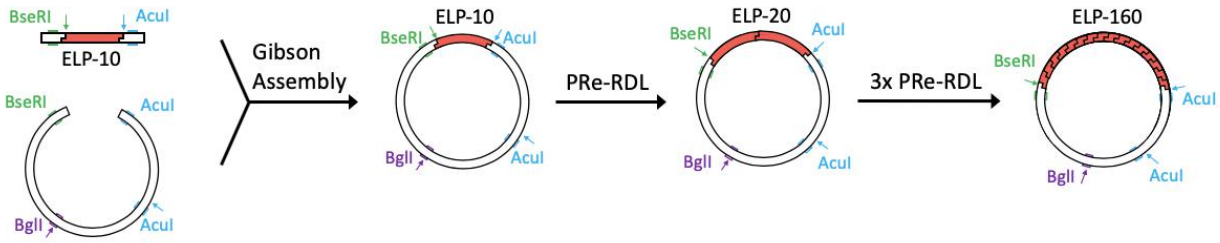

Figure 26: Illustration of the five necessary cloning steps to construct an ELP with 160 pentapeptides from scratch using PRe-RDL.

5.1 Previous Efforts

5.1.1 Concatemerization

One of the oldest techniques to construct repetitive DNA sequences is concatemerization[122–125]. In the first descriptions of this approach, the dsDNA monomer of interest was typically purified out of a bacterial plasmid by restriction enzymes. The enzymes were chosen such that the created dsDNA monomer had compatible sticky ends on either side. Like this, it was then able to polymerize (= concatemerization) into higher order constructs (= concatemers) once a DNA ligase was added to the reaction mixture. As the 5' and 3' ends of the resulting concatemers were however still compatible with the ones of the plasmid they were cut out of, they could easily be reintroduced by also adding the linearized plasmid to the concatemerization mixture. While this approach produced clones with a broad variety of concatemer lengths after bacterial transformation one could also introduce an additional gelpurification step to specifically select the concatemer of desired length prior to vector reinsertion.

In 1985, *Simpson et al.* published a study in which they had achieved up to 50-mers of a 172-bp monomer using this concatemerization strategy[123]. Three years later in 1988, *Kim et al.* used an identical approach to produce a 10-mer of the 1.2-kb gene *luxA* thus proving that the concatemerization strategy was not only limited to relatively short DNA fragments[124].

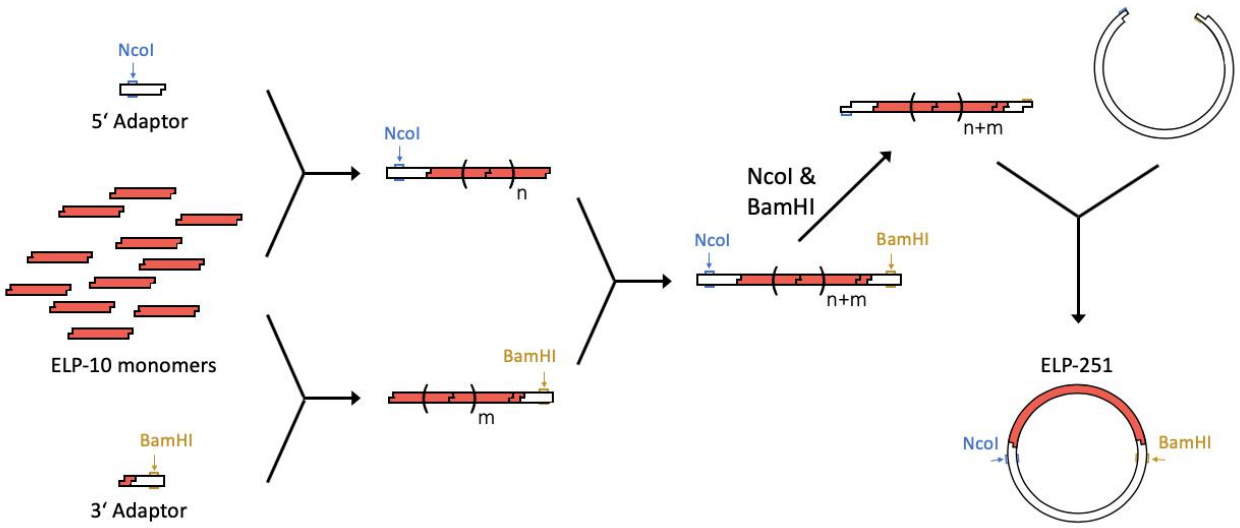

Figure 27: Schematic representation of the concatemerization approach employed by *McPherson et al.* to construct an ELP with up to 251 pentapeptide repeats in one single cloning step.[126]

As a result of these promising studies, the concatemerization approach was also investigated for its potential in growing ELP constructs[44,45,126,127]. In an initial study by *McPherson et al.* from 1996, a slightly adapted concatemerization strategy was then successfully employed to create an ELP concatemer with 251 pentapeptide repeats (fig. 27)[126]. A few years later, when *McDaniel et al.* then tried to integrate concatemerization into their PRe-RDL protocol, they however failed to create ELPs with more than 30 pentapeptide repeats[44]. Moreover, when *Amiram et al.* in 2011 used the same strategy and reaction conditions as *McPherson et al.* had 15 years earlier to concatemerize a ELP 10-mer into the Chilkoti group's PRe-RDL vector, they again failed to produce comparably large constructs[127]. It remains largely unclear why the two more recent studies had failed so spectacularly in replicating *McPherson et al.*'s concatemerization data, as the experimental setups were very similar in all cases. There were in principle only two differences: Firstly, the sticky ends on the DNA monomers were slightly different in length and composition. Secondly, the dsDNA monomers had been produced with slightly different methods. Whereas in the more recent studies the monomer had been produced by annealing two synthetic oligonucleotides, *McPherson et al.* had produced their monomer via polymerase chain reaction (PCR) followed by subsequent digestion.

5.1.2 Overlap Extension Rolling Circle Amplification

One reason, why these inconclusive concatemerization results were not further investigated is because the same study by *Amiram et al.* also reported the development of an alternative strategy for rapid ELP construction: Overlap extension rolling circle amplification (OERCA, fig. 28)[127]. OERCA is basically a combination of overlap extension PCR (OE-PCR) and rolling circle amplification (RCA) – two techniques which by themselves have already been used to create repetitive DNA sequences[128,129]. In principle, the experimental procedure for OERCA is almost identical to that of a regular PCR reaction. The only difference is that the used template is an enzymatically circularized, single-stranded version of the DNA monomer of interest[127]. In the first PCR cycle, construct elongation is exclusively achieved via RCA in which the DNA polymerase replicates several rotations of the circular template thereby creating ssDNA more

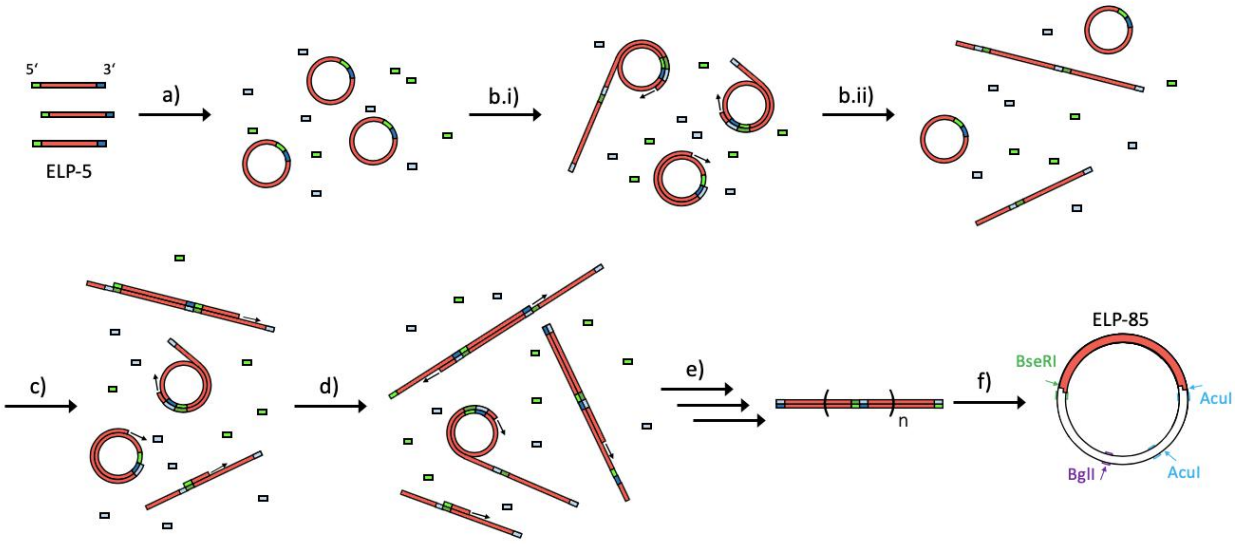

Figure 28: Step-by-step illustration of the OERCA process: First, a single-stranded ELP-5 construct is circularized (**a**) and subjected to RCA during the first PCR cycle (**b**). In the second PCR cycle, the complementary strands to the RCA products are generated (**c**) which can then be elongated through OE-PCR from the third PCR cycle onwards (**d**). After many additional cycles in which OE-PCR becomes more and more dominant long ELP concatemers are isolated (**e**) and ligated into the pET-24a+ vector for further modification through PRe-RDL.[127]

than one monomer in length. As the reaction progresses, OE-PCR comes more and more into play as more linear DNA is produced by RCA and regular PCR. As the created linear DNA strands have a highly repetitive sequence, they are able to anneal asymmetrically thereby acting as primers for additional DNA-polymerization at their 3' and 5' overhangs. Like this, the length of the DNA fragments is continuously increased during each PCR cycle. After 30 cycles and a subsequent DNA purification step, the OERCA mixture is then directly ligated into the linearized vector.

Using OERCA, *Amiram et al.* were able to create ELPs with up to 85 pentapeptide repeats in one single cloning cycle[127]. Nevertheless, only 2 of the 37 colonies they had screened contained ELP constructs with more than 50 pentapeptides and the average construct lengths actually lay at around 30 repeats. Thus, some significant improvements on OERCA are still necessary if it were to have a real edge on PRe-RDL.

5.2 Project Strategy

Based on these findings we found it justified to go back and give the concatemerization approach another shot. As opposed to the two abovementioned studies, we decided against the use of synthetic oligonucleotides as the starting material and instead chose PCR as our means for DNA amplification as had *McPherson et al.* for their successful ELP concatemerization study in 1996[126]. In order to provide a truly valuable addition to the toolkit of ELP cloning, we hoped to optimize concatemerization to a degree such that at least one out of ten resulting bacterial colonies would carry an ELP gene with 80 repeats or more.

The ELP monomer we chose for our concatemerization study was the same as *McPherson et al.*: $(VPGVG)_{10}$. As we planned to directly use the commercially orderable oligonucleotide as the template for PCR rather than the vector-bound version – thereby sparing us the Gibson assembly cloning cycle – the construct we designed already contained the recognition and

cleavage sites for the PRe-RDL restriction enzymes *AcuI* and *BseRI* as well as sites for T7 promotor and terminator primers (fig. 29a). As it seemed plausible that the restriction enzymes would have trouble binding properly if their recognition sites would be too close to the end of the dsDNA strand, we also included spacers between the ELP sequence and the T7 binding sites.

After digestion of the PCR product to yield the $(VPGVG)_{10}$ monomer, the concatemerization reaction itself should then proceed in a seeded manner. More concretely, the monomer shall first only be concatemerized with an empty "B" cut analogous to the ones employed in the PRe-RDL protocol (fig. 29b). By using the "B" cut as a seed for concatemerization we can ensure that one end of the formed concatemer is always available for additional $(VPGVG)_{10}$ monomers to bind without risking self-circularization. After a certain amount of time – a parameter that can be optimized to control the lengths of the created concatemers – the complementary "A" cut shall then be added to reconstruct the complete pET-24+ cloning vector for subsequent transformation.

In order to characterize the concatemer distribution over the yielded bacterial colonies, we planned on using colony PCR. Though constructs with repetitive sequences had been shown to sometimes yield heterogenous PCR products due to overlap extension, we were confident that the 50 bp additions on either side of the construct should be enough to prevent this from happening. Using colony PCR then had several advantages over the conventional diagnostic digests of overnight cultures such as its relative ease of use and its high-throughput nature.

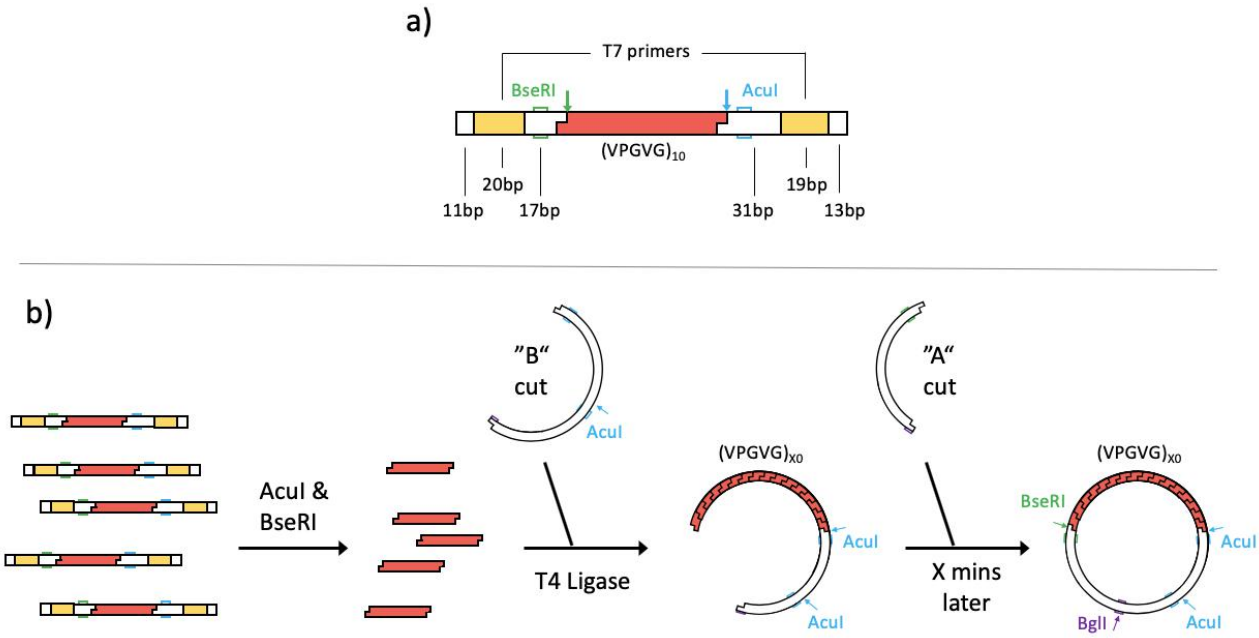

Figure 29: Overview of the project strategy pursued in this second project to employ concatemerization to arrive at high molecular weight ELP constructs in one cloning cycle: The starting point is the oligonucleotide construct in **a)** which contains recognition sites for T7 primers in close proximity to the ELP sequence. Thus, the oligonucleotide can be used as the template for PCR amplification. The PCR product is then digested with *AcuI* and *BseRI* to yield the dsDNA monomer for concatemerization (**b**). During concatemerization, the "A" cut of the empty vector is added with a slight delay such that the reaction is not quenched too early. After plasmid reconstruction and transformation, colony PCR is used to identify colonies with the desired number of ELP repeats.

6. Results and Discussion

6.1 Proof-of-Principle

In the first part of this study, we wanted to show that our concatemerization strategy principally worked in creating larger ELP constructs starting from the modified $(VPGVG)_{10}$ oligonucleotide from figure 29a. As we did not want to lose too much time, these first experiments were subject to only a very limited degree of optimization.

The first goal consisted in proving that PCR amplification of the $(VPGVG)_{10}$ oligonucleotide was successful in amplifying the targeted sequence without any major side products. For this, we chose a PCR program that consisted of 35 cycles with an annealing temperature at 45°C – a temperature which had previously worked very well for T7 primers. In the chosen setup, the final primer and nucleotide concentrations were at 2.5 and 250 µM respectively. The oligonucleotide starting material was supplemented at 0.25 ng/µL.

The resulting agarose gel after PCR amplification then showed rather disappointing results (fig. 30a). In addition to the targeted amplification product with a length of 237 bp, the gel also showed several unidentified side products both above and below the target band. From the band intensities on the agarose gel it seemed that the target construct was still the main product of the PCR amplification though only by a small margin. Though it seemed very plausible that this high degree of non-specific amplification might lead to some issues further downstream in the process, we nevertheless moved forward to *AcuI* and *BseRI* digestion. As a gel extraction step would be performed after digestion, we were confident that we would be able to remove the PCR side products before moving to concatemerization. Indeed, the agarose gel after *AcuI* and *BseRI* digestion looked as expected with the main band corresponding to the targeted length of 150 bp (sadly, no image was taken of this gel).

After subsequent gel extraction and ethanol precipitation we then performed a first concatemerization reaction with only the $(VPGVG)_{10}$ monomer. The reaction was performed over 1 hour

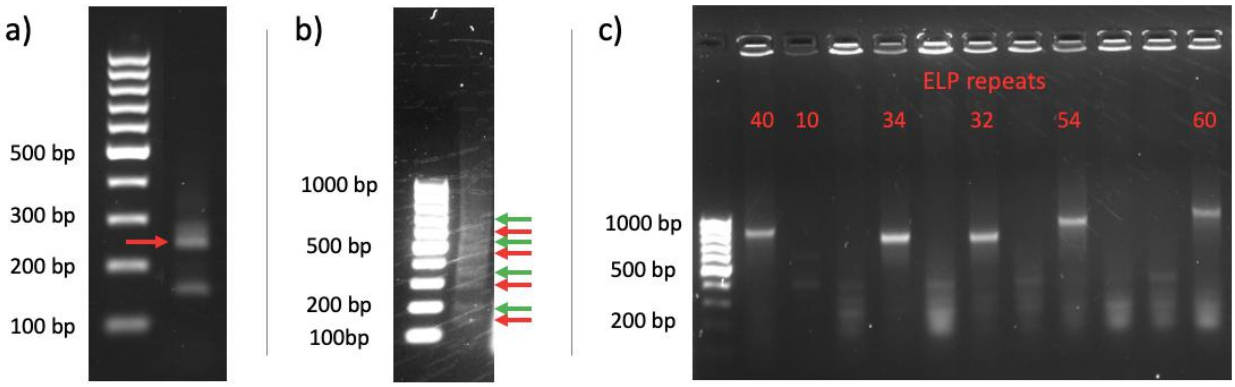

Figure 30: Proof-of-principle experiments: **a)** Gel electrophoresis after PCR amplification showed that though the most prominent band corresponded to the desired mass (237 bp, red arrow), several other side products were also co-amplified. **b)** Concatemerization of the digested PCR product over 1 hour resulted in two different ladder patterns: One corresponding to the desired construct (red arrows) and one with a relative shift of +30 bp (green arrows). **c)** Colony PCR after transformation showed successful ligation of the concatemers into the vector in around 50% of all colonies. Though sequencing confirmed seamless, in-frame vector insertions of up to 60 ELP repeats, some plasmids contained unexpected numbers of ELP repeats.

with monomer and T4 ligase (New England Biolabs, Ipswitch MA, USA) at final concentrations of 20 ng/µL and 20 U/µL respectively. The resulting agarose gel then showed the desired ladder pattern indicating concatemers with a length of up to 40 ELP repeats (fig 30b, red). In addition to these target-bands, the gel however also showed a second, similarly intense ladder pattern with a systematically increased mass by around 30 bp compared to the target concatemers (fig. 30b, green). Though the gel extraction step had obviously not been able to completely remove all side products, these results still confirmed positive concatemerization. Thus, we then moved on to an analogous concatemerization experiment supplemented with the "B" cut of the empty vector. 30 minutes into the reaction, the complimentary "A" cut was then added and another 30 minutes later, the ligation mixture was then transformed into competent *E. coli*. Analysis of the resulting colonies using colony PCR then showed that around one third of the screened colonies contained constructs with 30 or more ELP repeats with a 60-mer being the largest observed construct (fig. 30c). Though these were generally very encouraging results, the subsequently performed sequence analysis of the positive colonies then showed that some of the created constructs did not correspond to integer multiplications of the $(VPGVG)_{10}$ monomer. Half of the analyzed constructs were shown to contain smaller fragments of 2 or 4 ELP repeats in between the $(VPGVG)_{10}$ blocks. As the DNA encoding 2 ELP repeats has a length of 30 bp, this result generally matched the banding on the previous gel of fig. 30b.

Though this first set of experiments had generally yielded rather dirty concatemers with a relatively high fraction of side products, it had nonetheless been successful in proving the principle. Despite having been only weakly optimized, these preliminary experiments had already yielded constructs with more than double the length of what both *McDaniel et al*. and *Amiram et al*. had achieved using concatemerization[44,127]. Based on the gel images from fig. 30, it seemed very plausible that the side products could be easily eliminated by optimizing the conditions of the initial PCR amplification reaction. Furthermore, we were also very optimistic that some minor modifications to the concatemerization conditions could lead to constructs with even greater length.

6.2 Optimization

In order to improve the specificity and yield of the initial PCR amplification as well as to increase the length of the concatemerization products we screened through a variety of different variables that shall be discussed separately in the following sections. Unless specifically mentioned otherwise, one can assume identical reaction conditions as for the proof-of-principle experiments in the above section.

6.2.1 PCR Amplification

The variable which we generally expected to have the greatest effect on the cleanliness of the PCR reaction was the annealing temperature (T_a). As the self-priming for overlap extension – the hypothesized process by which the side products were formed – should theoretically have a different optimal T_a than the one for the binding of the T7 primers, changes in T_a might affect this equilibrium to our favor. To investigate this hypothesis, we ran PCR programs with six different annealing temperatures in a range of 41 to 61°C. The corresponding agarose gel then showed that though changes in T_a had an effect on PCR specificity they actually made it worse

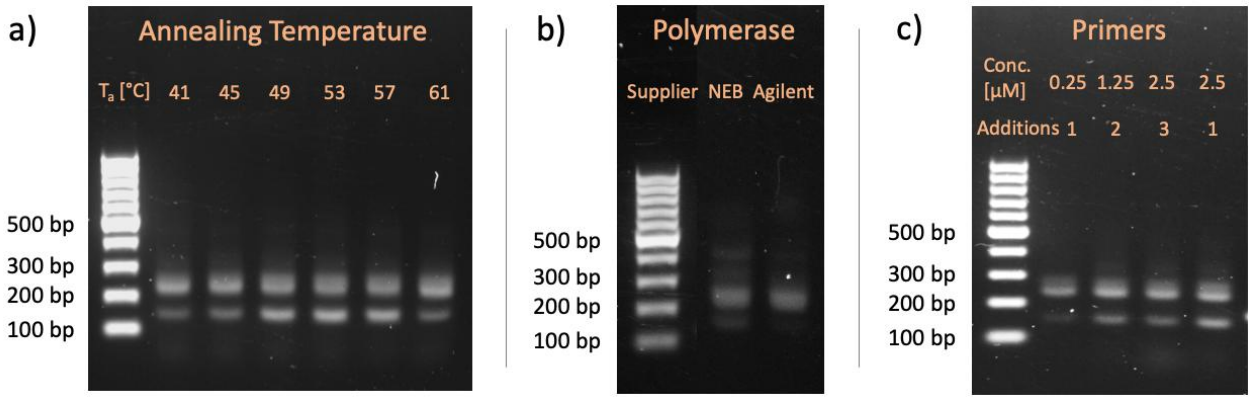

Figure 31: Agarose gels showing the results from the PCR optimization experiments: **a)** Changing the PCR annealing temperature away from the original value of 45°C resulted in equal or worse degrees of off-target amplification. **b)** Using a DNA polymerase from New England Biolabs instead of Agilent also did not improve purity but rather worsen it. **c)** Reducing the primer concentration did increase purity though it did not completely eliminate side product formation (lanes 1 vs. 4). Starting with 0.25 µM and then sequentially increasing the primer concentration via one (or two) primer additions after 15 (and 20) PCR cycles on the other hand did not increase purity. Note that for all three screenings, the targeted product had a length of 237 bp.

(fig. 31a). Of all the tested annealing temperatures, 45°C still seemed to yield the cleanest – or less dirty – PCR products and was therefore unchanged.

The second variable we changed was the DNA polymerase. In the initial experiments we had used Herculase II DNA polymerase supplied by Agilent Technologies (Santa Clara CA, USA). To test the effect different enzymes had on the specificity of the PCR reaction, we also included a Phusion® high-fidelity DNA polymerase supplied by New England Biolabs (Ipswitch MA, USA) at this stage. Also here, direct comparison at analogous reaction conditions then however showed that these changes actually made matters worse rather than better (fig. 31b).

Lastly, we also investigated different primer concentrations. The initial primer concentration had been chosen based on the length of the to-be-amplified construct to guarantee the highest possible DNA yields without any remaining primers or nucleotides after PCR completion. It generally seemed that the resulting large excess of primers particularly in the early PCR cycles might lead to higher chances of off-target priming and therefore the formation of side products. Thus, we ran several PCR experiments with decreased primer concentration as well as sequential primer addition. The resulting gels showed that a 10-fold decrease in primer concentration to 250 nM generally helped reducing side product formation though the resulting mixture was still not completely side product-free (fig. 31c). As the experiments with sequential primer addition on the other hand did not result in any improvements, the primer effect on PCR purity seems largely independent of the primer-to-template ratio.

Though reducing the primer concentration slightly improved the cleanliness of the PCR amplification, it still remained significantly contaminated. As a result of these rather underwhelming achievements, it seemed most likely that the sequence of the oligonucleotide starting material was the main problem. Admittedly, this construct had been designed rather hurriedly without checking for any potential risk factors for PCR amplification.

We were confident that by optimizing the sequences both up- and downstream of the ELP sequence we would have eventually been able to overcome these purity issues. As the screening

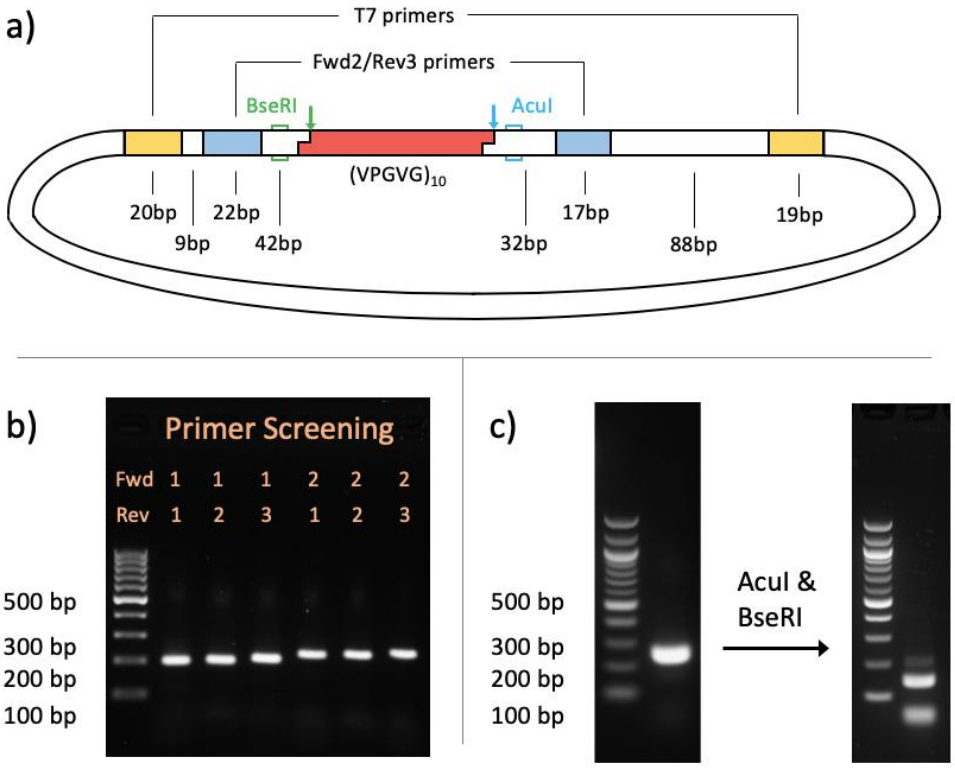

Figure 32: a) Due to the purity issues for the oligonucleotide we decided to switch to the vector-bound (VPGVG)$_{10}$ variant as the PCR template. As the T7 binding sites in this setup were relatively far away from the ELP sequence, we designed five new PCR primers in closer proximity. **b)** PCR amplification using all six primer pairs resulted in perfect purity in all cases. **c)** Enzymatic digestion of a PCR product that had been amplified with the fwd2/rev3 primer pair then resulted in the desired band corresponding to 150 bp. Note that broad band at around 60 bp corresponds to the 3' and 5' overhangs. The faint band at 210 bp corresponds to partly digested constructs.

through different oligonucleotide architectures would however have been a rather costly undertaking and we were also slowly running out of time, we decided to instead switch to the vector-bound (VPGVG)$_{10}$ construct as the template (fig. 32a). We chose this approach as it was already known that PCR amplifications of this particular sequence architecture yields clean products. If this strategy worked to yield large concatemers and we still had enough time, we then hoped to also test a linearized, shorter version of the same architecture as the PCR template which should principally work analogously as its vector-bound version.

One problem when using this sequence environment together with T7 primers is that the resulting fragments after enzymatic digestion of the PCR product would be rather similar in size – T7 primer binding sites are 73 and 137 up- and downstream of the 150 bp (VPGVG)$_{10}$ construct. Thus, achieving good separation for the subsequent gel extraction step might be challenging. To solve this issue, we designed five new primers – two up- and three downstream of the ELP sequence – with binding sites in closer proximity to the (VPGVG)$_{10}$ construct. PCR test reactions then showed that all six primer combinations yielded the target band in equal, perfect purity even at a primer concentration of 2.5 µM (fig. 32b).

Based on these findings, a large scale PCR amplification was then performed in which only the template (vector-bound instead of linear oligonucleotide) as well as the primer pair (fwd2/rev3 instead of T7 pro/ter) were changed compared to the initial setup. This yielded perfectly pure

bands both after PCR as well as after digestion with *AcuI* and *BseRI* (fig. 32c). After gel extraction and ethanol precipitation, we then moved on to optimize the concatemerization conditions.

6.2.2 Concatemerization Conditions

The first variable we screened for improved concatemerization results was the monomer concentration. Though it was generally expected that an increase in concentration would lead to better concatemerization, the resulting differences were hardly detectable on the corresponding gel (fig. 33a). As changes in monomer concentration also affect the brightness of the bands on the gel, it was very difficult to draw a definitive conclusion – but if there was any effect, it was very slim.

Secondly, we investigated the effect of reaction time. Here, the screening results indicated that longer ligation times certainly promoted higher order concatemerization though also only to a

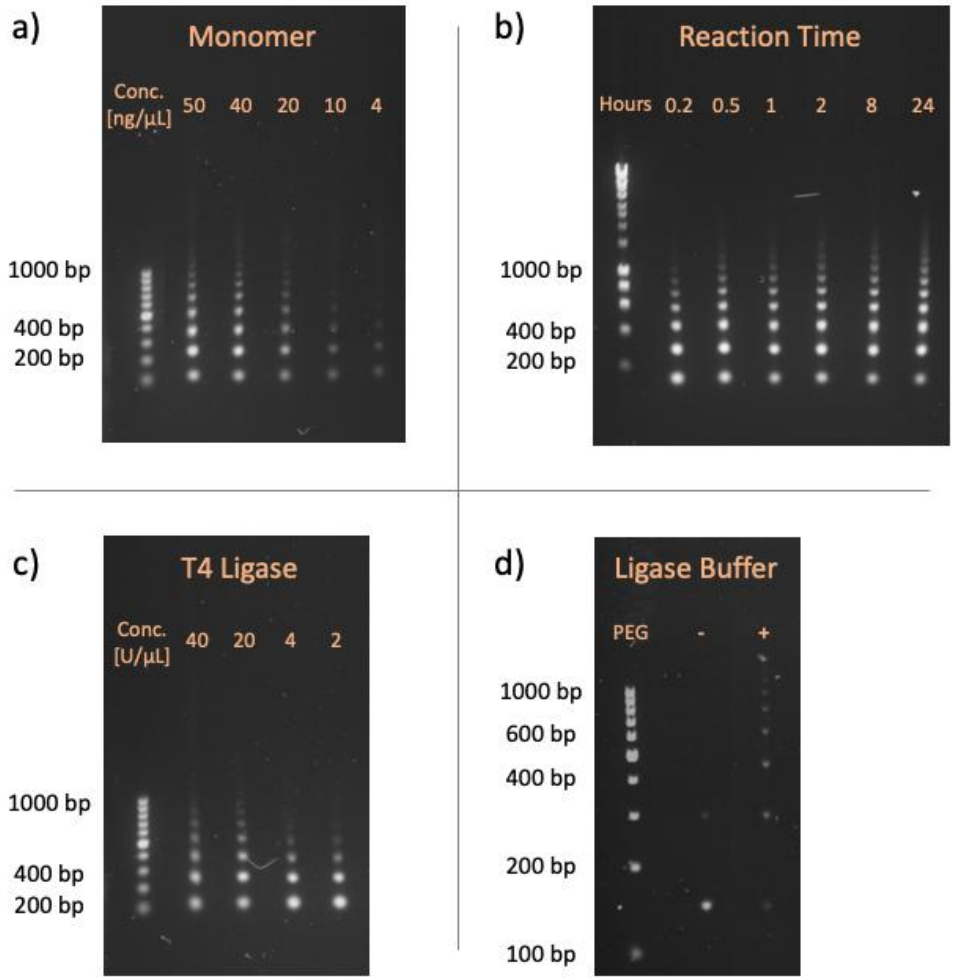

Figure 33: Agarose gels showing the results from the concatemerization optimization experiments: **a)** Due to decreasing intensity of the concatemer bands with decreasing monomer concentration it was difficult to draw a definitive conclusion on the effect of monomer concentration. If there was any, it was however rather slim. **b)** Increasing the reaction time did generally lead to more higher order concatemerization. The reaction was however generally rather fast with concatemers with 80 ELP repeats already being present only 10 minutes into the reaction. **c)** Increasing the ligase concentration seemed to be the most effective way to promote higher order concatemerization. **d)** By using ligase buffers containing the crowding agent PEG, we could significantly increase the concatemerization degree. Note that the monomer for this particular experiment originated from another batch due to which we have to interpret this gel separately

rather limited degree. Already after 10 minutes of ligation, we observed concatemers with up to 80 ELP repeats whereas six hours later, the highest band corresponded to only 30 additional ELP repeats (fig. 33b).

Our optimization experiments then also indicated that the ligase concentration seemed to have a more pronounced effect on the concatemerization degree compared to the two previously investigated variables. Decreasing the ligase concentration from 20 to 2 U/µL almost halved the size of the largest detectable concatemer on the agarose gel (fig. 33c).

Another approach to artificially increase the ligase concentration in the reaction mixture is by using reaction buffers that contain crowding agents such as polyethylene glycol (PEG). PEG in commercially available ligase buffers occupies significant fractions within the reaction volume thereby making it inaccessible to both ligase and DNA[130]. This then increases their effective concentration and ultimately the rate of the ligation reaction. Thus, we also included the PEG-containing Quick Ligase™ kit supplied by New England Biolabs (Ipswitch MA, USA) in our optimization efforts. The resulting experiments then showed that indeed, a change in ligase buffer dramatically increased the degree of concatemerization (fig. 33d).

Based on these findings the concatemerization conditions were changed such that the reaction was now run with 40 ng/µL of $(VPGVG)_{10}$ monomer and 1 µL of Quick Ligase™ per 6 µL of ligation mixture over the course of two hours. Under these conditions degrees of concatemerization were reached such that the individual bands of the ladder pattern were no longer visible on the corresponding gels.

6.3 Optimized Concatemerization

Based on these very encouraging results from the optimization stage, we were curious to see what the concatemer distribution would look like in the bacterial colonies after transformation. For this, we ran an analogous concatemerization experiment in presence of the “B” and after 1 hour also the “A” cut of the empty vector. After subsequent transformation, the corresponding plates then yielded countless colonies the next morning. To our great disappointment, both colony PCR as well as sequence analysis then however showed that all of these colonies exclusively contained empty vectors.

One possible explanation for this very unexpected result was that the reaction conditions might have been optimized too much such that all the starting material had already become inert – through circularization – before the “A” cut was added. Thus, we performed an analogous experiment in which both vector fragments were present from the very beginning. Nevertheless, we exclusively got empty vectors. In another attempt, we then replaced the two vector fragments by one linearized, dephosphorylated vector fragment which then however resulted in no colonies at all.

As it therefore seemed obvious that the $(VPGVG)_{10}$ monomers had great trouble ligating into the vector fragments, we then increased the monomer-to-vector ratio up to 1000-fold by decreasing the concentration of the vector fragments. However, also this attempt was unsuccessful.

Finally, we then exactly replicated the reaction conditions of the initial proof-of-principle study – even by using the oligonucleotide template for PCR – but still only got empty vectors.

The only exception to the general "empty vectors only"-rule that gave us some indication on what was going on were three false-positive results from different colony PCR screenings that seemed to correspond to ELPs with 20, 40 and 50 repeats. Subsequent sequence analysis then however showed that though their sequences were made up of 2, 4 and 5 $(VPGVG)_{10}$ blocks respectively, there was a frameshift mutation at each linkage (fig. 34). Judging from the sequence data, these frameshift mutations seemed to have stemmed from the loss of either one or even both of the two overhang nucleobases at the *AcuI/BseRI* cut site. Curiously, these two types of frameshift mutations were then also strictly alternating within the concatemer sequence. In other words: The sense-frame encoding the $(VPGVG)_{10}$ block always jumped back and forth between two reading frames but never touched the third one. As there were only eight inter-ELP linkages spread over these three false-positive clones, it still seems possible that this striking pattern might just have been a very unlikely coincidence. What the sequence data also showed is that of the six ELP-to-vector linkages, five of them were in-frame. This would then suggest that this type of linkage is generally significantly more sensitive to whatever caused these frameshifts than inter-ELP linkages. If this were true, it would also explain why we saw very good concatemerization for ELP-only reactions but only three out of hundreds of screened colonies actually contained a vector-bound concatemer.

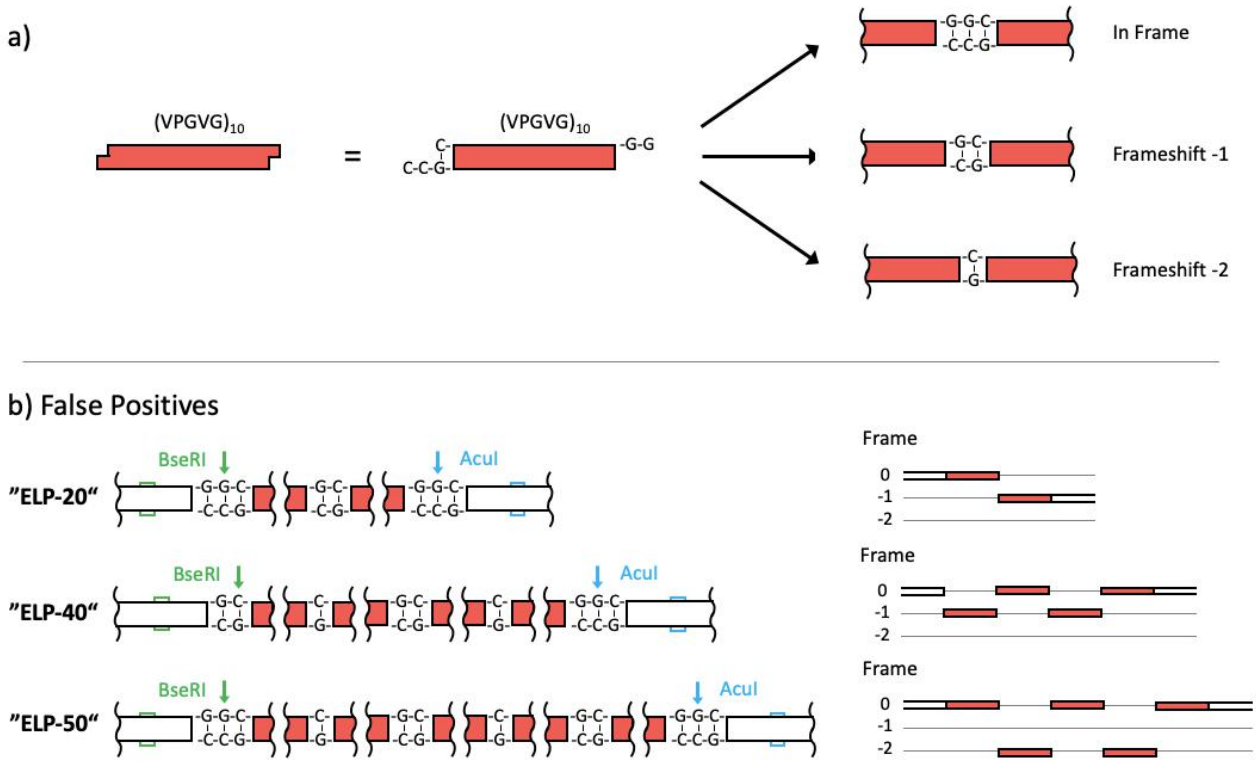

Figure 34: a) Schematic depiction of the three different types of monomer linkages observed for the three false positive colonies: in-frame ligations resulting in the glycine "scar" between two ELP blocks and the two observed frameshift mutations. **b)** Schematic illustration of the sequences of the three false positive colonies. Note that the two frameshift mutations were strictly alternating such that the sense-frame only ever occupied two of the possible three reading frames.

One of the possible explanations as to why these frameshifts occurred was that some nucleotides were added/removed within the non-coding regions during the PCR amplification step. To test this hypothesis, we performed sanger sequencing on the PCR product we had used for our concatemerization experiments. The sequencing results then showed us that everything was in order with the PCR amplified construct and that no relative shifts in restriction enzyme cut sites had occurred.

As issues during the PCR amplification could thus be ruled out as the cause for the observed frameshifts, there principally only remain two explanations which however both seem quite unlikely:

The first is that the restriction enzymes bound wrongly, thereby leading to shifts of the *AcuI* and *BseRI* cuts on either end of the ELP sequence. As the to-be-digested construct was rather short with the enzyme recognition sites relatively close to the end of the dsDNA strand, it seems plausible that this could have happened. This hypothesis however has one major weakness: None of the imaginable, shifted restriction enzyme cuts on the N-terminal end of the monomer would actually be complementary to any of the imaginable sticky ends on the C-terminal end while simultaneously upholding the observed frameshift pattern. Thus, it seems highly unlikely that such monomers would concatemerize as readily as had been observed in our experiments.

The second explanation is that the enzymatic cuts were made at the correct position but the sticky ends then degraded sometime between enzymatic digestion and concatemerization. Though this is the only explanation that would actually result in both complementary sticky ends as well as the observed frameshift pattern, the suggested instability of *AcuI* and *BseRI* cuts was so far never a problem for PRe-RDL vector fragments. In fact, the “A” and “B” cuts have been shown to be stable over years with complete retention of their ligation efficiency.

7. Conclusion and Outlook

To be honest, this second project has left us rather confused. The initial proof-of-principle experiments had resulted in very promising results already exceeding those of *McDaniel et al*. and *Amiram et al*. and made us believe we were at the brink of a great improvement on our cloning procedures[44,127]. The subsequently performed optimization then however seemed to have led to different, unidentified sticky ends on the $(VPGVG)_{10}$ monomers which allowed them to ligate with themselves but not with the vector fragments. As none of the possible explanations for this observation is particularly convincing, the only real solution is to head back to the drawing board and start over. If such a project would be attempted again, it might be worthwhile to also include some additional ELP monomers as perhaps the $(VPGVG)_{10}$ monomer sequence had just been an unfortunate choice.

Should these efforts then be successful and lead to reproducible results, the next big step would consist in developing a technique to precisely control the construct size within the bacterial colonies. Though colony PCR is an efficient and mostly reliable means in achieving rapid screening of many colonies for a targeted size, it still takes several hours to perform and analyze. Originally, we had thought to use different reaction times as a means to broadly control the distribution of concatemer lengths. Based on our findings depicted in fig. 33b, this no longer seems realistic. The generally most straightforward approach in controlling the size of to-be-transformed concatemers is to perform gel electrophoresis of the reaction mixture and to excise the band of the desired construct length. After gel purification, the insert is then ligated into the linear, dephosphorylated vector. Though this approach should principally also work in our case, it remains questionable whether we would retrieve sufficient amounts of DNA for the subsequent vector insertion. It might be necessary to also include an intermediate amplification step to ensure sufficient DNA quantities.

Once this second goal is also achieved, we would possess a very powerful and complimentary cloning strategy to PRe-RDL. Generally, PRe-RDL will certainly remain the method of choice to modify and grow ELP-based constructs. For projects that are at least partly based on the development and understanding of an entirely new class of biopolymers and thus have a large screening component, this concatemerization approach could be very valuable. Cloning is generally seen as a necessary evil which one does not want to lose a lot of time on. By using such a highly efficient and high-throughput concatemerization approach the time “wasted” could be reduced to a minimum. Another area which would be made more easily accessible through our concatemerization approach is the one of ultra-large ELPs with more than 200 pentapeptide repeats. To our knowledge, nobody has yet explored the physicochemical behavior of ELPs in that regime. By employing concatemerization, ultra-large constructs could be prepared quickly without losing to much time.

Project III

Developing ELP/RLP Multiblock Constructs that self-assemble into Vesicular Architectures

8. Project Introduction

Until today, research on ELP-/RLP-based drug delivery systems that benefit from the EPR effect has almost exclusively been limited to micellar platforms[13,30,35,42]. Whereas micelles are generally very easy and reliable in fabrication and also comparably predictable in terms of their behavior *in vitro* and *in vivo* there exist several limitations: For one, micellar drug delivery vehicles can typically only carry hydrophobic cargo in their cores. Delivering hydrophilic drugs such as cisplatin is a big challenge as these molecules generally destabilize the self-assembled particles thereby leading to insufficient shielding of the cargo from the environment and poor pharmacokinetics[131,132]. A second drawback is that the potential complexity of micellar drug delivery vehicles is rather limited. Micelles are usually very simple platforms with sensitivities to only one type of stimulus (e.g. temperature, pH, cell-receptors etc.). If one wanted to increase the specificity of the nanoformulation by engineering two or even three different sensitivities into the platform, micelles are a very difficult client. And lastly, micellar drug delivery systems are generally rather small in size with diameters rarely exceeding 100 nm. This then limits the amount of cargo that can be delivered per micelle.

In contrast to micelles, vesicular drug delivery systems are able to address all three of these limitations: Whereas hydrophobic drugs are still efficiently loaded and protected in the hydrophobic core of their amphiphilic membrane, their aqueous lumen can also carry vast quantities of hydrophilic cargo. In terms of complexity, vesicles can easily be engineered to be sensitive to multiple stimuli for instance by encapsulating micelles with a secondary sensitivity[133,134]. Like this, we can also build multi-step release cascades to further increase the overall specificity of the formulation. And lastly, vesicles are typically larger than micelles due to which we can also load significantly more cargo into the former. Meanwhile, vesicular drug delivery systems still benefit equally from the EPR effect and also show a similar pharmacokinetic profile[135,136].

Thus, vesicular drug delivery systems based on lipids (liposomes) and synthetic polymers (polymersomes) have been researched quite heavily during the last decades with some great results: In 1995, Doxil® – a liposomal formulation carrying doxorubicin – was the first ever EPR-benefiting formulation to be approved by the FDA[137]. Since then many more liposomal drug delivery systems have entered the market and countless polymersomal systems are currently in development for clinical application[12,138].

For ELP-based drug delivery, research into vesicular systems has so far been very limited with only a handful of studies that investigated vesicles mainly from an architectural standpoint. One of them was published in 2012 by *Martin et al.* in which AB and ABA block copolymers were employed to form vesicles with a diameter of around 200 nm[139]. The hydrophilic block contained repeats of the ELP pentapeptide VPG[4V:E]G whereas the hydrophobic block consisted of VPAVG-repeats. The latter is a slightly modified ELP block that has been shown to have a hysteretic phase behavior[140,141]. In another study on ELP-based vesicles, *Luo et al.* in 2015 reported the formation of monodisperse vesicles with a diameter of 100 nm using a VPGFG block attached to a collagen-like polypeptide (CLP) with the sequence $(GPO)_4$GFO-GER-$(GPO)_4$GG[142]. These vesicles were furthermore thermosensitive and disassembled upon heating above the melting temperature of the triple helices formed by the CLP-blocks.

8.1 Project Strategy

In the face of the rather sparse literature found on ELP-based vesicles, we felt the need to investigate some of our own constructs in the context of vesicle formation. More concretely, we pursued two different approaches that were investigated sequentially and will thus be discussed separately in the following sections.

8.1.1 ELP/RLP Triblocks

As we already had a relatively deep understanding of what variables controlled the self-assembly of ELP/RLP block copolymers, it seemed reasonable to start our investigation into vesicle-forming constructs by modifying the DB-40 and DB-80 constructs described in the first subproject of this master thesis. It is generally known that by continuing to apply changes to a construct's architecture that promote worm-like over spherical morphologies one might eventually create vesicular structures[143]. And as the DB-80 construct had already been shown to form strongly elongated worms and even lamellar structures under certain conditions, vesicular morphologies seemed within reach. Moreover, one of the two ELP vesicles reported by *Martin et al*. had consisted of a triblock construct in which the collapsed middle block was surrounded by solvated, hydrophilic ELP blocks[139]. Thus, the conversion into triblocks seemed like a promising strategy to morph the DB-40 and DB-80 constructs into vesicle-forming biopolymers. As a result, we then attached another $ELP_{A/G,80}$ block to the N-terminus to create the triblock constructs TB-40 and TB-80 (fig. 35a).

8.1.2 Charge-bearing Coronas

The second group of constructs that were investigated were designed on the hypothesis that charges in the coronal portions of amphiphilic molecules seemed to play an important role in vesicle formation. Highly charged coronas seemed to be a common denominator for many vesicle-forming molecules: From the highly polar headgroups of the lipids in liposomes over polyglutamic acid blocks in many synthetic polymersomes to the coronal glutamate-bearing ELP blocks employed by *Martin et al*[12,139,144,145]. In another study by *Bellomo et al.* from 2004, a highly charged polylysine block was fused to a hydrophobic polyleucine block to form a vesicular architecture[146]. Moreover, by introducing some lysine residues into the hydrophobic block, they were able to engineer pH-sensitivity into their vesicles.

An overview of the resulting charge-bearing constructs that we designed is shown in fig 35b. The relative lengths of the blocks within the constructs were adapted from the di- and triblock architectures employed by *Martin et al.* to yield vesicles[139]. In addition to vesicle formation we also hypothesized that these constructs could be subject so some interesting pH-dependent rearrangements. As had been previously reported by *Weitzhandler et al.* in their architectural study on ELP/RLP diblock constructs, the polarity of the coronal block has a strong influence on the particle morphology (fig. 6b)[29]. Furthermore, *Urry et al.*'s hydrophobicity index for guest residues in ELPs shows that the loss of the charge in glutamate and histidine residues dramatically decreases their polarity and thereby also the T_t of the respective ELPs[17]. Thus, we were confident that even if these constructs would nevertheless assemble into micelles we would still observe some interesting pH-dependent effects. More concretely, we hypothesized that upon decreasing/increasing the pH below/above the pK_a of the charged guest residues in the coronal

blocks, the changes in polarity could lead to a transition from spherical to worm-like architectures. Based on this secondary goal, we then designed our charged coronal blocks such that they for one spanned a significant pK_a-range and secondly would still remain soluble at room temperature even after losing their charge. Thankfully, scientists around Prof. Dan Urry and Prof. Ashutosh Chilkoti had already published several studies on pH-sensitivity in ELP constructs which supplied us with inspiration to design coronal blocks that met both of those requirements[41,147,148].

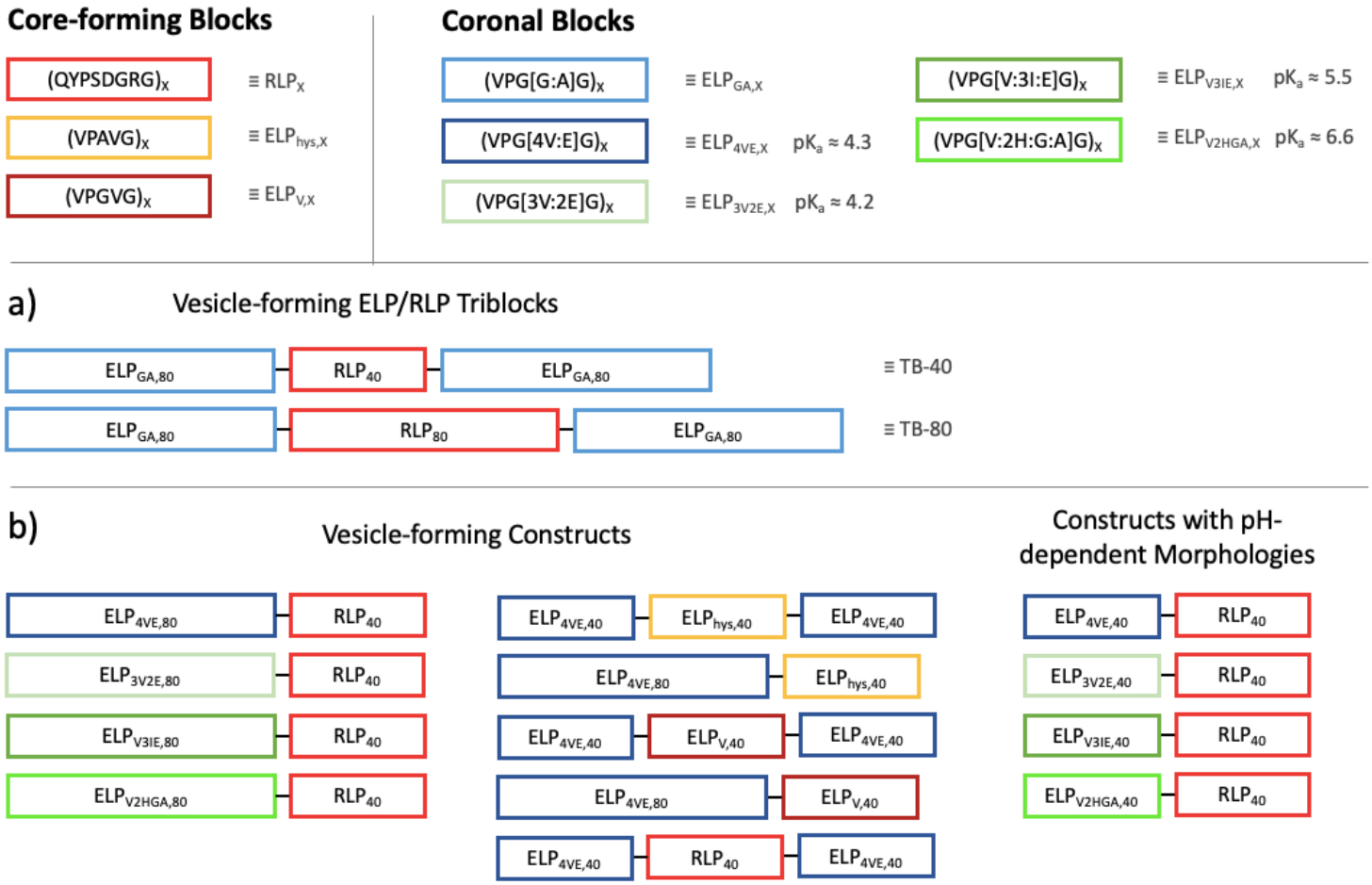

Figure 35: Schematic overview of the different constructs investigated in the third project of this master thesis.

9. Results and Discussion

9.1 ELP/RLP Triblocks

The initial characterization of the two ELP/RLP triblock constructs was performed by acquiring DLS data of the respective solutions in PBS (fig. 36a). Judging from the comparably small hydrodynamic radii, it already seemed highly unlikely that either of the two constructs had formed vesicles. Furthermore, the R_H value for the TB-40 construct suggested that for this polypeptide there might not actually have been any self-assembly at all. This indication was then however disproven by the subsequently taken cryo-TEM images. They showed assembled particles of a similar size for both triblock constructs (fig. 36b-c). Though the measured cores for TB-40 seemed slightly smaller than for TB-80, the TEM images for both constructs generally matched the DLS data for the latter and not the former – again, we assumed an invisible ELP corona with a diameter of around 15-20 nm (fig. 36a). At this point, it was largely unclear why the DLS measurements differed so greatly between these two constructs. In any case, the TEM images also supported the interpretation that these constructs did indeed form micelles and not vesicles. This, as the 2D-projections of vesicles in cryo-TEM images typically look more like rings than filled circles[142]. This deduction however needs to be treated with caution as such an effect might also have been covered up by poor contrast and resolution. Sadly, our static light scattering (SLS) instrument was unavailable at the time which would have provided a more reliable base to conclude whether the observed particles were actually vesicles or not.

As a result of this initial characterization, this subproject was basically already dead before it even started walking. Routinely recorded turbidity-vs-temperature datasets then however uncovered an interesting property of both triblock constructs: Their phase transition was irreversible (fig. 37a). As none of the previously characterized diblock constructs made up from the same ELP and RLP blocks had shown such an irreversibility, it seemed plausible that this was a consequence of the triblock architecture. To further investigate the mechanism of this irreversibility, solutions of the AlexaFluor-350 labeled triblocks were entrapped in microfluidic water-in-oil microcompartments. The created emulsion was then analyzed with a fluorescence microscope that had been equipped with a heating stage. When ELPs with a completely reversible phase transition were analyzed in that way one usually observed the formation of one single, phase-separated droplet which rapidly and completely disappeared upon cooling below the transition temperature[149]. In the case of our two triblock constructs, heating above their transition temperature however resulted in aggregates consisting of many smaller droplets (fig. 37b-c).

a)

Construct	DLS R_H [nm]	TEM R_H [nm]
TB-40	6.6 ± 0.2	9.3 ± 2.9
TB-80	27.3 ± 0.5	11.8 ± 3.4

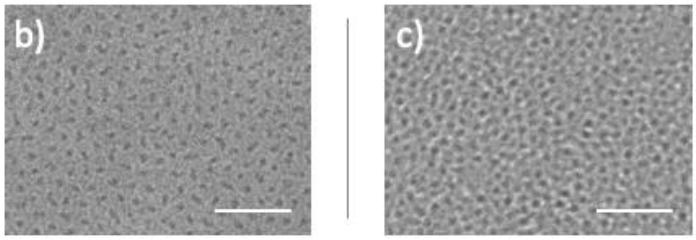

Figure 36: Initial characterization of the TB-40 and TB-80 constructs using DLS (**a**) and cryo-TEM (**a-c**). Note that the samples were both prepared in PBS at concentrations of 1 mg/mL. The scale bars on the TEM images both represent 200 nm.

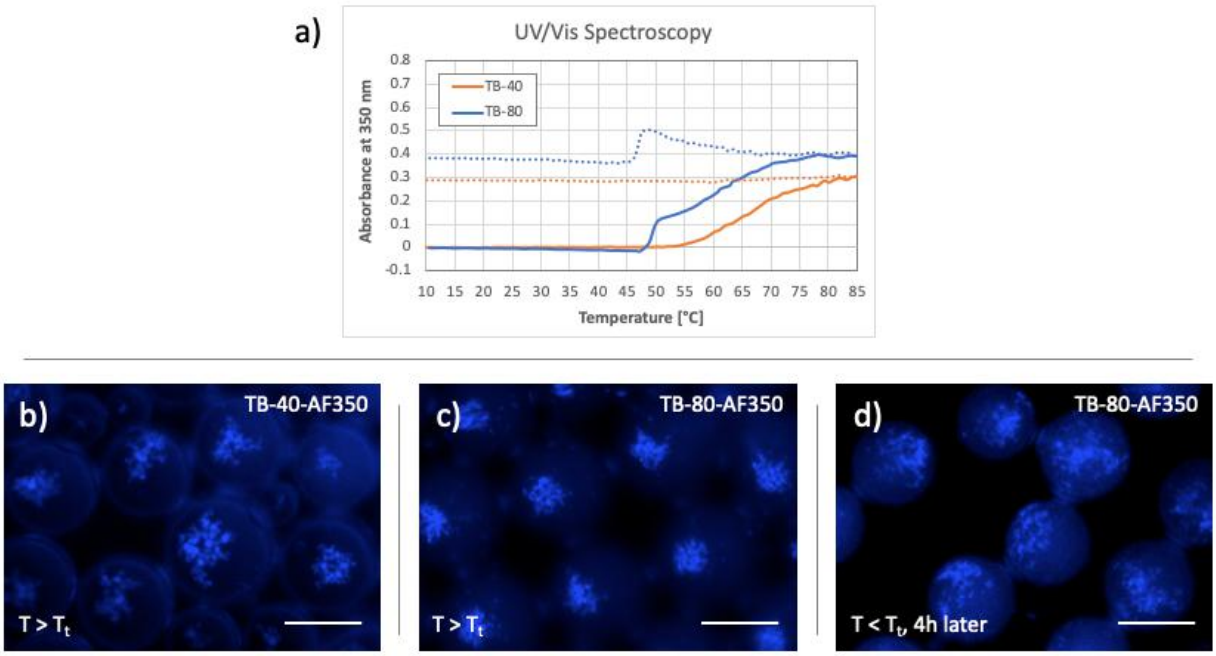

Figure 37: The secondary characterization of the TB-40 and TB-80 constructs showed a non-standard phase transition forming clusters of arrested droplets (**b-c**) with a remarkable irreversibility (**a, d**). The temperature-vs-turbidity analysis was performed at concentrations of 0.5 mg/mL in PBS and the water-in-oil compartments in the microscopy images all contain sample solutions at 2 mg/mL in PBS. Note that in the temperature-vs-turbidity diagram, the sample was first heated (full lines) and then cooled (dotted lines). All scale bars in the microscopy images represent 50 μm.

Moreover, these aggregates remained stable not only upon cooling below their transition temperature but also after storage at 20°C over several hours (fig. 37d).

As it seemed plausible that the number of nucleation sites created after surpassing T_t was the determining factor for the number of droplets in the resulting aggregate, further characterization experiments with different salt concentrations and heating rates were performed on the TB-80 construct. These experiments then showed that indeed, the heating rate does have a significant influence on the number of created droplets. The slower the temperature approached and surpassed T_t, the fewer phase-separated droplets were formed (fig. 38a). Moreover, if the temperature was rapidly decreased upon detection of the first nuclei, the aggregates disappeared again. This indicated that there was a "tipping point" somewhere in the middle of the phase transition process after which it became irreversible. The experiments with different salt concentrations on the other hand showed the expected decrease in transition temperature upon increase of the ionic strength of the buffer (fig. 38b).

In addition, these experiments also uncovered a rather unexpected dependence of the phase transition on the imaging process itself: For one, it was found that if the water-in-oil emulsion was heated without being simultaneously imaged the sample's phase transition occurred at temperatures around 8°C below the T_t observed for simultaneously imaged samples (fig. 38b). This then resulted in the observation of both transitioned and untransitioned microcompartments at the boundary of the field of view for experiments with simultaneous imaging (fig. 38c). Conversely, if the emulsion was imaged only slightly above the transition temperature of the ELPs upon the onset of nucleation and the temperature was then rapidly decreased, the microcompartements in the field of view generally remained phase transitioned whereas the samples in

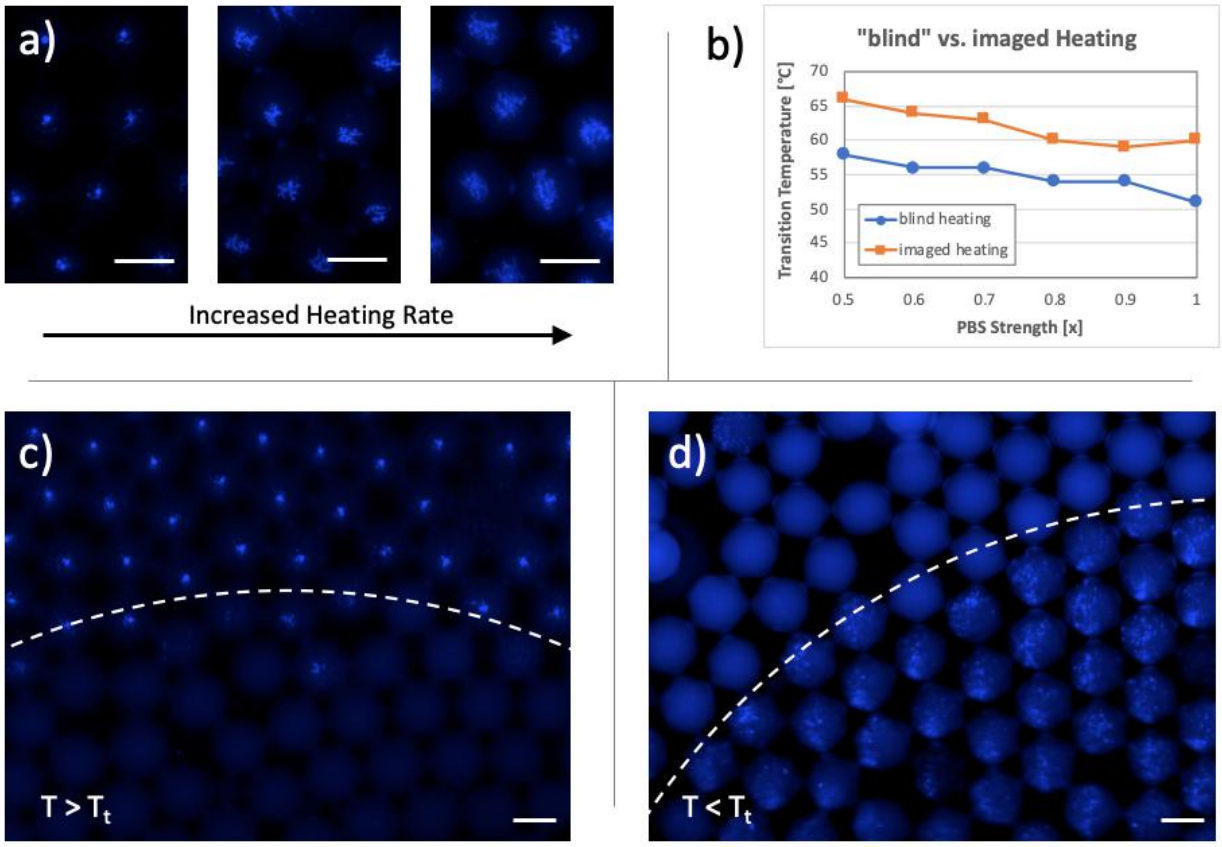

Figure 38: a) Water-in-oil emulsion experiments investigating different heating rates showed that the number of ELP droplets formed during the phase transition is dependent on the heating rate: Fast phase transitions yielded more droplets than if the transition temperature was passed very slowly. **b)** Secondly, an increasing PBS strength generally lowered the transition point as would be expected. In addition, we also uncovered some imaging-dependent effects such as a decrease in transition temperature upon "blind" heating – that is heating without simultaneous imaging – and different phase behaviors at the boundary of the field of view. In images **c** and **d**, the field of view in which imaging had taken place during the heating process is indicated with the dotted line. Note that all these analyses were performed on the TB-80 construct at 1 mg/mL in PBS and that all scale bars represent 50 μm.

the periphery returned to their soluble state (fig. 38d). These observations then brought us to the conclusion that illumination of the microcompartments generally seemed to stabilize them in whatever state they are in at the time. The mechanism of this phenomenon however remained unclear.

As these illumination-dependent findings were quite inexplicable but generally indicated a contribution of the used fluorescence tag we decided to re-express, -purify and -tag both triblock constructs and to use an AlexaFluor-488 tag instead. Subsequently, analogous characterization experiments were run which resulted in contradictive results: As opposed to the previously characterized samples, the triblocks of this second batch now seemed to have mostly reversible phase transitions (fig. 39a). In the case of the TB-80 construct, we also observed the formation of the perfectly spherical droplets that are typically observed for standard ELP phase transitions. Moreover, the observed phase transitions now were completely independent of whether the microcompartments were simultaneously imaged or not. Though the second batch was generally purer than the first one, it remains unclear why the two sets of triblock constructs would behave so dramatically different (fig. 39b).

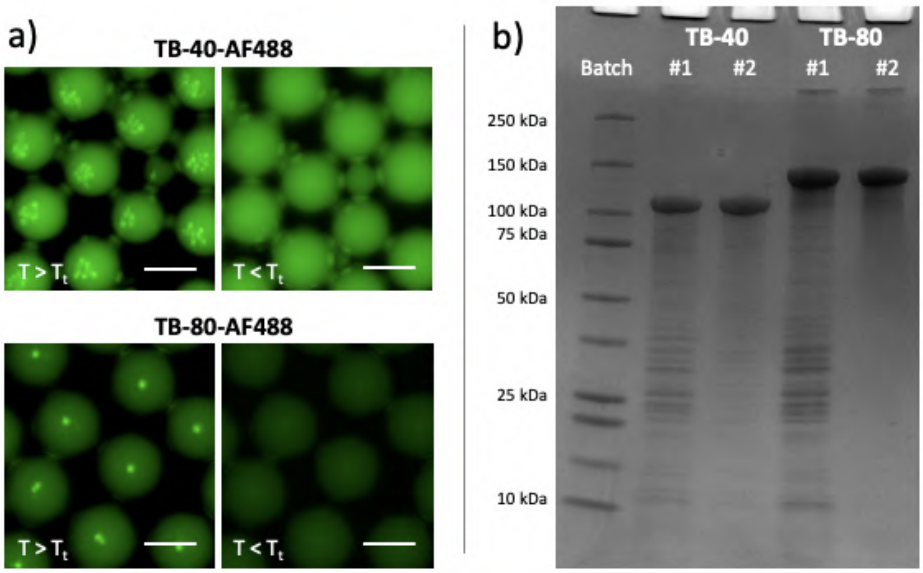

Figure 39: Re-expression and -purification of both TB-40 and TB-80 constructs and tagging with AF488 yielded an entirely different phase behavior: The phase transitions were now typically completely reversible (**a**) and also resulted in perfectly spherical aggregates in the case of the TB-80 construct. **b**) SDS-PAGE analysis showed that the second batch of protein was purer which might have been the reason for the observed differences between the two samples. Note that the scale bars represent 50 μm.

In the face of these rather inexplicable and often also inconsistent observations, we decided to abandon the ELP/RLP triblock constructs and move on to the second strategy for vesicle formation.

9.2 Charge-bearing Coronas

In order to determine the self-assembling behavior as well as the pH-dependence of the proteins of this second strategy, solutions at five different pH values (3.3, 4.3, 5.4, 6.6 and 7.4) were prepared and analyzed using both DLS and temperature-vs-turbidity experiments. The findings of this initial characterization are summarized in fig. 40a.

In terms of vesicle formation, most of the samples again seem to have formed primarily micellar particles with hydrodynamic radii rarely exceeding 35 nm. Apart from the two reference constructs taken from *Martin et al.* the only two other constructs that might have formed vesicles judging from their size readings are $ELP_{V3IE,40}$-RLP_{40} and $ELP_{V3IE,80}$-RLP_{40}. Though these constructs both predominantly formed small micelles at low pH, a considerably large secondary population (> 30 mass%) of particles several hundred nanometers in size was observed at higher pH. To further characterize the particle morphology, cryo-TEM images were recorded for the $ELP_{V3IE,80}$-RLP_{40} construct (fig. 40b). These images then showed an equal mixture of micelles and short worm-like structures but nothing in the size-range reported by DLS. Based on these findings, two interpretations are possible: The first explanation was that the DLS instrument had systematically overinterpreted the prevalence of the secondary population. The alternative hypothesis was that these larger particles rearranged during the sample preparation for cryo-TEM and were thus no longer present in the corresponding images.

In terms of the hypothesized pH-dependent rearrangements for the charge-bearing ELP/RLP diblock constructs, the DLS results were very discouraging: For all constructs and at all investigated pH values, the primary population had corresponded to small micelles which then directly phase separated above the transition point of the respective constructs. Though the different constructs showed the expected trends regarding their transition temperature for decreasing/increasing pH, the lost charges within the coronal block did not have any significant effect on the particle morphology. One possible explanation for this is that though the charges were lost, the coronal blocks were still not hydrophobic enough to create worm-like morphologies. Based on the hydrophobicity scale developed by *Urry et al.* this however seems highly unlikely as the uncharged glutamate and histidine residues respectively rank equally and significantly higher in terms of their hydrophobicity in comparison to valine[17]. Another explanation is that RLP_{40} was a poor choice as the core-forming block as it generally promotes micellar morphologies in comparison to longer RLP blocks.

a)

Construct	T_t at pH 3.3 [°C]	T_t at pH 7.4 [°C]	Est. pH for T_t at 37°C	R_H of P1 [nm]	R_H of P2[nm]	Comment
$ELP_{4VE,40}$-RLP_{40}	14	64	5.2	32	140	P2 only at pH 7.4
$ELP_{4VE,80}$-RLP_{40}	16	56	5.0	33	200	No stable readings
$ELP_{3V2E,40}$-RLP_{40}	11	56	4.8	29	400	No stable readings
$ELP_{3V2E,80}$-RLP_{40}	15	60	4.5	35-80	-	For increasing pH, P1 radii increase
$ELP_{V3IE,40}$-RLP_{40}	9	33	8-9	28	500-800	P2 in considerable mass fraction at higher pH
$ELP_{V3IE,80}$-RLP_{40}	10	54	5.6	30	300-400	P2 in considerable mass fraction at higher pH
$ELP_{V2HGA,40}$-RLP_{40}	>80	14	5.3	25	150	P2 appears at pH 6.6 above T_t
$ELP_{V2HGA,80}$-RLP_{40}	>80	21	6.2	27	44	P2 appears at pH 6.6 above T_t
$ELP_{4VE,80}$-$ELP_{hys,40}$	31	72	4.4	150-260	20	For increasing pH, P1 radii increase
$ELP_{4VE,40}$-$ELP_{hys,40}$-$ELP_{4VE,40}$	31	66	4.4	170-250		P1 stable above T_t
$ELP_{4VE,80}$-$ELP_{V,40}$	>80	26	N.A.	6	60	No pH-vs-R_H-trend. No stable readings
$ELP_{4VE,40}$-$ELP_{V,40}$-$ELP_{4VE,40}$	>80	60	N.A.	90-200		No pH-vs-R_H-trend. No stable readings
$ELP_{4VE,40}$-RLP_{40}-$ELP_{4VE,40}$	>80	60	N.A.	90-200	20	No pH-vs-R_H-trend. No stable readings

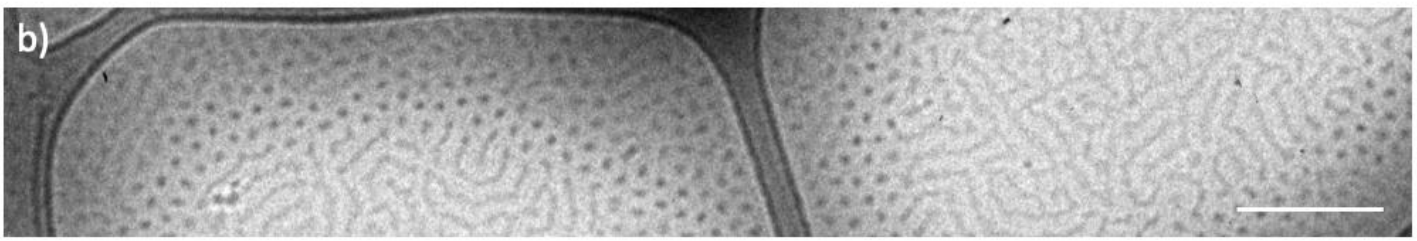

Figure 40: a) Overview of the initial DLS and UV/Vis characterization for the constructs with charge-bearing coronal blocks. All constructs were analyzed at a concentration of 1 mg/mL and at five different pH values: 3.3, 4.3, 5.4, 6.6 and 7.4. For the DLS data, measurements every 3°C were performed between 4 and 60°C. **b)** Cryo-TEM images of the ELP_{V3IE}-80-RLP-40 construct at pH 7.4.

10. Conclusion and Outlook

In conclusion, it seems that both of the pursued strategies in generating vesicular structures failed quite spectacularly. Furthermore, the constructs with the charge-bearing coronal blocks had also failed to show any of the hypothesized pH-dependent rearrangements. Over all analyzed constructs, the only two that showed some potential in terms of vesicle formation were $ELP_{V3IE,40}$-RLP_{40} and $ELP_{V3IE,80}$-RLP_{40}. Though the acquired cryo-TEM images provide some evidence against vesicle formation, additional experiments are necessary to characterize the morphology of these constructs in more depth. At this point the first project of this master thesis however started taking off, due to which we made the decision to abandon our efforts to generate vesicles.

If we were to revisit this idea some other time, then the preliminary experiments of this third subproject still provide some valuable insights:

For one, the generation of vesicles is generally a significantly more complex matter than the creation of micelles. Though simple dissolution of the polypeptides might be the easiest option, it most certainly is not the one best suited for vesicle formation. Today, vesicles based on lipids or synthetic polymers are typically created by more sophisticated preparation procedures such as thin film rehydration, sonication or membrane extrusion[150].

Secondly, previously published studies as well as the results discussed in this study indicate that the relative lengths of the individual blocks within the ELP copolymers is one of the absolutely critical variables for the resulting morphologies. Therefore, future scientists working on ELP constructs that form vesicles would probably be well advised to limit themselves to only two core-forming and coronal blocks each and instead focus on exploring many different di- and triblock architectures[143].

Thirdly, the orientation of the individual molecules within the self-assembled structure seems very important for vesicle formation. Ideally, one would want the individual molecules of a vesicle membrane to assemble in a highly regular, side-by-side manner that induces minimal curvature. For the RLP-based constructs studied in this subproject, the reality was probably quite the opposite: As the RLP block resided in its phase-separated state – a state with a very limited degree of order on the macroscopic level – it was simply way easier for the ELP blocks to adopt a star-shaped orientation than to force themselves into the highly ordered, parallel arrangement within a vesicle membrane. Thus, it might be a good idea to choose a core-forming block that still remains solvated at the temperature of interest to give the molecules more freedom to arrange in a parallel fashion.

Lastly, the rather confusing results for the TB-40 and TB-80 constructs described in section 9.1 indicate that the triblock architecture by itself might also already cause some unforeseen trouble. Therefore, it might be a good idea to focus on di- rather than triblock architectures as the general behavior of the former is way better understood at this point.

11. Acknowledgments

First of all, I would like to thank Prof. Dr. Ashutosh Chilkoti for giving me this opportunity to perform my master project work in his research group at Duke University. I realize that short research visits such as mine are generally regarded as rather unproductive arrangements which makes me appreciate his invitation to come to his labs at Duke even more.

Secondly, I would like to express my deep gratitude to Dr. Michael Dzuricky for being the best supervisor, teacher and mentor that I could have hoped for. Without his constant support and mentorship, I would most certainly have only been able to achieve a small fraction of what I did in reality. Though he was always there for me when I needed advice, he also gave me the freedom to pursue my own ideas as they came up which I appreciated a lot. Thanks Mike!

Thirdly, I would like to thank Krissey Lloyd for taking care of the lab and the therein contained supplies and equipment so meticulously. I cannot even start to imagine how disorganized the lab would have been without her. I would also like to thank her for helping me so patiently with all the administrative things that such a research visit encompasses.

Fourthly, I would like to thank Junseon Min for helping me with the SPR measurements. I realize that the measurements probably turned out to be rather more work than expected after our initial discussion. I greatly appreciated her patience and advice during the performance and analysis of the SPR measurements.

A big thank you also goes out to all members of the Chilkoti lab. I greatly enjoyed all our conversations in- and outside of the lab and I am very happy for all the friendships that formed during the last nine months.

Also, I would like to thank Prof. Dr. Michael Nash for helping me establish contact with Prof. Chilkoti back in 2018 and for being the second assessor of my master thesis.

Additionally, I would like to thank the Swiss Nanoscience Institute for their financial support through the Nanoscience Travel Grant.

And last but not least, I would like to express my deepest gratitude to my girlfriend, my family and my friends back at home in Switzerland. Though we were separated by an entire ocean and six hours in time difference, it never really felt like that. Such an adventure to a foreign country inevitably brings some lonely moments with itself and I greatly appreciate your constant support, friendship and love.

References

1. Bray, F. *et al.* Global cancer statistics 2018: GLOBOCAN estimates of incidence and mortality worldwide for 36 cancers in 185 countries. *CA. Cancer J. Clin.* **68**, 394–424 (2018).
2. Google Scholar. https://scholar.google.ch/schhp?hl=de&as_sdt=1,5.
3. DeVita, V. T. & Chu, E. A History of Cancer Chemotherapy. *Cancer Res.* **68**, 8643–8653 (2008).
4. Allen, T. M. Ligand-targeted therapeutics in anticancer therapy. *Nat. Rev. Cancer* **2**, 750 (2002).
5. Polakis, P. Antibody Drug Conjugates for Cancer Therapy. *Pharmacol. Rev.* **68**, 3–19 (2016).
6. Fang, J., Nakamura, H. & Maeda, H. The EPR effect: Unique features of tumor blood vessels for drug delivery, factors involved, and limitations and augmentation of the effect. *Adv. Drug Deliv. Rev.* **63**, 136–151 (2011).
7. Ranganathan, R. *et al.* Nanomedicine: towards development of patient-friendly drug-delivery systems for oncological applications. *Int. J. Nanomedicine* **7**, 1043 (2012).
8. Singh, R. & Lillard, J. W. Nanoparticle-based targeted drug delivery. *Exp. Mol. Pathol.* **86**, 215–223 (2009).
9. Mudshinge, S. R., Deore, A. B., Patil, S. & Bhalgat, C. M. Nanoparticles: Emerging carriers for drug delivery. *Saudi Pharm. J.* **19**, 129–141 (2011).
10. Sercombe, L. *et al.* Advances and Challenges of Liposome Assisted Drug Delivery. *Front. Pharmacol.* **6**, (2015).
11. Anajafi, T. & Mallik, S. Polymersome-based drug-delivery strategies for cancer therapeutics. *Ther. Deliv.* **6**, 521–534 (2015).
12. Puri, A. *et al.* Lipid-Based Nanoparticles as Pharmaceutical Drug Carriers: From Concepts to Clinic. *Crit. Rev. Ther. Drug Carr. Syst.* **26**, (2009).
13. McDaniel, J. R., Callahan, D. J. & Chilkoti, A. Drug delivery to solid tumors by elastin-like polypeptides. *Adv. Drug Deliv. Rev.* **62**, 1456–1467 (2010).
14. Gray, W. R., Sandberg, L. B. & Foster, J. A. Molecular Model for Elastin Structure and Function. *Nature* **246**, 461–466 (1973).
15. Urry, D. W., Cunningham, W. D. & Ohnishi, T. Conformation and interactions of elastin. Proton magnetic resonance of the repeating pentapeptide. *Biochemistry* **13**, 609–616 (1974).
16. Urry, D. W. *et al.* Temperature of polypeptide inverse temperature transition depends on mean residue hydrophobicity. *J. Am. Chem. Soc.* **113**, 4346–4348 (1991).
17. Urry, D. W. *et al.* Hydrophobicity scale for proteins based on inverse temperature transitions. *Biopolymers* **32**, 1243–1250 (1992).
18. Meyer, D. E. & Chilkoti, A. Quantification of the effects of chain length and concentration on the thermal behavior of elastin-like polypeptides. *Biomacromolecules* **5**, 846–851 (2004).
19. Luan, C.-H., Parker, T. M., Prasad, K. U. & Urry, D. W. Differential scanning calorimetry studies of NaCl effect on the inverse temperature transition of some elastin-based polytetra-, polypenta-, and polynonapeptides. *Biopolymers* **31**, 465–475 (1991).
20. Meyer, D. E. & Chilkoti, A. Purification of recombinant proteins by fusion with thermally-responsive polypeptides. *Nat. Biotechnol.* **17**, 1112–1115 (1999).
21. Cho, Y. *et al.* Effects of Hofmeister Anions on the Phase Transition Temperature of Elastin-like Polypeptides. *J. Phys. Chem. B* **112**, 13765–13771 (2008).
22. Seuring, J. Polymers with Upper Critical Solution Temperature in Aqueous Solution. (2012).
23. Elvin, C. M. *et al.* Synthesis and properties of crosslinked recombinant pro-resilin. *Nature* **437**, 999–1002 (2005).
24. Lyons, R. E. *et al.* Design and facile production of recombinant resilin-like polypeptides: gene construction and a rapid protein purification method. *Protein Eng. Des. Sel.* **20**, 25–32 (2007).
25. Quiroz, F. G. & Chilkoti, A. Sequence heuristics to encode phase behaviour in intrinsically disordered protein polymers. *Nat. Mater.* **14**, 1164–1171 (2015).
26. Dutta, N. K. *et al.* A Genetically Engineered Protein Responsive to Multiple Stimuli. *Angew. Chem. Int. Ed.* **50**, 4428–4431 (2011).
27. Li, L., Luo, T. & Kiick, K. L. Temperature-Triggered Phase Separation of a Hydrophilic Resilin-Like Polypeptide. *Macromol. Rapid Commun.* **36**, 90–95 (2015).
28. Li, L., Tong, Z., Jia, X. & L. Kiick, K. Resilin-like polypeptide hydrogels engineered for versatile biological function. *Soft Matter* **9**, 665–673 (2013).
29. Weitzhandler, I. *et al.* Micellar Self-Assembly of Recombinant Resilin-/Elastin-Like Block Copolypeptides. *Biomacromolecules* **18**, 2419–2426 (2017).
30. Dzuricky, M., Xiong, S., Weber, P. & Chilkoti, A. Avidity and Cell Uptake of Integrin-Targeting Polypeptide Micelles is Strongly Shape-Dependent. *Nano Lett.* **19**, 6124–6132

(2019).
31. Urry, D. W., Parker, T. M., Reid, M. C. & Gowda, D. C. Biocompatibility of the Bioelastic Materials, Poly(GVGVP) and Its γ-Irradiation Cross-Linked Matrix: Summary of Generic Biological Test Results. *J. Bioact. Compat. Polym.* **6**, 263–282 (1991).
32. Liu, W. *et al.* Tumor accumulation, degradation and pharmacokinetics of elastin-like polypeptides in nude mice. *J. Controlled Release* **116**, 170–178 (2006).
33. Dreher, M. R., Liu, W., Michelich, C. R., Dewhirst, M. W. & Chilkoti, A. Thermal Cycling Enhances the Accumulation of a Temperature-Sensitive Biopolymer in Solid Tumors. *Cancer Res.* **67**, 4418–4424 (2007).
34. Dreher, M. R. *et al.* Temperature Triggered Self-Assembly of Polypeptides into Multivalent Spherical Micelles. *J. Am. Chem. Soc.* **130**, 687–694 (2008).
35. Simnick, A. J., Valencia, C. A., Liu, R. & Chilkoti, A. Morphing Low-Affinity Ligands into High-Avidity Nanoparticles by Thermally Triggered Self-Assembly of a Genetically Encoded Polymer. *ACS Nano* **4**, 2217–2227 (2010).
36. Frenkel, V. Ultrasound mediated delivery of drugs and genes to solid tumors. *Adv. Drug Deliv. Rev.* **60**, 1193–1208 (2008).
37. Yuba, E., Harada, A., Sakanishi, Y. & Kono, K. Carboxylated hyperbranched poly(glycidol)s for preparation of pH-sensitive liposomes. *J. Controlled Release* **149**, 72–80 (2011).
38. Chen, W., Meng, F., Cheng, R. & Zhong, Z. pH-Sensitive degradable polymersomes for triggered release of anticancer drugs: A comparative study with micelles. *J. Controlled Release* **142**, 40–46 (2010).
39. Liu, J. *et al.* pH-Sensitive nano-systems for drug delivery in cancer therapy. *Biotechnol. Adv.* **32**, 693–710 (2014).
40. Cardone, R. A., Casavola, V. & Reshkin, S. J. The role of disturbed pH dynamics and the Na + /H + exchanger in metastasis. *Nat. Rev. Cancer* **5**, 786–795 (2005).
41. Callahan, D. J. *et al.* Triple Stimulus-Responsive Polypeptide Nanoparticles That Enhance Intratumoral Spatial Distribution. *Nano Lett.* **12**, 2165–2170 (2012).
42. Andrew MacKay, J. *et al.* Self-assembling chimeric polypeptide–doxorubicin conjugate nanoparticles that abolish tumours after a single injection. *Nat. Mater.* **8**, 993–999 (2009).
43. Li, L. & Kiick, K. L. Resilin-Based Materials for Biomedical Applications. *ACS Macro Lett.* **2**, 635–640 (2013).
44. McDaniel, J. R., MacKay, J. A., Quiroz, F. G. & Chilkoti, A. Recursive Directional Ligation by Plasmid Reconstruction Allows Rapid and Seamless Cloning of Oligomeric Genes. *Biomacromolecules* **11**, 944–952 (2010).
45. Meyer, D. E. & Chilkoti, A. Genetically encoded synthesis of protein-based polymers with precisely specified molecular weight and sequence by recursive directional ligation: examples from the elastin-like polypeptide system. *Biomacromolecules* **3**, 357–367 (2002).
46. Benkoulouche, M. Part:BBa_K1317003. *Registry of Standard Biological Parts* http://parts.igem.org/Part:BBa_K1317003 (2019).
47. Dreher, M. R. *et al.* Evaluation of an elastin-like polypeptide–doxorubicin conjugate for cancer therapy. *J. Controlled Release* **91**, 31–43 (2003).
48. Van Domeselaar, G. H., Kwon, G. S., Andrew, L. C. & Wishart, D. S. Application of solid phase peptide synthesis to engineering PEO–peptide block copolymers for drug delivery. *Colloids Surf. B Biointerfaces* **30**, 323–334 (2003).
49. Ranger, M., Jones, M.-C., Yessine, M.-A. & Leroux, J.-C. From well-defined diblock copolymers prepared by a versatile atom transfer radical polymerization method to supramolecular assemblies. *J. Polym. Sci. Part Polym. Chem.* **39**, 3861–3874 (2001).
50. Bast, A., Kaiserová, H., den Hartog, G. J. M., Haenen, G. R. M. M. & van der Vijgh1, W. J. F. Protectors against doxorubicin-induced cardiotoxicity: Flavonoids. *Cell Biol. Toxicol.* **23**, 39–47 (2007).
51. Liebmann, J. E. *et al.* Cytotoxic studies of paclitaxel (Taxol ®) in human tumour cell lines. *Br. J. Cancer* **68**, 1104–1109 (1993).
52. Swers, J. S. *et al.* Multivalent Scaffold Proteins as Superagonists of TRAIL Receptor 2–Induced Apoptosis. *Mol. Cancer Ther.* **12**, 1235–1244 (2013).
53. Xu, P. *et al.* Highly stable core-surface-cross-linked nanoparticles as cisplatin carriers for cancer chemotherapy. *Colloids Surf. B Biointerfaces* **48**, 50–57 (2006).
54. Shuai, X., Merdan, T., Schaper, A. K., Xi, F. & Kissel, T. Core-Cross-Linked Polymeric Micelles as Paclitaxel Carriers. *Bioconjug. Chem.* **15**, 441–448 (2004).
55. Liu, S. *et al.* Synthesis of Shell Cross-Linked Micelles with pH-Responsive Cores Using ABC Triblock Copolymers. *Macromolecules* **35**, 6121–6131 (2002).
56. Joo, K.-I. *et al.* Crosslinked multilamellar liposomes for controlled delivery of anticancer drugs. *Biomaterials* **34**, 3098–3109 (2013).
57. Edwards, I. R. & Aronson, J. K. Adverse drug reactions: definitions, diagnosis, and management. *The Lancet* **356**, 1255–1259 (2000).
58. Chung, C., Lampe, K. J. & Heilshorn, S. C.

Tetrakis(hydroxymethyl) Phosphonium Chloride as a Covalent Cross-Linking Agent for Cell Encapsulation within Protein-Based Hydrogels. *Biomacromolecules* **13**, 3912–3916 (2012).
59. Lim, D. W., Nettles, D. L., Setton, L. A. & Chilkoti, A. Rapid Cross-Linking of Elastin-like Polypeptides with (Hydroxymethyl)phosphines in Aqueous Solution. *Biomacromolecules* **8**, 1463–1470 (2007).
60. Nettles, D. L. *et al.* In situ crosslinking elastin-like polypeptide gels for application to articular cartilage repair in a goat osteochondral defect model. *Tissue Eng. Part A* **14**, 1133–1140 (2008).
61. Raphel, J., Parisi-Amon, A. & C. Heilshorn, S. Photoreactive elastin-like proteins for use as versatile bioactive materials and surface coatings. *J. Mater. Chem.* **22**, 19429–19437 (2012).
62. McHale, M. K., Setton, L. A. & Chilkoti, A. Synthesis and in Vitro Evaluation of Enzymatically Cross-Linked Elastin-Like Polypeptide Gels for Cartilaginous Tissue Repair. *Tissue Eng.* **11**, 1768–1779 (2005).
63. Leitner, A. *et al.* Probing Native Protein Structures by Chemical Cross-linking, Mass Spectrometry, and Bioinformatics. *Mol. Cell. Proteomics* **9**, 1634–1649 (2010).
64. Preston, G. W. & Wilson, A. J. Photo-induced covalent cross-linking for the analysis of biomolecular interactions. *Chem. Soc. Rev.* **42**, 3289–3301 (2013).
65. Costa, S. A. *et al.* Photo-Crosslinkable Unnatural Amino Acids Enable Facile Synthesis of Thermoresponsive Nano-to Microgels of Intrinsically Disordered Polypeptides. *Adv. Mater.* **30**, 1704878 (2018).
66. Nwe, K. & Brechbiel, M. W. Growing Applications of "Click Chemistry" for Bioconjugation in Contemporary Biomedical Research. *Cancer Biother. Radiopharm.* **24**, 289–302 (2009).
67. Mavila, S., Eivgi, O., Berkovich, I. & Lemcoff, N. G. Intramolecular Cross-Linking Methodologies for the Synthesis of Polymer Nanoparticles. *Chem. Rev.* **116**, 878–961 (2016).
68. Li, G., Tao, F., Wang, L., Li, Y. & Bai, R. A facile strategy for preparation of single-chain polymeric nanoparticles by intramolecular photo-crosslinking of azide polymers. *Polymer* **55**, 3696–3702 (2014).
69. Jiang, X., Pu, H. & Wang, P. Polymer nanoparticles via intramolecular crosslinking of sulfonyl azide functionalized polymers. *Polymer* **52**, 3597–3602 (2011).
70. Gritsan, N. P. & Platz, M. S. Kinetics, Spectroscopy, and Computational Chemistry of Arylnitrenes. *Chem. Rev.* **106**, 3844–3867 (2006).
71. Gritsan, N. & Platz, M. *Photochemistry of azides: the azide/nitrene interface*. (John Wiley & Sons: Hoboken, NJ, USA, 2010).
72. Hofmann, K. & Bohn, H. Studies on Polypeptides. XXXVI. The Effect of Pyrazole—Imidazole Replacements on the S-Protein Activating Potency of an S-Peptide Fragment1-3. *J. Am. Chem. Soc.* **88**, 5914–5919 (1966).
73. Borrás, F. & Offord, R. E. Protected Intermediate for the Preparation of Semisynthetic Insulins. *Nature* **227**, 716–718 (1970).
74. Inouye, K. *et al.* Enzyme-assisted semisynthesis of human insulin. *J. Am. Chem. Soc.* **101**, 751–752 (1979).
75. Noren, C. J., Anthony-Cahill, S. J., Griffith, M. C. & Schultz, P. G. A general method for site-specific incorporation of unnatural amino acids into proteins. *Science* **244**, 182–188 (1989).
76. Bain, J. D., Diala, E. S., Glabe, C. G., Dix, T. A. & Chamberlin, A. R. Biosynthetic site-specific incorporation of a non-natural amino acid into a polypeptide. *J. Am. Chem. Soc.* **111**, 8013–8014 (1989).
77. Bruce, A. G., Atkins, J. F., Wills, N., Uhlenbeck, O. & Gesteland, R. F. Replacement of anticodon loop nucleotides to produce functional tRNAs: amber suppressors derived from yeast tRNAPhe. *Proc. Natl. Acad. Sci.* **79**, 7127–7131 (1982).
78. Young, T. S. & Schultz, P. G. Beyond the Canonical 20 Amino Acids: Expanding the Genetic Lexicon. *J. Biol. Chem.* **285**, 11039–11044 (2010).
79. Amiram, M. *et al.* Evolution of translation machinery in recoded bacteria enables multi-site incorporation of nonstandard amino acids. *Nat. Biotechnol.* **33**, 1272 (2015).
80. Young, T. S., Ahmad, I., Yin, J. A. & Schultz, P. G. An Enhanced System for Unnatural Amino Acid Mutagenesis in E. coli. *J. Mol. Biol.* **395**, 361–374 (2010).
81. Isaacs, F. J. *et al.* Precise Manipulation of Chromosomes in Vivo Enables Genome-Wide Codon Replacement. *Science* **333**, 348–353 (2011).
82. Lajoie, M. J. *et al.* Genomically recoded organisms expand biological functions. *science* **342**, 357–360 (2013).
83. Bowditch, R. D. *et al.* Identification of a novel integrin binding site in fibronectin. Differential utilization by beta 3 integrins. *J. Biol. Chem.* **269**, 10856–10863 (1994).
84. Richards, J. *et al.* Engineered Fibronectin Type III Domain with a RGDWXE Sequence Binds with Enhanced Affinity and Specificity to Human αvβ3 Integrin. *J. Mol. Biol.* **326**, 1475–1488 (2003).
85. Liu, Z., Wang, F. & Chen, X. Integrin αvβ3-targeted cancer therapy. *Drug Dev. Res.* **69**,

329–339 (2008).
86. Ruoslahti, E. Rgd and Other Recognition Sequences for Integrins. *Annu. Rev. Cell Dev. Biol.* **12**, 697–715 (1996).
87. Englund, E. A. *et al.* Programmable multivalent display of receptor ligands using peptide nucleic acid nanoscaffolds. *Nat. Commun.* **3**, 614 (2012).
88. Jin, Z.-H. *et al.* Effect of Multimerization of a Linear Arg-Gly-Asp Peptide on Integrin Binding Affinity and Specificity. *Biol. Pharm. Bull.* **33**, 370–378 (2010).
89. Manzari, M. T. *et al.* Genomically informed small-molecule drugs overcome resistance to a sustained-release formulation of an engineered death receptor agonist in patient-derived tumor models. *Sci. Adv.* **5**, eaaw9162 (2019).
90. Angell, Y. M. *et al.* Discovery and Optimization of a TRAIL R2 Agonist for Cancer Therapy. in *Peptides for Youth* (eds. Valle, S. D., Escher, E. & Lubell, W. D.) 101–103 (Springer New York, 2009).
91. Pavet, V. *et al.* Multivalent DR5 Peptides Activate the TRAIL Death Pathway and Exert Tumoricidal Activity. *Cancer Res.* **70**, 1101–1110 (2010).
92. Wiley, S. R. *et al.* Identification and characterization of a new member of the TNF family that induces apoptosis. *Immunity* **3**, 673–682 (1995).
93. Han, J. H. *et al.* Potentiation of TRAIL killing activity by multimerization through isoleucine zipper hexamerization motif. *BMB Rep.* **49**, 282–287 (2016).
94. Falschlehner, C., Emmerich, C. H., Gerlach, B. & Walczak, H. TRAIL signalling: Decisions between life and death. *Int. J. Biochem. Cell Biol.* **39**, 1462–1475 (2007).
95. Pan, L. *et al.* Higher-Order Clustering of the Transmembrane Anchor of DR5 Drives Signaling. *Cell* **176**, 1477-1489.e14 (2019).
96. Park, B.-W. *et al.* Rationally designed anti-HER2/neu peptide mimetic disables P185 HER2/neu tyrosine kinases in vitro and in vivo. *Nat. Biotechnol.* **18**, 194 (2000).
97. Wang, J., Dzuricky, M. & Chilkoti, A. The Weak Link: Optimization of the Ligand–Nanoparticle Interface To Enhance Cancer Cell Targeting by Polymer Micelles. *Nano Lett.* **17**, 5995–6005 (2017).
98. Wang, K. *et al.* Novel mode of action of polybia-MPI, a novel antimicrobial peptide, in multi-drug resistant leukemic cells. *Cancer Lett.* **278**, 65–72 (2009).
99. Schweizer, F. Cationic amphiphilic peptides with cancer-selective toxicity. *Eur. J. Pharmacol.* **625**, 190–194 (2009).
100. Oren, Z. & Shai, Y. Selective Lysis of Bacteria but Not Mammalian Cells by Diastereomers of Melittin: Structure−Function Study. *Biochemistry* **36**, 1826–1835 (1997).
101. Valencia, P. M. *et al.* Effects of ligands with different water solubilities on self-assembly and properties of targeted nanoparticles. *Biomaterials* **32**, 6226–6233 (2011).
102. Stefanick, J. F., Ashley, J. D., Kiziltepe, T. & Bilgicer, B. A Systematic Analysis of Peptide Linker Length and Liposomal Polyethylene Glycol Coating on Cellular Uptake of Peptide-Targeted Liposomes. *ACS Nano* **7**, 2935–2947 (2013).
103. Stefanick, J. F., Ashley, J. D. & Bilgicer, B. Enhanced Cellular Uptake of Peptide-Targeted Nanoparticles through Increased Peptide Hydrophilicity and Optimized Ethylene Glycol Peptide-Linker Length. *ACS Nano* **7**, 8115–8127 (2013).
104. Kuwajima, K., Nitta, K., Yoneyama, M. & Sugai, S. Three-state denaturation of α-lactalbumin by guanidine hydrochloride. *J. Mol. Biol.* **106**, 359–373 (1976).
105. Tanford, C. Protein denaturation. in *Advances in protein chemistry* vol. 23 121–282 (Elsevier, 1968).
106. McDaniel, J. R. *et al.* Noncanonical Self-Assembly of Highly Asymmetric Genetically Encoded Polypeptide Amphiphiles into Cylindrical Micelles. *Nano Lett.* **14**, 6590–6598 (2014).
107. Rharbi, Y. Fusion and Fragmentation Dynamics at Equilibrium in Triblock Copolymer Micelles. *Macromolecules* **45**, 9823–9826 (2012).
108. Johnson, B. K. & Prud'homme, R. K. Mechanism for Rapid Self-Assembly of Block Copolymer Nanoparticles. *Phys. Rev. Lett.* **91**, 118302 (2003).
109. Passmore, L. A. & Russo, C. J. Specimen preparation for high-resolution cryo-EM. *Methods Enzymol.* **579**, 51–86 (2016).
110. Thompson, R. F., Walker, M., Siebert, C. A., Muench, S. P. & Ranson, N. A. An introduction to sample preparation and imaging by cryo-electron microscopy for structural biology. *Methods* **100**, 3–15 (2016).
111. Jacobsen, L. B., Calvin, S. A. & Lobenhofer, E. K. Transcriptional effects of transfection: the potential for misinterpretation of gene expression data generated from transiently transfected cells. *BioTechniques* **47**, 617–624 (2009).
112. Zhao, J. & H. Stenzel, M. Entry of nanoparticles into cells: the importance of nanoparticle properties. *Polym. Chem.* **9**, 259–272 (2018).
113. Berg, O. G. & von Hippel, P. H. Diffusion-Controlled Macromolecular Interactions. *Annu. Rev. Biophys. Biophys. Chem.* **14**, 131–158 (1985).
114. Schreiber, G. Kinetic studies of protein–protein interactions. *Curr. Opin. Struct. Biol.* **12**,

41–47 (2002).
115. Li, S.-D. & Huang, L. Pharmacokinetics and Biodistribution of Nanoparticles. *Mol. Pharm.* **5**, 496–504 (2008).
116. Owens, D. E. & Peppas, N. A. Opsonization, biodistribution, and pharmacokinetics of polymeric nanoparticles. *Int. J. Pharm.* **307**, 93–102 (2006).
117. Arvizo, R. R. *et al.* Modulating Pharmacokinetics, Tumor Uptake and Biodistribution by Engineered Nanoparticles. *PLOS ONE* **6**, e24374 (2011).
118. Motornov, M., Roiter, Y., Tokarev, I. & Minko, S. Stimuli-responsive nanoparticles, nanogels and capsules for integrated multifunctional intelligent systems. *Prog. Polym. Sci.* **35**, 174–211 (2010).
119. Moktan, S., Perkins, E., Kratz, F. & Raucher, D. Thermal Targeting of an Acid-Sensitive Doxorubicin Conjugate of Elastin-like Polypeptide Enhances the Therapeutic Efficacy Compared with the Parent Compound In Vivo. *Mol. Cancer Ther.* **11**, 1547–1556 (2012).
120. Wu, J. *et al.* Hydrophobic Cysteine Poly(disulfide)-based Redox-Hypersensitive Nanoparticle Platform for Cancer Theranostics. *Angew. Chem. Int. Ed.* **54**, 9218–9223 (2015).
121. Thirumurugan, P., Matosiuk, D. & Jozwiak, K. Click Chemistry for Drug Development and Diverse Chemical–Biology Applications. *Chem. Rev.* **113**, 4905–4979 (2013).
122. Hartley, J. L. & Gregori, T. J. Cloning multiple copies of a DNA segment. *Gene* **13**, 347–353 (1981).
123. Simpson, R. T., Thoma, F. & Brubaker, J. M. Chromatin reconstituted from tandemly repeated cloned DNA fragments and core histones: A model system for study of higher order structure. *Cell* **42**, 799–808 (1985).
124. Kim, S. C. & Szybalski, W. Amplification of cloned DNA as tandem multimers using BspMI-generated asymmetric cohesive ends. *Gene* **71**, 1–8 (1988).
125. Prince, J. T., McGrath, K. P., DiGirolamo, C. M. & Kaplan, D. L. Construction, cloning, and expression of synthetic genes encoding spider dragline silk. *Biochemistry* **34**, 10879–10885 (1995).
126. McPherson, D. T., Xu, J. & Urry, D. W. Product Purification by Reversible Phase Transition FollowingEscherichia coliExpression of Genes Encoding up to 251 Repeats of the Elastomeric Pentapeptide GVGVP. *Protein Expr. Purif.* **7**, 51–57 (1996).
127. Amiram, M., Quiroz, F. G., Callahan, D. J. & Chilkoti, A. A highly parallel method for synthesizing DNA repeats enables the discovery of 'smart' protein polymers. *Nat. Mater.* **10**, 141–148 (2011).
128. White, M. J., Fristensky, B. W. & Thompson, W. F. Concatemer chain reaction: A taq DNA polymerase-mediated mechanism for generating long tandemly repetitive DNA sequences. *Anal. Biochem.* **199**, 184–190 (1991).
129. Zhao, W., Ali, M. M., Brook, M. A. & Li, Y. Rolling Circle Amplification: Applications in Nanotechnology and Biodetection with Functional Nucleic Acids. *Angew. Chem. Int. Ed.* **47**, 6330–6337 (2008).
130. New England Biolabs. Why do I need to add PEG to my DNA ligation? https://international.neb.com/tools-and-resources/video-library/why-do-i-need-to-add-peg-to-my-dna-ligation (2019).
131. Fujiyama, J. *et al.* Cisplatin incorporated in microspheres: development and fundamental studies for its clinical application. *J. Controlled Release* **89**, 397–408 (2003).
132. Dhar, S., Gu, F. X., Langer, R., Farokhzad, O. C. & Lippard, S. J. Targeted delivery of cisplatin to prostate cancer cells by aptamer functionalized Pt(IV) prodrug-PLGA-PEG nanoparticles. *Proc. Natl. Acad. Sci. U. S. A.* **105**, 17356–17361 (2008).
133. Huang, X. & Voit, B. Progress on multi-compartment polymeric capsules. *Polym. Chem.* **4**, 435–443 (2013).
134. Thamboo, S. *et al.* Mimicking Cellular Signaling Pathways within Synthetic Multicompartment Vesicles with Triggered Enzyme Activity and Induced Ion Channel Recruitment. *Adv. Funct. Mater.* **29**, 1904267 (2019).
135. Haley, B. & Frenkel, E. Nanoparticles for drug delivery in cancer treatment. *Urol. Oncol. Semin. Orig. Investig.* **26**, 57–64 (2008).
136. Maruyama, K. Intracellular targeting delivery of liposomal drugs to solid tumors based on EPR effects. *Adv. Drug Deliv. Rev.* **63**, 161–169 (2011).
137. U.S. Federal Drug Administration. Approval Package for: NDA 50-718/S-50. *CENTER FOR DRUG EVALUATION AND RESEARCH* https://www.accessdata.fda.gov/drugsatfda_docs/nda/2015/050718Orig1s050.pdf (2015).
138. Zhang, X. & Zhang, P. Polymersomes in Nanomedicine - A Review. *Curr. Med. Chem.* **13**, 124–129 (2017).
139. Martín, L., Castro, E., Ribeiro, A., Alonso, M. & Rodríguez-Cabello, J. C. Temperature-Triggered Self-Assembly of Elastin-Like Block Co-Recombinamers:The Controlled Formation of Micelles and Vesicles in an Aqueous Medium. *Biomacromolecules* **13**, 293–298 (2012).
140. Herrero-Vanrell, R. *et al.* Self-assembled particles of an elastin-like polymer as vehicles for controlled drug release. *J. Controlled Release* **102**, 113–122 (2005).

141. Reguera, J. *et al.* Thermal Behavior and Kinetic Analysis of the Chain Unfolding and Refolding and of the Concomitant Nonpolar Solvation and Desolvation of Two Elastin-like Polymers. *Macromolecules* **36**, 8470–8476 (2003).
142. Luo, T. & Kiick, K. L. Noncovalent Modulation of the Inverse Temperature Transition and Self-Assembly of Elastin-b-Collagen-like Peptide Bioconjugates. *J. Am. Chem. Soc.* **137**, 15362–15365 (2015).
143. Antonietti, M. & Förster, S. Vesicles and Liposomes: A Self-Assembly Principle Beyond Lipids. *Adv. Mater.* **15**, 1323–1333 (2003).
144. Agut, W., Brûlet, A., Schatz, C., Taton, D. & Lecommandoux, S. pH and Temperature Responsive Polymeric Micelles and Polymersomes by Self-Assembly of Poly[2-(dimethylamino)ethyl methacrylate]-b-Poly(glutamic acid) Double Hydrophilic Block Copolymers. *Langmuir* **26**, 10546–10554 (2010).
145. Sanson, C. *et al.* A simple method to achieve high doxorubicin loading in biodegradable polymersomes. *J. Controlled Release* **147**, 428–435 (2010).
146. Bellomo, E. G., Wyrsta, M. D., Pakstis, L., Pochan, D. J. & Deming, T. J. Stimuli-responsive polypeptide vesicles by conformation-specific assembly. *Nat. Mater.* **3**, 244–248 (2004).
147. Urry, D. W., Peng, S. Q. & Parker, T. M. Hydrophobicity-induced pK shifts in elastin protein-based polymers. *Biopolymers* **32**, 373–379 (1992).
148. Urry, D. W. *et al.* Nanometric design of extraordinary hydrophobic-induced pKa shifts for aspartic acid: Relevance to protein mechanisms. *Biopolymers* **34**, 889–896 (1994).
149. Dzuricky, M. Oral report on the morphology of typical ELP aggregates formed in microfluidic droplets upon heating above their transition temperature. (2019).
150. Lee, J. C.-M. *et al.* Preparation, stability, and in vitro performance of vesicles made with diblock copolymers. *Biotechnol. Bioeng.* **73**, 135–145 (2001).

Appendix

A – Experimental Section

A.i Cloning

Vectors

In this study, two different vectors were used for the gene synthesis steps which from now on shall be referred to as JMD2 and NCT2. The former was employed for the gene assembly of all constructs investigated in this study and for expression of the *p*AzF-free constructs. For the *p*AzF-containing constructs, the genes were transferred into the latter vector during the final cloning step before expression. Both vectors are based on the pET-24+ cloning plasmid. In JMD2, the main difference is the introduction of the *AcuI*, *BseRI* and *BglI* recognition sites required for the PRe-RDL procedure. In the NCT2 vector on the other hand, the T7 promoter and terminator sequences were replaced by a pTac promoter and an rrnB terminator which makes this vector more compatible with protein expression in the genomically recoded *E. coli* strain used for *p*AzF-expression.

Lastly, a vector encoding an orthogonal tRNA/aaRS pair was also required for unnatural amino acid expression. The corresponding pEVOL plasmid that contained two copies of the pAcFRS.1.t1 synthetase was generously provided by Prof. Farren J. Isaacs (Yale University, USA).

Procedures

If the DNA construct of interest was novel and could not be provided by other lab members, it was ordered as a gBlock from Integrated DNA Technologies (Coralville IA, USA) and inserted into the linearised vector of choice by coincubating the two fragments with Gibson assembly® master mix (New England Biolabs, Ipswitch MA, USA) at 50°C for 1 hour. Subsequently, 1 µL was used for the transformation of NEB® 5-alpha competent cells (see New England Biolabs website for detailed protocol). The bacteria were plated on 2xYT agar plates supplemented with the corresponding antibiotic(s) and incubated overnight at 37°C.

For subsequent gene synthesis via PRe-RDL, the bacterial stocks containing the to-be-merged constructs were grown up overnight in 2xYT media (16 g/L tryptone, 10 g/L yeast extract and 5 g/L NaCl) supplemented with kanamycin (45 µg/mL) at 37°C and 210 rpm (Excella E24 shaker incubator, New Brunswick Scientific, Edison NJ, USA). After extraction and purification of the DNA using the QIAprep spin miniprep kit (Qiagen, Hilden, GER), the plasmids were subjected to digestion for 2-3 hours at 37°C using buffers and rescriction enzymes manufactured by New England Biolabs (Ipswitch MA, USA). Subsequently, the created DNA fragments were separated via gel electrophoresis on a 1% agarose gel (in tris-acetate-EDTA buffer supplemented with 0.1‰ SYBR Safe stain (Invitrogen, Carlsbad CA, USA)) at 130V for 20-40 minutes (EPS-300 X Power Supply, Fisher Scientific, Hampton NH, USA) and purified using the QIAquick gel extraction kit (Qiagen, Hilden, GER). To ligate the fragments, T4 DNA ligase and corresponding buffer (both New England Biolabs, Ipswitch MA, USA) were used. The reaction mixture was incubated at room temperature for 1 hour before 1-5 µL (40-200 ng of DNA) were used for the transformation of NEB® 5-alpha competent cells

(see New England Biolabs website for detailed protocol). The bacteria were plated on 2xYT agar plates supplemented with kanamycin (45 μg/mL) and incubated overnight at 37°C.

If the construct of interest contained amber stop codons ("TAG") for the introduction of *p*AzF residues, the last cloning step consisted of digesting the corresponding JMD2 vector with *BseRI* and *BamHI* (both New England Biolabs, Ipswitch MA, USA), purifying the digest following the procedures above and finally ligating the construct into the linearized, *BseRI*- and *BamHI*-cut NCT2 vector. The ligation mixture was incubated at room temperature for 1 hour before 1-5 μL (40-200 ng of DNA) were used for the transformation of genetically recoded, competent *E. coli* (C321.ΔA, generously provided by Prof Farren J. Isaacs (Yale University, USA)) that had been previously transformed with the pEVOL vector. The bacteria were plated on 2xYT agar plates supplemented with kanamycin (45 μg/mL) and chloramphenicol (25 μg/mL) and incubated overnight at 37°C.

To determine the DNA concentration at different stages of the cloning process a NanoDrop 1000 instrument was used (Thermo Fisher Scientific, Waltham MA, USA). Sequence analysis of the transformation products was performed by GENEWIZ (Morrisville NC, USA).

A.ii Polymerase Chain Reaction

In this study, PCR methods were employed for two different purposes: For one, to produce large quantities of a certain DNA fragment to be later used for cloning purposes and secondly, to analyse the length of the DNA construct contained in different colonies after transformation. As the procedures are different for these two methods, they shall be described seperately. Independently of the purpose, the PCR reaction itself was run on an ARKTIK Thermal Cycler (Thermo Fisher Scientific, Waltham MA, USA).

Regular PCR

Of the 50 μL reaction volume, 10 μL were accounted for by Herc II reaction buffer, 1 μL by Herc II enzyme, 0.5 μL by dNTPs (100 mM (25 mM each), all three reagents from Agilent Technologies, Santa Clara CA, USA), 1 μL by the to-be-amplivied DNA (typically at 10 ng/μL) and 1.25 μL each by the respective primers (10-100 μM, supplied by Integrated DNA Technologies, Coralville IA, USA). The remainder of the reaction volume was filled with water. For the PCR reaction itself, the melting temperature for each cycle was set to 98°C (for 15 seconds), the polymerisation temperature to 72°C (30 seconds) and the annealing temperature to 45°C (for T7 primers, 30 seconds). 35 PCR cycles were performed.

After the PCR reaction is complete, the DNA was purified via ethanol precipitation: To a given PCR reaction volume, 0.1 volumes of chilled sodium acetate solution (3 M, pH 5.3, 4°C) and 2 volumes of ice cold ethanol (-20°C) were added, mixed and the tube moved to -80°C for one hour. Subsequently, the tube is centrifuged at maximum speed (Microcentrifuge 5424, Eppendorf AG, Hamburg, GER) at 4°C for 30 minutes and the supernatant carefully removed. Next, the sample is washed with 1 mL of 95% ethanol, centrifuged again at identical conditions for 10 minutes, the supernatant removed, the pellet air-dried and finally dissolved in the desired volume of water.

Colony PCR

For colony PCR, the reaction volume was 25 µL of which 12.5 µL were accounted for by GoTaq Green master mix (Promega Corporation, Durham NC, USA), 12.3 µL by water and 0.1 µL each by both forward an reverse T7 primers (100 µM). Then, a small fraction of each of the to-be-analysed colonies was picked and placed in the reaction tube before the reaction was started. The parameters for the PCR reaction were identical to the ones described in the above section. To analyse the size of the encoded constructs in each of the picked colonies a 1% agarose gel was run analogously as described above.

A.iii Protein Expression and Purification

*p*AzF-free Proteins

As NEB® 5-alpha bacteria are not the most efficient cell line at expressing protein, the DNA construct of interest was transformed into BL21 (DE3) competent cells (New England Biolabs, Ipswitch MA, USA) prior to starting protein expression. The expression was then performed in 4 L erlenmeyer flasks filled with 1 L of 2xYT media supplemented with kanamycin (45 µg/mL). After the media had been inoculated with the desired bacterial strain, the cultures were incubated at 37°C and 200 rpm (GYROMAX 747, Amerex Instruments, Concord CA, USA) until they reached an OD_{600} of 0.6-0.8. At this point, protein expression was induced by the addition of IPTG (1 mL of a 1 M solution in water per culture) and the culture incubated at the same conditions overnight.

The next morning, the cells were spun down (10 minutes at 3'000 rpm and 4°C in a Sorvall RC 3B centrifuge equipt with a H6000A bucket rotor (both Thermo Fisher Scientific, Waltham MA, USA)), the supernatant decanted and the cell pellet resuspended in PBS (20 mL). Subsequently, the cells were lysed using a Qsonica Q500 sonicator (3 minutes at 75% with 10 seconds on, 40 seconds off intervals, Newtown CT, USA). After addition of a solution of 10% PEI in water (2 mL per L of resuspended cell culture), the lysate was spun down (30 minutes at 14'000 rpm and 4°C in a Beckman Coulter J2-HC centrifuge equipt with a JA-20 rotor (both Beckman Coulter, Brea CA, USA)) and the supernatant collected in a different tube. Now, ITC cycles were performed for further purification: To push the targeted protein beyond its transition temperature, the NaCl concentration of the supernatant was increased up to 3 M and the temperature increased up to 45°C. Once the protein had transitioned, the samples were subjected to another round of centrifugation (30 minutes at 14'000 rpm and 35°C in a Sorvall RC 5B centrifuge equipt with a SS34 rotor (both Thermo Fisher Scientific, Waltham MA, USA)) after which the supernatant was discarded. The pellet was then resuspended in water and at 4°C. Subsequently, the samples were spun down again (30 minutes at 14'000 rpm and 4°C in a Beckman Coulter J2-HC centrifuge equipt with a JA-20 rotor (both Beckman Coulter, Brea CA, USA)) and the supernatant transferred into a new tube to complete the ITC cycle. To determine the purity of the protein solution SDS-PAGE was performed (using 2x Laemmli sample buffer and 4-20% Mini-PROTEAN TGX precast gels (both Bio-Rad Laboratories, Hercules CA, USA) at 180 V for 45 minutes (EPS-300 X Power Supply, Fisher Scientific, Hampton NH, USA) and staining with SimplyBlue Safe Stain (Invitrogen, Carlsbad CA, USA)). If the purity was not sufficient, additional ITC cycles were performed. Once the desired

purity (>95%) was reached, the sample was dialysed against nanopure water over two days (in SnakeSkin dialysis tubing, 3'500 MWCO (Thermo Fisher Scientific, Waltham MA, USA)). Subsequently, the dialysed samples were lyophilised on a Labconco FreeZone 2.5 plus lyophiliser (Labconco, Kansas City MO, USA). Like this, protein yields of between 20-100 mg were reached per L of bacterial culture.

PAzF Proteins

The expression and purification protocol for pAzF proteins was basically identical to the one described above apart from a few exceptions: For one, the expression was performed in the genetically recoded *E. coli* strain C321.ΔA rather than BL21 (DE3). Secondly, the growth media contained three additional ingredients, namely arabinose (0.2% w/v), chloramphenicol (25 μg/mL) and *para*-azidophenylalanine (Chem-Impex International (Wood Dale IL, USA), 1 mM). Thirdly, the temperature was kept at 34°C prior to IPTG induction and was then lowered to 25°C. And lastly, the samples needed to be protected from light throughout the expression and purification steps as well as all subsequent characterisation steps.

A.iv Protein Labelling

To attach fluorescent dyes to the N-terminus of the protein of interest, some lyophilised protein sample was dissolved in aq. sodium bicarbonate solution (0.1 M, pH 8.3) to which an NHS-funcionalised AlexaFluor flourophore (Invitrogen, Carlsbad CA, USA) was added in large excess (>5 equivalents). After incubation at room temperature for 1 hour, the sample was dialysed and lyophilised analogously as described in the above section.

Subsequently, the labelled proteins were dissolved in PBS and mixed with the unlabelled proteins such that the protein-vs-dye ratio was at 10:1. Protein and dye concentrations were determined using the UV/Vis setup on the NanoDrop 1000 instrument (Thermo Fisher Scientific, Waltham MA, USA).

A.v *Para*-Azidophenylalanine Crosslinking

The crosslinking of pAzF proteins was performed using a Omnicure series 1000 UV source (equipt with a 320-500 nm filter, Nordson, Westlake OH, USA). During the crosslinking step, the typical 0.25-1.0 mL of protein solution were kept in a 35 mm Primaria™ cell culture dish (Thermo Fisher Scientific, Waltham MA, USA) to maximise the exposed surface area. Each sample would be exposed to the UV source for three intervals of 20 seconds with mixing steps in between each exposure.

A.vi Dynamic Light Scattering

The DLS data in this study was acquired using a DynaPro plate reader (Wyatt Technology, Goleta CA, USA). The analysed samples were loaded in the individual wells of a 96-well plate (50 μL analyte volume) and covered with mineral oil (25 μL) to prevent solvent evaporation during the measurements. The DLS results mentioned in this study represent the average of at least 10 (max. 20) measurements acquired over at least 10 (max. 30) seconds each.

A.vii Cryo-Transmission Electron Microscopy

Cryo-TEM images were taken on a FEI Tecnai G2 Twin TEM (FEI, Hillsboro OR, USA) at a voltage of 80 kV. Prior to imaging the samples were prepared as follows: Lacey holey carbon grids (Ted Pella, Redding CA, USA) were glow discharged in a PELCO EasiGlow apparatus (Ted Pella, Redding CA, USA) and loaded into the Vitrobot Mark IV vitrification instrument (FEI, Hillsboro OR, USA). Subsequently, 3 µL of sample were carefully deposited onto the grid, blotted for 3 seconds at a force of -3 and with a drain time of 1 second and then vitrified in liquid ethane. The grids were then transferred onto a Gatan 626 cryoholder (Gatan, Pleasanton CA, USA) which was inserted into the TEM instrument.

A.viii Surface Plasmon Resonance

The SPR measurements for both integrin- as well as DR5 targeting nanoparticles were performed on a Biacore T200 instrument (GE Healthcare, Chicago IL, USA) at 25°C. The flow channels of the CM5 sensor chip (GE Healthcare, Chicago IL, USA) were normalized using 70% glycerol. Recombinant human DR5 receptors (Sino Biological Inc., Beijing, CHN) and $\alpha_v\beta_3$ integrins (Novus Biologicals, Littleton CO, USA) were immobilized in separate flow channels using NHS/EDC coupling. Upon immobilization, the two receptors reached a surface density of around 1'200 ($\alpha_v\beta_3$ integrin) and 2'100 (DR5) response units (RU) respectively. For the control channel, we used analogous methods to immobilize the crosslinked, unfunctionalized UAA5-40 construct to reach a surface density of around 4'500 RU. The SPR measurements were performed using crosslinked/native nanoparticle samples at various concentrations in PBS. All samples were injected into the flow cells at a flow rate of 5 µL/min for 3 minutes and then allowed to dissociate for 10 minutes. The surface was subsequently regenerated using 2 mM aq. NaOH at a flow rate of 5 µL/min for 40 seconds. After subtraction of the signal from the reference channel, the final SPR sensograms were analyzed using the 1:1 Langmuir binding model on the BIAevaluation sofware (GE Healthcare, Chicago IL, USA).

A.ix Cell Experiments

Cell Culturing

All cell lines used in the course of this master project were purchased from the American Type Culture Collection (ATCC, Manassas VA, USA) and cultured following the respective manuals on the ATCC website.

Cell Uptake Experiments – Suspension Cell Lines

For the cell uptake experiments on the two K562 cell lines, cell culture was harvested from the culturing vessel and centrifuged at 500 g for 5 minutes after which the supernatant was carefully removed. The cell pellet was gently resuspended in fluorescently tagged protein sample solution to reach a cell density of 1 million cells/mL. After incubation of the mixture at 37°C and 200 rpm, it was spun down at 500 g for 5 minutes and the supernatant was carefully removed. After 2 washing steps (resuspension in 1 mL of Hanks' buffered salt solution (HBSS), centrifugation at 800 g for 5 minutes and removal of the supernatant), the cell pellet was finally resuspended in PBS + 1% BSA at a cell density of 1 million cells/mL.

To analyse the uptake levels of the proteins by the cells the samples were loaded onto a 384-well plate and imaged on a Dragonfly 500 spinning disk confocal microscope (Andor Technology, Belfast, UK). Moreover, cell uptake levels were also determined on an Accuri C5 flow cytometer (Becton Dickinson, Franklin Lakes NJ, USA). The cell fluorescence intensity was quantified after gating to remove false positive measurements.

Cell Uptake Experiments – Adherent Cell Lines

For the adherent cell lines, the cell uptake experiments required seeding wells of a 4-well plate (ibidi GmBH, Planegg, GER) with 10'000 cells each one day prior to the actual experiment. After 24 hours of incubation following the ATCC recommendation, the supernatant was carefully removed and replaced with 50 µL of protein sample. After 2 hours of incubation at 37°C, the protein solution was removed and the cells washed twice with 100 µL of HBSS before the addition of PBS + 1% BSA. Cell uptake levels were then determined using the same confocal microscope as for the suspension cell lines.

Cell Viability Assays

The cell viability assays were started by seeding the wells of a 96-well plate (Thermo Fisher Scientific, Waltham MA, USA) with 10'000 cells each in a volume of 90 µL. After 24 hours of incubation following the ATCC guidelines, 10 µL of protein sample at different concentrations were added in duplicates. Again, 24 hours later 15 µL of CellTiter-Glo® (Promega Corporation, Madison WI, USA) were added to each well and mixed by gently tapping the 96-well plate. After 40 minutes of incubation at room temperature under exclusion of light, cell viability was determined by measuring the luminescence of each well on a Perkin Elmer Wallac 1420 Victor^2 microplate reader (Perkin Elmer, Waltham MA, USA).

A.x Transition Temperature Determination

To determine the transition temperature of ELP/RLP constructs as well as to investigate the reversibility of the phase separation, UV/Vis spectroscopy was employed: Optical transmission at 350 nm was recorded for increasing/decreasing temperatures on a Cary series UV/Vis spectrophotometer (Agilent Technologies, Santa Clara CA, USA). The samples were heated at a rate of 1°C/min.

A.xi Water-in-Oil Microcompartments

Production

Water-in-oil microcompartments were produced in a microfluidic droplet-generating glass chip (Dolomite Microfluidics, Royston, UK) using two different liquid phases: An aqueous, ELP/RLP-containing phase in PBS and an organic phase comprised of TEGOSOFT DEC, ABIL EM 90 and mineral oil (75%, 5% and 20% v/v, Evonik Industries, Essen, GER). The two phases were injected into the microfluidic device using syringe pumps (Chemyx Inc., Stafford TX, USA) at constant flow rates of 250 µL/h (organic phase) and 75 µL/h (aqueous phase) respectively. The microcompartment production and morphology was monitored using an inverted microscope (5x, Leica, Wetzlar, GER) equipped with a digital microscopy camera (Lumenera Infinity 3-1 CCD, Teledyne Lumenera, Ottawa, CAN).

Characterization

The created water-in-oil emulsion was then transferred onto a glass microscope slide (VWR International, Radnor PA, USA) and placed on a Linkam LTS120 heating and cooling stage equipped with a Linkam PE95 temperature control unit (both Linkam Scientific Instruments, Tadworth, UK). The phase transition during heating/cooling was simultaneously recorded with an upright Zeiss Axio Imager A2 fluorescence microscope (Carl Zeiss AG, Oberkochen, GER).

B – Genetic Sequences

Note that the AcuI and BseRI cut sites are located within the first and last glycine codon. Thus, the C-terminal tyrosine of the N-terminal fragment is removed upon pre-RDL ligations.

Project I

Protein	Amino Acid Sequence	DNA Sequence
$ELP_{A/G,\ 80}$	$(GAGVPGVGVP)_{40}$-GY	$(GGCGCAGGTGTTCCGGGTGGCGG-TGTGCCGGGCGCAGGTGTCCCGGG-TGGCGGTGTGCCGGGCGCAGGTGT-CCCGGGTGGCGGTGTTCCGGGCGC-AGGTGTCCCGGGTGGCGGTGTGCC-GGGCGCAGGTGTTCCGGGTGGCGG-GGTGCCG)_8$-GGCTAC
RLP_{40}	$(GQYPSDGR)_{40}$-GY	$(GGGCAGTACCCATCTGACGGTCG-CGGTCAGTATCCGAGCGACGGCCG-TGGTCAGTATCCGAGTGACGGCCG-TGGTCAATACCCTTCGGATGGTCGT)_{10}$-GGCTAC
RLP_{80}	$(GQYPSDGR)_{80}$-GY	$(GGGCAGTACCCATCTGACGGTCG-CGGTCAGTATCCGAGCGACGGCCG-TGGTCAGTATCCGAGTGACGGCCG-TGGTCAATACCCTTCGGATGGTCGT)_{20}$-GGCTAC
*p*AzF-glycine-RLP_8	G-pAzF-$(GQYPSDGR)_8$-GY	GGCTAG-(GGGCAGTACCCATCTGA-CGGTCGCGGTCAGTATCCGAGCGA-CGGCCGTGGTCAGTATCCGAGTGA-CGGCCGTGGTCAATACCCTTCGGA-TGGTCGT)$_2$-GGCTAC
*p*AzF-glycine-RLP_{20}	G-pAzF-$(GQYPSDGR)_{20}$-GY	GGCTAG-(GGGCAGTACCCATCTGA-CGGTCGCGGTCAGTATCCGAGCGA-CGGCCGTGGTCAGTATCCGAGTGA-CGGCCGTGGTCAATACCCTTCGGA-TGGTCGT)$_5$-GGCTAC
K_8D_4	GG-K_8-GGG-D_4-GGY	GGCGGCAAGAAGAAGAAGAAGAA-GAAGAAGGGCGGCGGCGACGACG-ACGACGGCGGC
AHNP	GFCGDGFYACAMDVGY	GGCTTTTGTGGAGATGGATTTTAC-GCTTGTTATATGGATGTCGGCTAC

GRGDSPAS	GRGDSPASGY	GGCCGCGGTGACTCACCGGCGTC-AGGCTAC
Fn3	GVSDVPRDLEVVAATPT-SLLISWDAPAVTVRYYR-TYGETGGNSPVQEFTVP-GSKSTATIS-GLKPGVDYTITVYAVT-GRGDSPASS-KPISINYRTGY	GGCGTGTCCGATGTACCCCGTGAC-CTGGAGGTAGTAGCCGCCACGCCC-ACATCGTTATTAATCTCATGGGACG-CTCCTGCAGTTACTGTAAGATATTA-TCGGATCACTTACGGAGAAACGGG-TGGAAATAGCCCGGTACAGGAGTT-CACGGTGCCGGGCTCCAAGAGTAC-TGCAACAATCTCCGGTCTGAAACCG-GGCGTAGACTACACCATTACTGTCT-ACGCAGTAACCGGACGCGGTGACT-CACCGGCGTCATCCAAACCTATAA-GCATTAACTATCGGACCGGCTAC
Polybia-MPI	GIDWKKLLDAAKQILGY	GGCATTGATTGGAAGAAGTTGTTG-GACGCCGCCAAGCAGATTTTGGGC-TAC
Tn3	GAIEVKDVTDTTALITW-AKPWVDPPPLWGIELTY-GIKDVPGDRTTIDLQQK-HTAYSIGNLKPDTEYEV-SLISFDPYGMRSKPAKE-TFTTGGGGSGGGGSGG-GGSGY	GGCGCGATTGAAGTTAAGGATGTG-ACGGACACCACCGCACTGATTACA-TGGGCAAAACCCTGGGTAGACCCG-CCGCCGCTGTGGGGAATCGAACTG-ACCTATGGTATTAAGGATGTTCCAG-GCGATCGCACGACCATCGATCTGCA-ACAGAAACACACCGCGTATAGTATC-GGGAACCTTAAACCAGATACAGAAT-ATGAAGTTTCTCTCATCTCCTTTGAT-CCGTATGGAATGCGTTCTAAACCTG-CCAAAGAAACCTTCACGACGGGCG-GCGGTGGCTCTGGCGGCGGTGGTA-GCGGTGGAGGCGGAAGCGGCTAC
TRAIL	GVRERGPQRVAAHITGT-RGRSNTLSSPNSKNEKA-LGRKINSWESSRSGHSF-LSNLHLRNGELVIHEKG-FYYIYSQTYFRFQEEIKE-NTKNDKQMVQYIYKYT-SYPDPILLMKSARNSCW-SKDAEYGLYSIYQGGIF-ELKENDRIFVSVTNEHL-IDMDHEASFFGAFLVGG-SGGGGSLPETGGGY	GGCGTTCGTGAACGTGGTCCGCAG-CGTGTTGCAGCACATATTACCGGC-ACCCGTGGTCGGAGCAATACCCTG-AGCAGCCCGAATAGCAAAAATGAA-AAAGCACTGGGTCGCAAAATTAAC-AGCTGGGAAAGCAGCCGTAGCGGT-CATAGCTTTCTGAGCAATCTGCATC-TGCGTAATGGTGAACTGGTGATTCA-TGAAAAAGGCTTCTACTATATCTAC-AGCCAGACCTATTTTCGCTTCCAAG-AAGAGATTAAAGAAAACACCAAAA-ACGATAAACAAATGGTGCAGTACAT-

		CTATAAATACACCAGCTATCCGGAT-CCGATTCTGCTGATGAAAAGCGCAC-GTAATAGCTGTTGGAGCAAAGATGC-AGAATATGGCCTGTATAGCATTTATC-AGGGTGGCATCTTTGAACTGAAAGA-AAACGATCGTATTTTCGTGAGCGTG-ACCAATGAACATCTGATCGATATGG-ATCATGAAGCCAGCTTTTTTGGTGC-ATTTCTGGTGGGTGGATCCGGTGGC-GGTGGCTCTCTGCCGGAAACCGGTG-GCGGCTAC
TRAIL peptide	GWDCLDNKIGRRQCVR-LGY	GGCTGGGATTGTCTTGACAATAAA-ATCGGTCGTCGCCAATGTGTGCGT-TTGGGCTAC

Project II

Note the color coding within the DNA sequences. Green corresponds to the ELP sequence iself, red denotes binding sites for T7 primers and blue indicates binding sites for fwd2/rev3 primers.

Construct	DNA Sequence
$(VPGVG)_{10}$ oligonucleotide	TCCCGCGAAATTAATACGACTCACTATAGGGAAGAAGGAGGA-GTACATATGGGCGTTCCAGGCGTGGGGGTACCTGGGGTCGGA-GTGCCGGGAGTCGGCGTGCCAGGTGTTGGGGTGCCCGGAGTT-GGTGTGCCTGGTGTGGGGGTTCCTGGTGTAGGCGTCCCGGGA-GTAGGAGTTCCAGGGGTCGGCGTACCCGGTGTTGGCTGATAA-TAATGATCTTCAGGTCCGAATTCGCCGCTGAGCAATAACTAGC-ATAACCCCTTGGG
$(VPGVG)_{10}$ vector-bound	…TAGGGGAATTGTGAGCGGATAACAATTCCCCTCTAGAAATA-ATTTTGTTTAACTTTAAGAAGGAGGAGTACATATGGGCGTTCC-AGGCGTGGGGGTACCTGGGGTCGGAGTGCCGGGAGTCGGCGT-GCCAGGTGTTGGGGTGCCCGGAGTTGGTGTGCCTGGTGTGGGG-GTTCCTGGTGTAGGCGTCCCGGGAGTAGGAGTTCCAGGGGTCG-GCGTACCCGGTGTTGCCTACTGATAATGATCTTCAGGATCCGA-ATTCGAGCTCCGTCGACAAGCTTGCGGCCGCACTC…
T7 fwd primer	TAATACGACTCACTATAGGG
T7 rev primer	GCTAGTTATTGCTCAGCGG
Fwd1 primer	AACTTTAAGAAGGAGGAGTAC
Fwd2 primer	GCGGATAACAATTCCCCTCTAG
Rev1 primer	CGAATTCGGATCCTGAAGATC

Rev2 primer	AGCTCGAATTCGGATCC
Rev3 primer	CTTGTCGACGGAAGCTCG

Project III

Protein	Amino Acid Sequence	Genetic Sequence
ELP_{hys}-5X	G-$(VPAVG)_{5X}$-Y	GGC-(GTACCCGCCGTAGGTGTGCCTGCG-GTAGGCGTTCCTGCTGTTGGAGTACCTG-CAGTTGGTGTCCCTGCCGTCGGC)$_X$-TAC
ELP_V-5X	G-$(VPGVG)_{5X}$-Y	GGC-(GTTCCCGGCGTCGGGGTCCCTGG-TGTGGGAGTTCCGGGTGTCGGCGTGCCC-GGAGTCGGCGTCCCGGGGGTAGGC)$_X$-TAC
ELP_{4VE}-5X	G-$[(VPGVG)_2$-(VPGEG)-$(VPGVG)_2]_X$-Y	GGC-(GTACCAGGCGTTGGTGTCCCCGGT-GTCGGTGTACCTGGAGAGGGAGTACCA-GGGGTAGGAGTCCCTGGAGTCGGC)$_X$-TAC
ELP_{3V2E}-5X	G-[(VPGVG)-(VPGEG)-(VPGVG)-(VPGEG)-(VPGVG)]$_X$-Y	GGC-(GTACCTGGCGTCGGAGTACCCGG-AGAAGGGGTGCCTGGAGTAGGTGTACCT-GGTGAGGGGGTACCAGGAGTAGGC)$_X$-TAC
ELP_{V3IE}-5X	G-$[(VPGVG)$-$(VPGIG)_2$-(VPGEG)-(VPGIG)]$_X$-Y	GGC-(GTTCCAGGAGTTGGAGTACCAGG-AATAGGAGTCCCCGGAATAGGCGTTCC-TGGGGAAGGAGTACCGGGCATCGGC)$_X$-TAC
ELP_{V2HGA}-5X	G-[(VPGVG)-(VPGHG)-(VPGGG)-(VPGHG)-(VPGAG)]$_X$-Y	GGC-(GTACCTGGTGTTGGAGTACCTGG-CCACGGCGTACCAGGGGGAGGTGTACC-TGGACATGGGGTCCCTGGGGCTGGC)$_X$-TAC

C – SDS-PAGE Gels

Project I

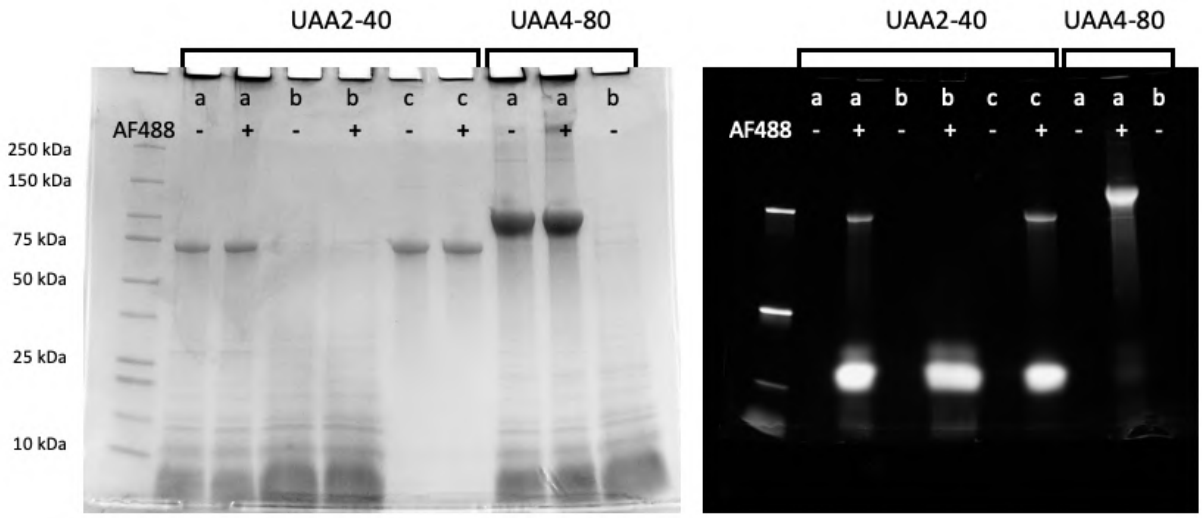

Figure S1: SDS-PAGE gel images after expression and purification of the three unfunctionalized *p*AzF-containing ELP/RLP diblock constructs. a) bacterial lysate b) hot spin supernatant c) cold spin supernatant. Note that the sample in every second lane was co-incubated with DBCO-AF488 prior to running the gel. The gel on the left was stained with SimplyBlue Safe Stain whereas the gel on the right shows the fluorescence at 488 nm of the individual bands.

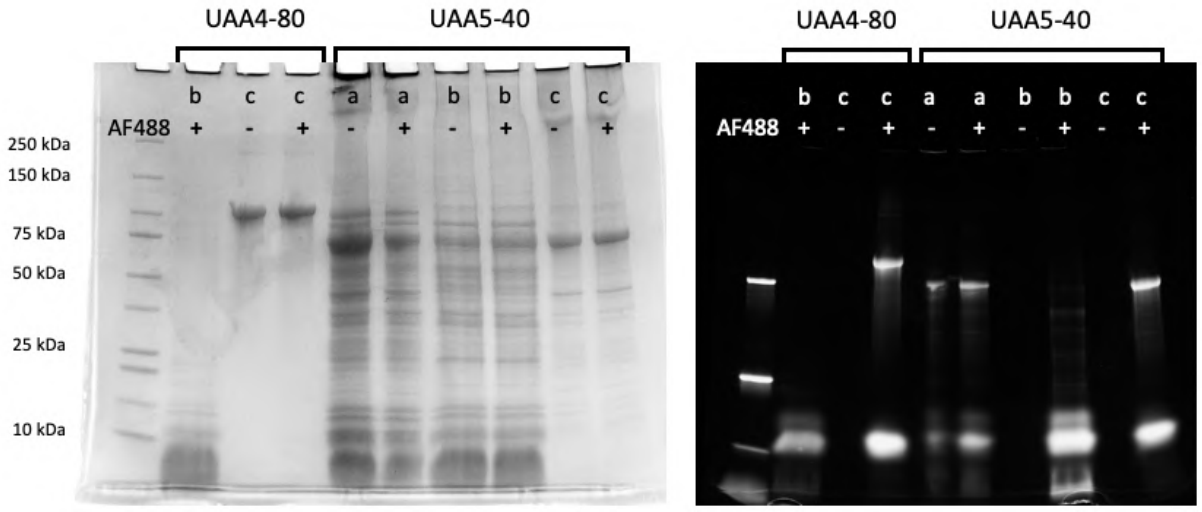

Figure S2: Continuation of figure S1

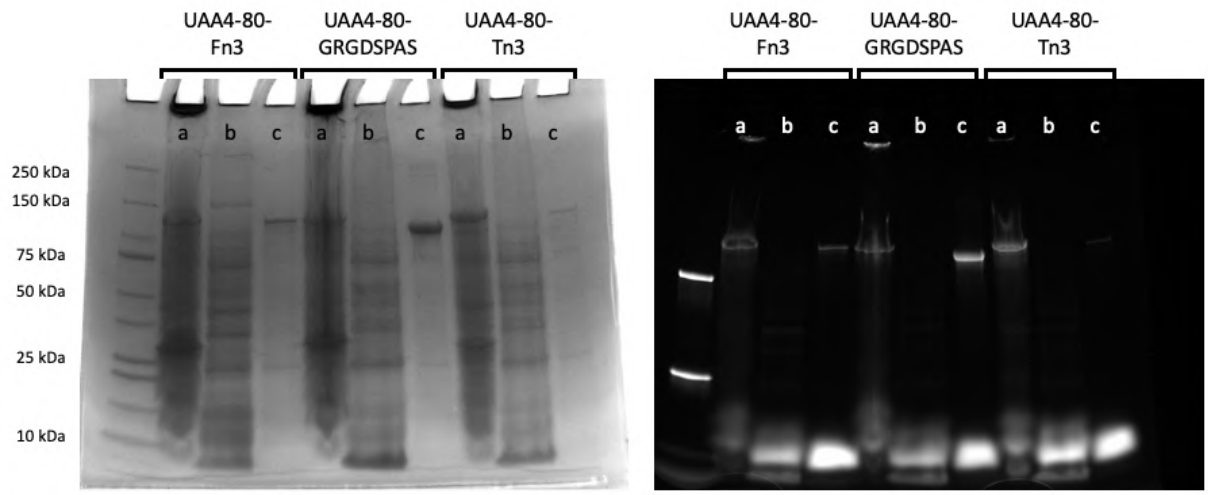

Figure S3: SDS-PAGE gel images after expression and purification of the K_8D_4-free constructs UAA4-80-Fn3, -GRGDSPAS and -Tn3. a) bacterial lysate b) hot spin supernatant c) cold spin supernatant. Note that all samples were co-incubated with DBCO-AF488 prior to running the gel. The gel on the left was stained with SimplyBlue Safe Stain whereas the gel on the right shows the fluorescence at 488 nm of the individual bands.

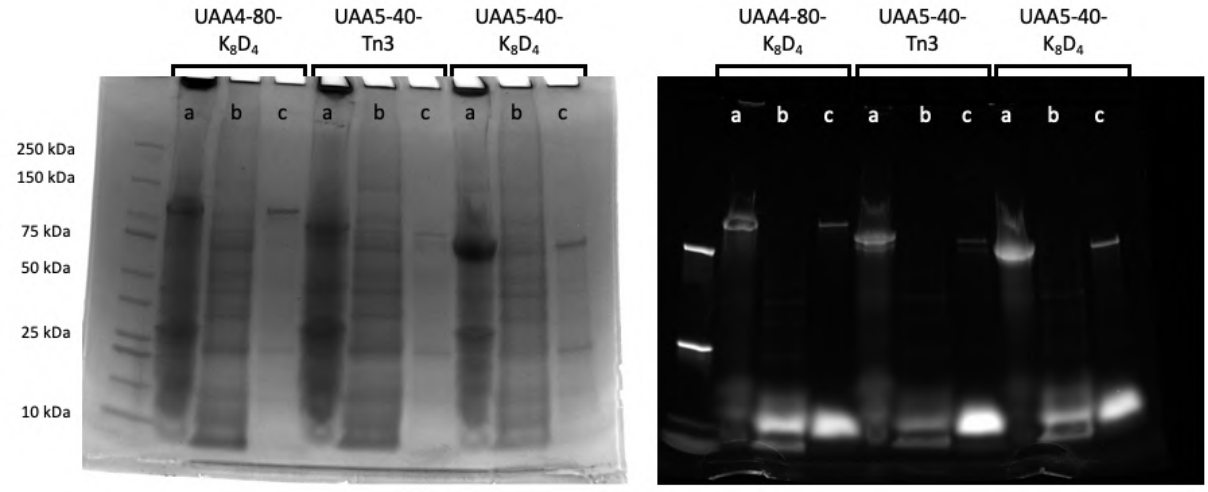

Figure S4: SDS-PAGE gel images after expression and purification of the constructs UAA4-80-K_8D_4, UAA5-40-Tn3 and UAA5-40-K_8D_4. a) bacterial lysate b) hot spin supernatant c) cold spin supernatant. Note that all samples were co-incubated with DBCO-AF488 prior to running the gel. The gel on the left was stained with SimplyBlue Safe Stain whereas the gel on the right shows the fluorescence at 488 nm of the individual bands.

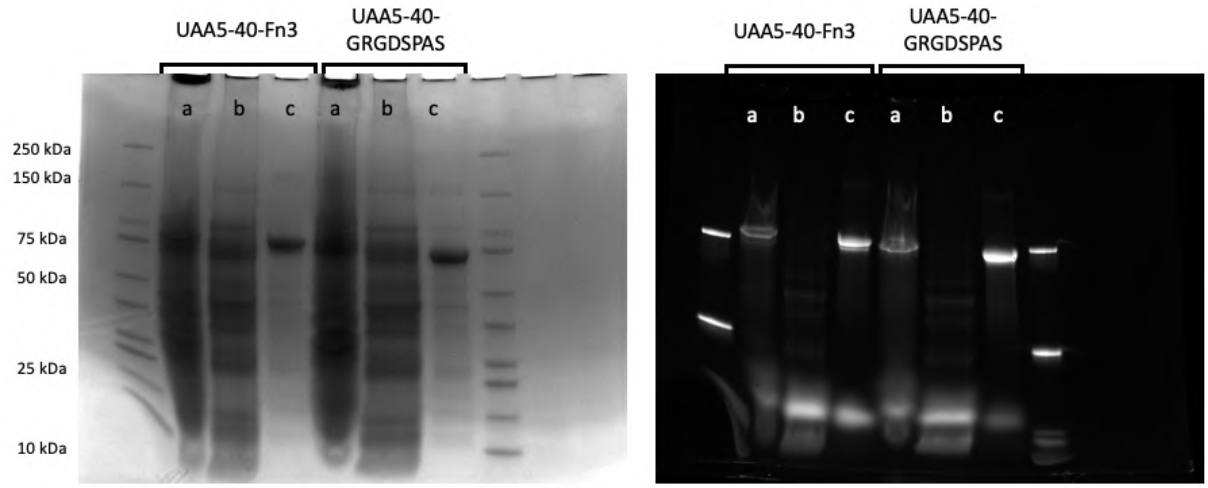

Figure S5: SDS-PAGE gel images after expression and purification of the constructs UAA5-40-Fn3 and UAA5-40-GRGDSPAS. a) bacterial lysate b) hot spin supernatant c) cold spin supernatant. Note that all samples were co-incubated with DBCO-AF488 prior to running the gel. The gel on the left was stained with SimplyBlue Safe Stain whereas the gel on the right shows the fluorescence at 488 nm of the individual bands.

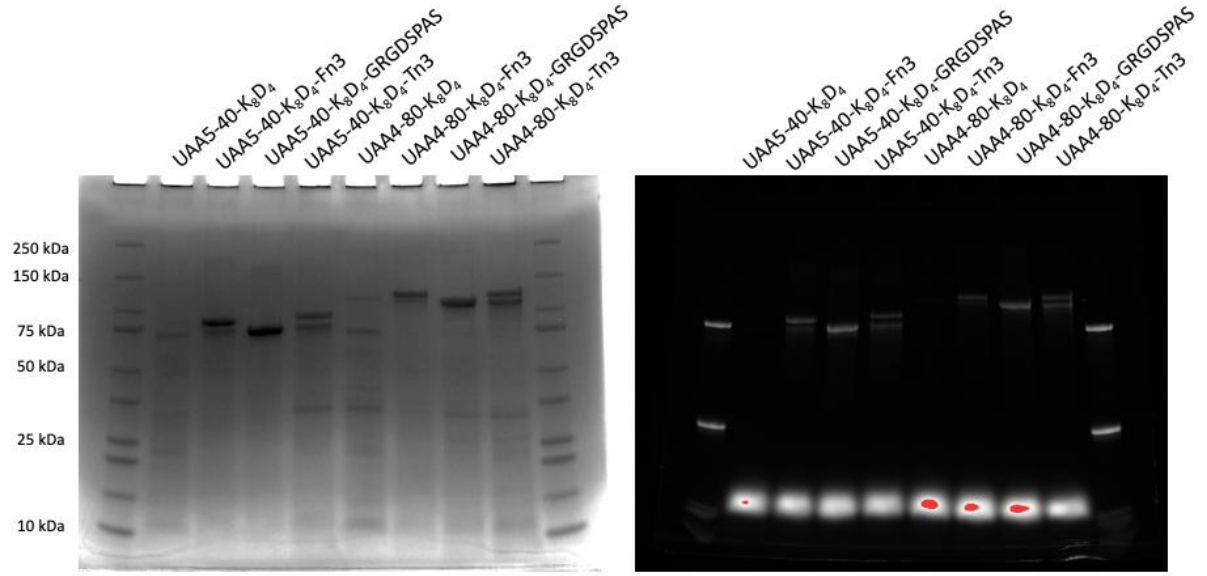

Figure S6: SDS-PAGE gel images of the eight purified K_8D_4-containing constructs used for the final multivalency experiments. Note that all samples were co-incubated with DBCO-AF488 prior to running the gel. The gel on the left was stained with SimplyBlue Safe Stain whereas the gel on the right shows the fluorescence at 488 nm of the individual bands.

Project III

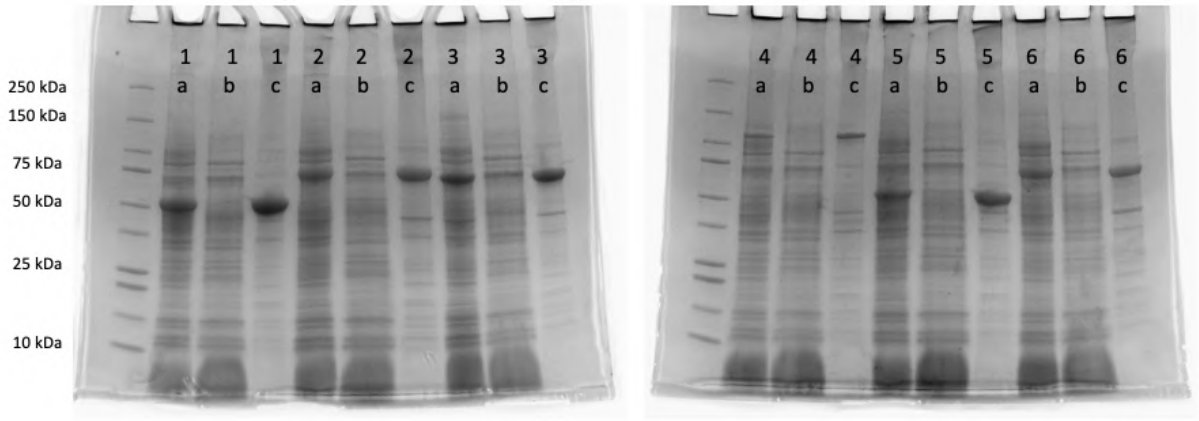

#	Construct	#	Construct	#	Construct
1	$ELP_{4VE,40}$-RLP_{40}	3	$ELP_{3V2E,40}$-RLP_{40}	5	$ELP_{V3IE,40}$-RLP_{40}
2	$ELP_{4VE,80}$-RLP_{40}	4	$ELP_{3V2E,80}$-RLP_{40}	6	$ELP_{V3IE,80}$-RLP_{40}

Figure S7: SDS-PAGE gel images after expression and purification of the different constructs of the third project of this master thesis. a) bacterial lysate b) hot spin supernatant c) cold spin supernatant. Both gels were stained with SimplyBlue Safe Stain.

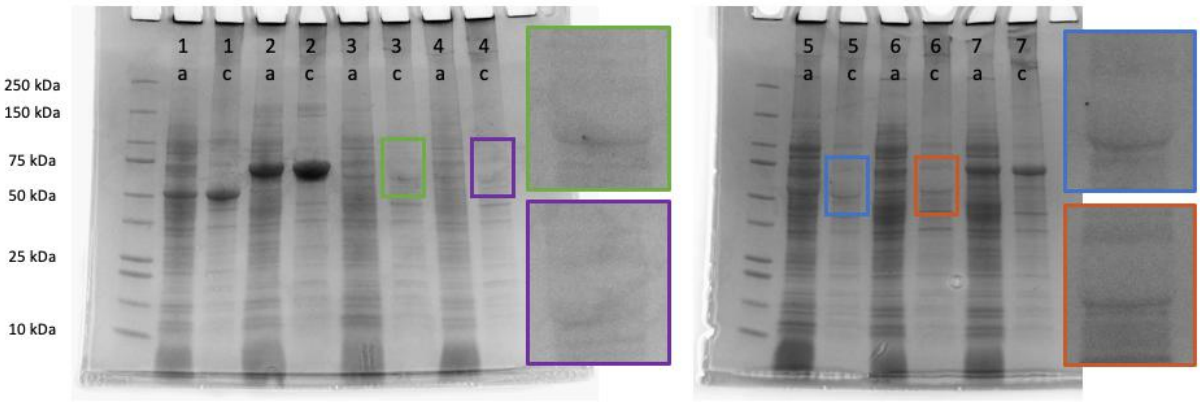

#	Construct	#	Construct	#	Construct
1	$ELP_{V2HGA,40}$-RLP_{40}	4	$ELP_{4VE,40}$-$ELP_{hys,40}$-$ELP_{4VE,40}$	7	$ELP_{4VE,40}$-RLP_{40}-$ELP_{4VE,40}$
2	$ELP_{V2HGA,80}$-RLP_{40}	5	$ELP_{4VE,40}$-$ELP_{V,80}$		
3	$ELP_{4VE,40}$-$ELP_{hys,80}$	6	$ELP_{4VE,40}$-$ELP_{V,40}$-$ELP_{4VE,40}$		

Figure S8: Continuation of figure S7. Note that constructs number 3, 4, 5 and 6 do not contain any aromatic residues and thus did not stain with SimplyBlue Safe Stain. By taking a closer look at the corresponding lanes one can however see a slight broadening of the lane at the targeted mass similar to an “overloaded” lane (compare to lane 2c for instance).

University of Basel

Faculty of Science

Declaration on Scientific Integrity
(including a Declaration on Plagiarism and Fraud)

Master's Thesis ☑

Title of Thesis *(Please print in capital letters)*:

IMPROVING CLONING PROCEDURES AND PARTICLE ARCHITECTURES OF ELASTIN-LIKE POLYPEPTIDE-BASED DRUG DELIVERY VEHICLES

First Name, Surname: PATRICK WEBER
(Please print in capital letters)

Matriculation No.: 14-055-370

With my signature I declare that this submission is my own work and that I have fully acknowledged the assistance received in completing this work and that it contains no material that has not been formally acknowledged.

I have mentioned all source materials used and have cited these in accordance with recognised scientific rules.

In addition to this declaration, I am submitting a separate agreement regarding the publication of or public access to this work.

☒ Yes ☐ No

Place, Date: MEGGEN, NOVEMBER 13TH 2019

Signature: P Weber

Please enclose a completed and signed copy of this declaration in your Bachelor's or Master's thesis .